Springer Theses
Recognizing Outstanding Ph.D. Research

Jan Becker

Plasmons as Sensors

Springer

Springer Theses

Recognizing Outstanding Ph.D. Research

For further volumes:
http://www.springer.com/series/8790

Aims and Scope

The series "Springer Theses" brings together a selection of the very best Ph.D. theses from around the world and across the physical sciences. Nominated and endorsed by two recognized specialists, each published volume has been selected for its scientific excellence and the high impact of its contents for the pertinent field of research. For greater accessibility to non-specialists, the published versions include an extended introduction, as well as a foreword by the student's supervisor explaining the special relevance of the work for the field. As a whole, the series will provide a valuable resource both for newcomers to the research fields described, and for other scientists seeking detailed background information on special questions. Finally, it provides an accredited documentation of the valuable contributions made by today's younger generation of scientists.

Theses are accepted into the series by invited nomination only and must fulfill all of the following criteria

- They must be written in good English.
- The topic should fall within the confines of Chemistry, Physics, Earth Sciences, Engineering and related interdisciplinary fields such as Materials, Nanoscience, Chemical Engineering, Complex Systems and Biophysics.
- The work reported in the thesis must represent a significant scientific advance.
- If the thesis includes previously published material, permission to reproduce this must be gained from the respective copyright holder.
- They must have been examined and passed during the 12 months prior to nomination.
- Each thesis should include a foreword by the supervisor outlining the significance of its content.
- The theses should have a clearly defined structure including an introduction accessible to scientists not expert in that particular field.

Jan Becker

Plasmons as Sensors

Doctoral Thesis accepted by
the University of Mainz, Germany

Springer

Author
Dr. Jan Becker
University of Mainz
Germany

Supervisor
Prof. Dr. Carsten Sönnichsen
University of Mainz
Germany

ISSN 2190-5053 ISSN 2190-5061 (electronic)
ISBN 978-3-642-31240-3 ISBN 978-3-642-31241-0 (eBook)
DOI 10.1007/978-3-642-31241-0
Springer Heidelberg New York Dordrecht London

Library of Congress Control Number: 2012940951

Scientific Publications

Parts of this thesis have been published in the following scientific journals:

"*Gold Nanoparticle Growth Monitored in situ Using a Novel Fast Optical Single-Particle Spectroscopy Method*"
J. Becker, O. Schubert, and C. Sönnichsen
Nano Letters, Year: 2007, Vol. 7, Pages: 1664–1669

"*Plasmonic Focusing Reduces Ensemble Linewidth of Silver-Coated Gold Nanorods*"
J. Becker*, I. Zins*, A. Jakab, Y. Khalavka, O. Schubert, and C. Sönnichsen
Nano Letters, Year: 2008, Vol. 8, Pages: 1719–1723

"*Protein-Membrane Interaction Probed by Single Plasmonic Nanoparticles*"
C. Baciu*, J. Becker*, A. Janshoff, and C. Sönnichsen
Nano Letters, Year: 2008, Vol. 8, Pages: 1724–1728

"*Mapping the Polarization Pattern of Plasmon Modes Reveals Nanoparticle Symmetry*"
O. Schubert, J. Becker, L. Carbone, Y. Khalavka, T. Provalska, I. Zins, and C. Sönnichsen
Nano Letters, Year: 2008, Vol. 8, Pages: 2345–2350

"*Synthesis of Rod-Shaped Gold Nanorattles with Improved Plasmon Sensitivity and Catalytic Activity*"
Y. Khalavka, J. Becker, and C. Sönnichsen
Journal of the American Chemical Society, Year: 2009, Vol. 131, Pages: 1871–1875

"*The Optimal Aspect Ratio of Gold Nanorods for Plasmonic Bio-Sensing*"
J. Becker, A. Trügler, A. Jakab, U. Hohenester, and C. Sönnichsen
Plasmonics, Year: 2010, Vol. 5, Pages: 161–167

*Authors contributed equally, in alphabetic order

Supervisor's Foreword

The sensing of molecular events with plasmonic nanoparticles offers a new window into the molecular world. Mostly hidden to us, dissolved molecules show complex conformational dynamics, molecular interactions and spatial diffusion. Many of those features average out in measurements integrating over time or large ensembles of molecules. Knowing the detailed dynamics is essential to understand biological functions and nanoparticle growth at the molecular level. However, few experimental techniques provide access to molecular events in solution and commonly require fluorescent dye labels attached to the molecule of interest. Analyte modification could potentially influence biological processes triggering current searches for unlabeled protein detection methods. Currently, optical microcavities (whispering gallery modes WGM), surface-enhanced Raman scattering (SERS), and electric detection via carbon nanotube or boron-doped silicon nanowire field-effect transistors are discussed for detection of unlabeled proteins. Each of those methods suffers from one or more disadvantages, e.g., complex sensor fabrication, or low signal-to-noise level, which has prevented their practical use in most cases.

Some years ago, we (and others) came up with the concept of using single gold nanoparticles to detect changes in their local environment. Plasmonic nanoparticles react to refractive index changes in their direct environment by a shift of the plasmon resonance. This can be monitored on single nanoparticles by optical dark-field spectroscopy. So far, these experiments were restricted to one single nanoparticle that was aligned with the input of a spectrometer. If dynamic processes, e.g., nanoparticle growth or molecular binding events, were investigated, this meant effectively to repeat the entire experiment over and over again to collect the necessary statistics for a confident interpretation of the observed changes. In principle, a spectrometer coupled to a CCD camera could analyze spectra of several nanoparticles at once if those nanoparticles were somehow aligned with the entrance slit. Many researchers came up with ideas to position the nanoparticles in such orderly arrays. So far, any such positioning strategy has proved to be too complex for routine use.

At the start of Jan Becker's work in my group, we came up with a new twist to this problem: if the nanoparticles could not be positioned effectively, why not use a 'flexible' entrance slit that positions itself above the image of the nanoparticles? After some unsuccessful trials with disassembled projectors, Jan found a working solution using a liquid crystal matrix. Each pixel of this matrix could be addressed separately and acts as an electronically tunable entrance slit. In each line, the 'slit' could 'move' horizontally until a nanoparticle position was matched.

This new technique sped up the plasmon sensing experiment by more than an order of magnitude. To fully comprehend the enormous effect this had on the way plasmon experiments were performed, one has to remember that previously each spectrum had to be collected on a new sample. For a small statistics of, for example, 20 particles, one would have had to create more than 20 identical samples, mount them, exchange liquids in a defined way to bind certain molecules on the surface, etc. Such experiment could, in reality, take months to complete and tire out even a dedicated researcher. Now, this experiment is possible in a single day on a single substrate. This is not only more reliable, it is another world in terms of user friendliness. Simply comparing times gives not enough credit to this change.

With this new system that we termed FastSPS in his hands, Jan Becker has used his talent for attracting collaborations to use it in various directions. The most important ones for advancing the plasmon sensor technology are outlined in this book: the development of a flexible method for the biofunctionalization of plasmon sensors and the optimization of the plasmonic nanoparticles used. For the latter, he performed many simulations to guide the experimental work and collaborated with several chemists that used strategies such as silver coating or rattle formation to enhance the nanoparticle geometry and composition to yield more sensitive nanoparticles.

The new FastSPS method that Jan Becker describes in detail in this book has paved the road toward more advanced plasmon sensing experiments. The book contains plenty of examples of how to perform plasmonic sensing experiments to answer several distinct types of questions, e.g., nanoparticle growth or molecular binding efficiency. He provides a solid theoretical introduction into plasmons and background information on plasmonic sensing. For many years to come, this work will set the standard against which plasmon sensing experiments will be measured.

Prof. Dr. Carsten Sönnichsen

Acknowledgments

At this point I would like to thank the following persons who have been very helpful in contributing to the success of this thesis:

First of all my thanks go to my supervisor Prof. Dr. Carsten Sönnichsen for giving me the opportunity to do my PhD in his group. The fact that his door was always open gave me the possibility for having innumerable helpful discussions and advices.

I would also like to thank Dr. Maximilian Kreiter, who had kindly agreed to co-referee this thesis.

Inga Zins, who provided the basis of several successful common projects by her tireless impulse to arrange additional experiments. With her warm character, she additionally improved our collaboration enormously.

Arpad Jakab for several discussions in fundamental solid-state physics. Our neighboring setups allowed us to have a lot of fun during plenty of hours that we spent in front of our microscopes.

Yuriy Khalavka, who helped me several times to align the transmission electron microscope. Without his enthusiasm to develop novel synthetic methods, several nanoparticles which I investigated during my thesis would have remained unexplored.

Olaf Schubert for his help in programming. Especially his presence in our group resulted in some nice common projects.

Andreas Henkel, who gave me a lot of advice in synthesizing and chemical modifying nanoparticles. By sharing his knowledge, he taught me a lot about chemistry.

Andreas Trügler and Ulrich Hohenester for providing me with their simulation software and for their willingness to implement models of further nanostructures. Without their help, the theoretical investigations of optical properties would have been very painful.

Christina Rosman and Dr. Sebastien Pierrat for a fantastic atmosphere in our office, where we could discuss different ideas spontaneously.

Dr. Luigi Carbone for the great time he spent in our group.

All members of the Institute for Physical Chemistry at the University of Mainz. Without their presence, the atmosphere at work would not have been so familial.

Thomas Sünner for many general discussions on physics and being a physicist.

In particular I would like to express enormous gratitude to my entire family.

Contents

Chapter 1
Introduction

Nano, a word derived from the Greek word $\nu\alpha\nu o\varsigma$ (nanos, which translated denotes "dwarf"), is nowadays a synonym for a whole research area—the nanosciences. One area within this huge research field is nano-optics, where the response of a nanoparticle to an incoming light wave is investigated. In detail, nanoparticles made of noble metals evoke a special interest, since these particles show a strong response to the incoming light wave. This attribute can be explained by the effect that the mentioned light wave excites the electrons in the conduction band to a collective oscillation. If the frequency of the incoming light matches the eigenfrequency of the electron-oscillation, a resonance occurs, which then leads to strong scattering and absorption of the incoming light. To allow a physical explanation of this phenomena, the collective oscillation of the electrons is described as a quasiparticle, which is termed *plasmon*.

Although this exceptional optical response was not understood in earlier times, already from the fourth century AD on, metallic nanoparticles were used to produce colorful glasses (e.g. window panels in churches). A first scientific report on the colors of metallic colloids dates back to Faraday (1857), but he was not able to give a qualitative explanation on the optical properties of the nanoparticles. These missing theoretical calculations were performed afterwards by Mie (1908), who solved Maxwell's equations. However, the theory obtained allows us to only calculate the optical properties of particles, which have a spherical shape. Later, Gans (1912) extended this theory, allowing the calculation of the optical properties also for spheroidal shaped particles. One main result of his theory is the explanation that the resonance wavelength increases with respect to the particles' elongation. Therefore, by varying the particles' length, the plasmon resonance of nanoparticles is tunable and covers for gold and silver the range of the visible spectrum. This makes these particles ideal samples for optical investigation.

Due to their very efficient light scattering properties in the visible range of the light, it is possible to investigate *individual* gold and silver nanoparticles optically, despite their very small size. To realize the optical investigation, a transmission light microscope in dark-field modus is used, where individual plasmonic nanoparticles

J. Becker, *Plasmons as Sensors*, Springer Theses,
DOI: 10.1007/978-3-642-31241-0_1, © Springer-Verlag Berlin Heidelberg 2012

appear as bright spots on a black background. Accomplishing a spectral investigation of these nanoparticles allows us to gain various information on the particles properties, like for example the determination of the particles' elongation already mentioned.

Another factor which influences the particle's spectral resonance position is the refractive index of the embedding medium. As a result of this factor, plasmonic nanoparticles can be used as sensors i.e. for the determination of some proteins, since these proteins have a higher refractive index compared to an initial pure aqueous solution. Therefore, these nanoparticles can be used as sensors in volumes on the attoliter scale.

In microscope systems used until now, the spectral investigation of individual nanoparticles was performed by positioning one nanoparticle in such a way, that its scattered light was imaged onto the entrance pinhole of a coupled spectrometer. Therein, the light was dispersed (by a grating or a prism) and was then captured by an appropriately installed CCD camera. Investigations of further particles were performed by their subsequent manual positioning. However, this approach is very time consuming and therefore obtaining statistics on many particles is impracticable. Furthermore, a continuous observation of several individual particles in parallel is not possible at all. To improve the measurement technique, I developed a novel fast single particle spectroscopy (fastSPS) setup, measuring automatically the spectra of all particles in the field of view with the possibility to monitor up to 30 particles continuously at the same time.

I used this novel setup for different investigations, e.g. to monitor the scattering spectra of nanoparticles during their growth process to obtain a further understanding of this mechanism. In another experiment, I applied membrane coated nanoparticles as sensors to investigate specific protein-membrane binding interactions. Furthermore, I showed that additional chemical modifications on gold nanorods result in a plasmonic sensitivity increase on refractive index changes, e.g. a larger shift in the nanoparticles' resonance wavelength when the refractive index in the environmental solution is changed by a given factor.

A second setup (RotPOL) was developed, which additionally allows us to measure the polarization of the scattered light of nanoparticles. Until now, in polarization dependent single particle studies, a polarization filter was rotated stepwise by hand, and the scattered light was measured therefore only at specifically selected angles of the polarizer without any spectral information. Naturally, this approach is unsatisfying and therefore an automatization, including the spectral information, was desired. The first part was realized by rotating a wedge-shaped polarizer with a motor. However, with this approach a typical spectrometer based on a grating (or prism) cannot be used to obtain the desired spectral information any more. For this reason, a special variable wavelength filter was implemented, which was automatically moveable. Since the wavelength dependent polarization of the scattered light depends strongly on the morphologies of the nanoparticle, this novel setup allowed us to gain new insights into the polarization anisotropy of differently shaped nanoparticles.

This work is organized as follows:

Initially, I will present theories and simulation methods to calculate the optical response of differently shaped particles to an incoming light wave and I will show some results obtained by various calculations (Chap. 2). For example, I show a dependency of the resonance wavelength on the particles' shape and material, on the refractive index of the medium and on the interparticle distance for two coupled gold nanospheres.

Chapter 3 will present the methods to synthesize the nanoparticles used during the presented work (i.e. gold nanorods and subsequent procedures to coat these particles with a silver shell or a porous gold cage and silver particles like cubes, rods and triangles). To characterize the particles, different analytical methods (e.g. extinction spectroscopy, darkfield microscopy, transmission electron microscopy) are available, which will be presented in Chap. 4.

Subsequently, in Chap. 5, I will present two novel spectroscopy approaches: the fast single particle spectroscopy (fastSPS) setup, where the entrance pinhole of the spectrometer is replaced by a liquid crystal device (LCD) acting as an addressable shutter. This approach allows us to investigate automatically all particles in the field of view and additionally offers the possibility to monitor the scattering spectra of up to 30 nanoparticles continuously in parallel. The second novel setup (RotPOL) enables the automatic investigation of the polarization anisotropy of non-spherical particles by a motor-driven rotation of a wedge-shaped polarizer.

The following chapters will present results of experiments performed on these novel setups. A study on the growth of single gold nanoparticles will be presented in Chap. 6, reporting on the preferentially growth of the short axis in a second step of the nanoparticle growth process. Additionally, a transfer function will be derived, which converts the measured single particle spectra into a particle geometry.

Chapter 7 will specify results of experiments where gold nanorods are used as sensors to detect protein binding onto a membrane by measuring the resulting spectral shift. Furthermore it will be shown that even different functionalizations of the membranes can be distinguished, since the evoking spectral shifts vary.

The sensitivity on changes in the refractive index of the environment depends on the particles' aspect ratio. Therefore, I will perform in Chap. 8 theoretical and experimental investigations and present the existence of an "optimal" aspect ratio. Furthermore, I will introduce a novel quantity (i.e. FOM*) allowing to compare the sensitivity of nanostructures with even complex shaped resonances.

As shown, the sensitivity on refractive index changes of gold nanorods can be optimized but has a given limit. Therefore, an additional improvement has to be achieved by chemical modifications of the gold nanorods. I will show in Chap. 9 that the fulfillment of further increase of the plasmonic sensitivity can be achieved by either a thin silver shell coating or by growing an additional porous gold cage.

The presented coating of a thin silver shell around gold nanorods evokes another improvement; the linewidth of the extinction spectrum is narrowed due to a change in the function connecting the particles' shape and its appropriate resonance wavelength. This change I term "plasmonic focusing" will be discussed in Chap. 10.

In Chap. 11, I will introduce a sensing approach consisting of two spherical particles. While the resonance wavelength of the longitudinal axis depends on the inter-particle distance and the refractive index of the environment, the resonance wavelength of the transversal axis depends solely on the refractive index. Hence, with this sensor the inter-particle distance can be determined even if the the refractive index of the local environment is not known.

Finally in Chap. 12 I will give a short summary of the work in this thesis.

References

Faraday, M. (1857). The Bakerian Lecture—On the Experimental Relations of Gold (and Other Metals) to Light. *Philosophical Transactions of the Royal Society of London, 147*, 145–181.

Gans, R. (1912). Über die Form ultramikroskopischer Goldteilchen. *Annalen der Physik, 342*(5), 881–900.

Mie, G. (1908). Beiträge zur Optik trüber Medien, speziell kolloidaler Metallösungen. *Annalen der Physik, 25*(3), 377–445.

Chapter 2
Light-Scattering and -Absorption of Nanoparticles

To understand the optical response of nanoparticles to the incident light, a theoretical description is needed, which is given in this chapter. In a first approximation, these optical properties can be described using a quasi-static model, which assumes a particle-size much smaller than the wavelength of the light. The derivation of the polarizability of a sphere, which describes its optical properties, and further extensions for spheroidal, rod-shaped and coated particles are given in Sect. 2.2. Gustav Mie calculated an exact analytical description of the optical properties for spherical particles, which is briefly summarized in Sect. 2.3 for uncoated as well as for coated spheres. For particles with an arbitrary shape, numerical methods have to be used to calculate their optical properties. In Sect. 2.4 I describe two different simulation methods (discrete dipole approximation and boundary element method) used in this thesis. The obtained theory and simulation methods are used to investigate various parameters influencing the scattering spectrum of nanoparticles (Sect. 2.5), like the particles' shape and the consisting material. For gold nanorods the resonance position is calculated in dependency of the refractive index of the embedding medium, as well as for different water temperatures. Furthermore, the influence of a substrate (nanoparticles are often immobilized on) is investigated and an impression of the scattering cross-sections of gold nanoparticles compared to silica-spheres is gained. Additionally, the resonance wavelength and optical response of a dimer consisting of two spherical gold nanospheres is calculated for different interparticle distances.

2.1 Introduction

In general there exist two possibilities for the light interacting with a nanoparticle: either it is scattered or it can be absorbed by the particle. These two optical properties of the nanoparticle are described by the frequency dependent cross-sections C_{sca} and C_{abs}, which allow the calculation of the amount of scattered and absorbed light, respectively:

J. Becker, *Plasmons as Sensors*, Springer Theses,
DOI: 10.1007/978-3-642-31241-0_2, © Springer-Verlag Berlin Heidelberg 2012

$$I_{\text{sca}} = \frac{I_0(\omega)}{A} \cdot C_{\text{sca}}, \quad I_{\text{abs}} = \frac{I_0(\omega)}{A} \cdot C_{\text{abs}} \tag{2.1}$$

$I_0(\omega)/A$: light intensity per area the particle is irradiated with

The amount of the transmitted light I_{trans} is then: $I_{\text{trans}} = I_0 - (I_{\text{sca}} + I_{\text{abs}})$, where the sum in the brackets is also denoted as the *extinction* (with $C_{\text{ext}} = C_{\text{sca}} + C_{\text{abs}}$). Usually the cross-sections are normalized to the effective particle cross-section (e.g. πr^2 for a sphere with radius r, or $\pi(a \cdot b^2)^{2/3}$ for a spheroid with a short and a long semiaxis a and b, respectively), which results in the efficiencies Q_{sca}, Q_{abs} and Q_{ext}.

2.2 Quasi-Static Approximation

The first qualitative scientific studies on the optical properties of metallic colloids date back to Michael Faraday in 1857 (Faraday 1857). However, he was not able to give a theory on the optical properties of the particles, which was afterwards performed in a first approximation by Lord Rayleigh in 1871 (Strutt 1871a,b,c; Rayleigh 1899). He assumed a particle, which is much smaller compared to the wavelength of the incident light. Therefore the assumption of a constant electromagnetic phase through the whole particle can be made. This has the advantage that simple electro-statics can be used to calculate the optical properties of those small particles.

The scattering C_{sca} and absorption cross-section C_{abs} in SI-units are then given by Bohren and Huffman (1983):

$$C_{\text{sca}} = \frac{k^4}{6\pi\epsilon_0^2} |\alpha|^2, \quad C_{\text{abs}} = \frac{k}{\epsilon_0} \Im(\alpha) \tag{2.2}$$

$k = 2\pi\sqrt{\epsilon_m}/\lambda$: wavevector
ϵ_m: dielectric function of the embedding medium
λ: wavelength of the light in vacuum
$\epsilon_0 = 8.854 \cdot 10^{-12} \frac{\text{A s}}{\text{V m}}$: vacuum permittivity
α: polarizability of the particle $\left[\frac{\text{A s m}^2}{\text{V}}\right]$

2.2.1 Derivation of the Polarizability

For the calculation of the scattering C_{sca} and the absorption cross-section C_{abs} of nanoparticles, the polarizability α of the particle is needed according to Eq. 2.2. Here I want to give the derivation of the polarizability for a spherical nanoparticle within the quasi-static-approximation (Greiner 1991; Nolting 1997).

In contrast to a gas, where the molecules have a large distance between each other and therefore the electric polarization of a single molecule is not influenced by

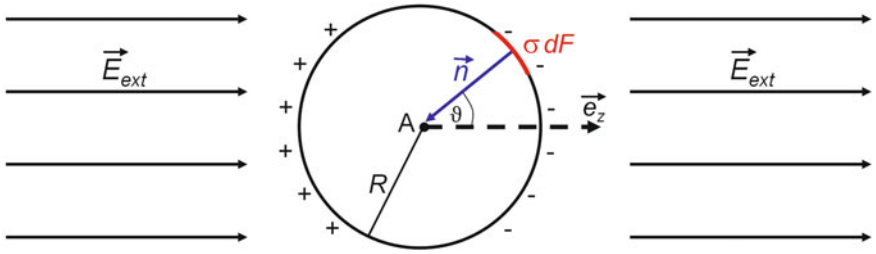

Fig. 2.1 To calculate the total local electric field $\vec{E}_{\text{loc}}$ at the position of one single lattice atom A the electric field $\vec{E}_{\text{L}}$ due to the polarization of the remaining atoms in the particle has to be added to the external electric field $\vec{E}_{\text{ext}}$. For this purpose a spherical volume with radius R around A is examined, which contains no other atoms except the selected one. $\vec{E}_{\text{L}}$ creates a surface charge $\sigma\, dF$ on the surface of the spherical volume with the normal vector $\vec{n}$

neighbored molecules, in a solid state the calculation of the polarization of a lattice-atom has to take the interaction between neighbored atoms into account. The electric polarization of a lattice atom depends in this case not only on the external electric field, but also on an additional field occurring from the polarization of the remaining atoms in the particle . The local electric field $\vec{E}_{\text{loc}}$ at the position of a single selected lattice atom has three parts:

$$\vec{E}_{\text{loc}} = \vec{E}_{\text{ext}} + \vec{E}_{\text{inter}} + \vec{E}_{\text{L}} \tag{2.3}$$

$\vec{E}_{\text{ext}}$: external electric field
$\vec{E}_{\text{inter}}$: electric field, due to the electrostatic interaction of neighboring lattice atoms
$\vec{E}_{\text{L}}$: electric field, due to polarization of atoms in the remaining crystal

The electric field $\vec{E}_{\text{inter}}$ depends on the crystal structure. Assuming a cubic lattice, where all atoms have their dipole moment in the direction of the external electric field, it can be shown that the contributions of all atoms cancel out and therefore (Nolting 1997):

$$\vec{E}_{\text{inter}} = 0 \tag{2.4}$$

To calculate $\vec{E}_{\text{L}}$ (also named Lorentz-field), a spherical volume around one single selected lattice atom is examined. This volume implies two assumptions: the arrangement of the dipoles outside the spherical volume is continuous and the volume itself contains no further atoms except the selected one. The charges on the surface of the spherical volume create thus the electric field $\vec{E}_{\text{L}}$ at the position of the lattice atom (Fig. 2.1).

The external electric field $\vec{E}_{\text{ext}}$ causes a parallel polarization $\vec{P}$, which creates on the surface of the spherical volume a surface-charge density σ according to:

$$\sigma = \vec{P} \cdot \vec{n} = -P \cos\vartheta \tag{2.5}$$

ϑ: angle between examined surface element and direction of $\vec{E}_{\text{ext}}$
$\vec{n}$: normal vector of the surface element, pointing into the center

In a small part of the surface dF the surface charge q is therefore σdF, and its electric field according to Coulomb's law is:

$$E = \frac{1}{4\pi\epsilon_0}\frac{q}{R^2} = \frac{1}{4\pi\epsilon_0}\frac{\sigma\, dF}{R^2} \tag{2.6}$$

R: radius of the spherical volume

The part in the direction of the external electric field $\vec{E}_{\text{ext}}$ is:

$$\vec{E} = \frac{1}{4\pi\epsilon_0}\frac{\sigma\, dF}{R^2}\cos\vartheta \cdot \vec{e}_z \tag{2.7}$$

Integration around the whole surface of the spherical volume and subsequently inserting Eq. 2.5 leads to:

$$\vec{E}_{\text{L}} = -\oint \vec{E} = -\frac{1}{4\pi\epsilon_0}\oint \frac{\sigma\, dF}{R^2}\cos\vartheta\, \vec{e}_z = +\frac{1}{4\pi\epsilon_0}\oint \frac{dF\, P}{R^2}\cos^2\vartheta\, \vec{e}_z \tag{2.8a}$$

$$= \frac{1}{4\pi\epsilon_0}\int_0^{2\pi} d\vartheta \int_0^{\pi} d\varphi \frac{P}{R^2}\cos^2\vartheta\ \sin\vartheta\ R^2\, \vec{e}_z \tag{2.8b}$$

$$= \frac{1}{4\pi\epsilon_0}\int_0^{2\pi} d\vartheta \int_0^{\pi} d\varphi\ P\cos^2\vartheta\ \sin\vartheta\, \vec{e}_z \tag{2.8c}$$

$$= \frac{1}{4\pi\epsilon_0} P\, 2\pi \left[-\frac{cos^3\vartheta}{3}\right]_0^{\pi} \vec{e}_z \tag{2.8d}$$

$$= \frac{1}{3\epsilon_0} P\, \vec{e}_z \tag{2.8e}$$

Since a positive charge $\sigma\, dF$ creates a field component in negative z-direction at the position of the examined lattice atom, the Eq. 2.8a needs a negative prefix.

For the calculation of the polarizability α the following definition has to be used:

$$\vec{P} = N\alpha\vec{E}_{\text{loc}} \tag{2.9}$$

N: number of dipoles per volume V

This equation can be converted by inserting the Eqs. 2.8e and 2.4 into Eq. 2.3:

$$\vec{P} = N\ \alpha\ \left(\vec{E}_{\text{ext}} + \frac{1}{3\epsilon_0}\vec{P}\right) \tag{2.10}$$

and can be solved for $\vec{P}$:

$$\vec{P} = \frac{N\,\alpha}{1 - \frac{1}{3\epsilon_0} N\,\alpha}\,\vec{E}_{\text{ext}} \tag{2.11}$$

Using now the definition of the dielectric susceptibility χ:

$$\vec{P} = \epsilon_0\,\chi\,\vec{E}_{\text{ext}} \tag{2.12}$$

Equation 2.11 can be written as:

$$\vec{P} = \frac{N\,\alpha}{1 - \frac{1}{3\epsilon_0} N\,\alpha}\,\frac{\vec{P}}{\epsilon_0\,\chi} \tag{2.13}$$

Canceling out $\vec{P}$ and solving the equation to χ leads to:

$$\chi = \frac{N\,\alpha}{\epsilon_0 - \frac{N\,\alpha}{3}} \tag{2.14}$$

The dielectric susceptibility χ is connected with the relative dielectric complex constant ϵ_r via:

$$\epsilon_\text{r} = 1 + \chi \tag{2.15}$$

while ϵ_r is defined as:

$$\epsilon_\text{r} = \epsilon'_\text{r} + i\epsilon''_\text{r} = \epsilon_p/\epsilon_m \tag{2.16}$$

ϵ_p: dielectric function of the particles' material
ϵ_m: dielectric function of the embedding medium

In the case of one particle, the whole particle can be considered as a single dipole, and therefore the number of dipoles per volume is: $N = 1/V$, where V is the particle volume. Together with Eqs. 2.15 and 2.14 can be transformed into the Clausius–Mossotti relation:

$$\alpha = 3\epsilon_0 V \frac{\epsilon_r - 1}{\epsilon_r + 2} \tag{2.17}$$

Using the Eq. 2.2, the scattering and absorption cross-sections can be transformed into:

$$C_{\text{sca}} = \frac{k^4}{6\pi}\left(3V^2\right)\frac{\left(\epsilon'_r - 1\right)^2 + \epsilon''^2_r}{\left(2 + \epsilon'_r\right)^2 + \epsilon''^2_r}, \quad C_{\text{abs}} = 3kV\frac{3\epsilon''_r}{\left(2 + \epsilon'_r\right)^2 + \epsilon''^2_r} \tag{2.18}$$

Relation of Refractive Index to Dielectric Function

The dielectric function $\epsilon = \epsilon' + i\epsilon''$ of a material contains a real part ϵ' and the imaginary part ϵ'' (see Eq. 2.16). However, the optical properties of materials are

often given in the complex index of refraction $\widetilde{n}$ (Johnson and Christy 1972):

$$\widetilde{n} = n + i\kappa \tag{2.19}$$

n: refractive index, defined as the ratio between the speed of light in vacuum and the phase velocity of light in that medium
κ: extinction coefficient, connected to the amount of absorption

(Note that the sign of the complex part is a matter of convention.)
Since the relation of the complex refractive index $\widetilde{n}$ and the dielectric function ϵ is defined as $\epsilon = \widetilde{n}^2$, the real and imaginary part of ϵ can be calculated according to:

$$\epsilon' = n^2 - \kappa^2, \quad \epsilon'' = 2 \cdot n\kappa \tag{2.20}$$

The backtransformation can be performed by:

$$n = \pm\sqrt{\frac{\sqrt{\epsilon'^2 + \epsilon''^2} + \epsilon'}{2}}, \quad \kappa = \pm\sqrt{\frac{\sqrt{\epsilon'^2 + \epsilon''^2} - \epsilon'}{2}} \tag{2.21}$$

2.2.2 QSA for Nano Spheroids

The derivation of the polarizability α was performed for spherical particles. However, within the quasi-static approximation the optical properties of ellipsoidal particles (described by three semiaxes ($a \geq b \geq c$)) can also be calculated, if a geometrical factor is introduced. This extension was performed by Gans (1912), who determined the polarizability α_i of a spheroid along the axis i according to Bohren and Huffman (1983):

$$\alpha_i = V\epsilon_0 \frac{\epsilon_r - 1}{1 + L_i(\epsilon_r - 1)} \tag{2.22}$$

L_i: geometrical factor related to the examined axis

The relationship existing for an ellipsoid is: $L_a + L_b + L_c = 1$ (Osborn 1945) and therefore for spheres accounts to $L_a = L_b = L_c = 1/3$, which recovers in this case Eq. 2.17. For spheroidal particles L_i is given by Myroshnychenko et al. (2008):

$$L_i = \frac{a \cdot b \cdot c}{2} \int_0^\infty \frac{1}{(s + l_i^2)\sqrt{(s + a^2)(s + b^2)(s + c^2)}} \mathrm{d}s \tag{2.23}$$

l_i: length of the examined axis (a, b or c)

However, of particular interest are the shapes having two axes with the same length (named *spheroids*), either *prolates* ($a \geq b = c$) or *oblates* ($a = b \geq c$). For a prolate particle the geometrical factor is Kooij and Poelsema (2006):

$$L_a = \frac{1-e^2}{e^2}\left(-1 + \frac{1}{2e}\ln\frac{1+e}{1-e}\right) \tag{2.24}$$

$$L_b = L_c = \frac{(1-L_a)}{2} \tag{2.25}$$

$e = \sqrt{1 - b^2/a^2}$: eccentricity.

It was found that the geometrical factor L_a of the long axis for prolate particles can be approximated (for $1 \leq \mathrm{AR} \leq 19$) by following equation Sönnichsen (2001):

$$L_a = \left(1 + \frac{a}{b}\right)^{-1.6} \tag{2.26}$$

For oblate (pancake shaped) spheroids with $a = b \geq c$ the geometrical factors are given by Bohren and Huffman (1983):

$$L_a = L_b = \frac{g(e)}{2e^2}\left[\frac{\pi}{2} - \arctan g(e)\right] - \frac{g^2(e)}{2} \tag{2.27}$$

$$L_c = 1 - 2 \cdot L_a \tag{2.28}$$

where $g(e)$ is given by:

$$g(e) = \left(\frac{1-e^2}{e^2}\right)^{1/2}, \quad e^2 = 1 - \frac{c^2}{a^2} \tag{2.29}$$

Similar to the fit-equation 2.26 describing the geometrical factor of the long axis for prolates, this value can also be approximated for oblate spheroidal particles in respect of the aspect ratio AR (i.e. a/c) for values $1 \leq \mathrm{AR} \leq 10$ according to (Fig. 2.2):

$$L_a = L_b = 0.647 \cdot (1 + \mathrm{AR})^{-0.92} \tag{2.30}$$

Inserting Eq. 2.22 into the Eq. 2.2 with the appropriate values for the geometrical factor reveals the scattering and absorption cross-section for spheroidal shaped particles in the quasi-static approximation. A result which can be derivated from these calculation is, that an increase of the aspect ratio (long axis/short axis) of the particle leads to a higher resonance wavelength (equipollent to a decrease of the resonance energy) of the long axis.

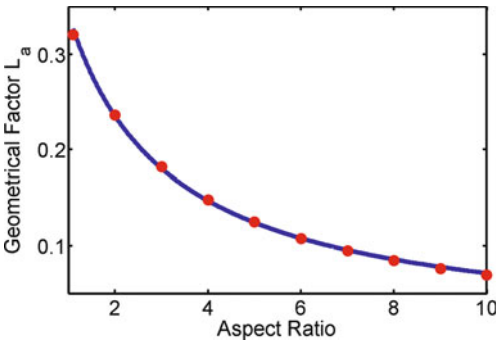

Fig. 2.2 The geometrical factor L_a and L_b of the long axis of a oblate shaped spheroid can be described by the simple approximation of Eq. 2.30 (*blue line*). The *red dots* mark the exact values calculated by Eq. 2.27

2.2.3 QSA for Coated Spheroids

The nanoparticles used in this work are often coated with a shell having a different dielectric function than the embedding medium. For example silver coated gold nanorods in aqueous solution were synthesized and it was shown, that the resonance wavelength and the single particle linewidth are decreasing due to this coating (Sects. 3.2 and 9.2). Another application was to coat gold nanorods in water ($n = 1.33$) with a membrane, having an assumed refractive index of $n = 1.5$, which leads to a redshift of the plasmon resonance (Chap. 7). A first approach to simulate these particles would be to use an "effective" dielectric function, which is a mixture of the dielectric functions of the particle and the coating material. However, core-shell particles show a completely different spectrum compared to alloyed particles (Kim et al. 2002). Therefore, a theory on the core-shell particles is needed for further understanding of their spectra. For a coated prolate spheroid with the total length of the semiaxis ($a_2 \geq b_2 = c_2$) and a core size of ($a_1 \geq b_1 = c_1$) the polarizability in the quasi-static approximation is given by Liu and Guyot-Sionnest (2004):

$$\alpha_i = \epsilon_0 V' \frac{\left\{(\epsilon_s - \epsilon_m)\left[\epsilon_s + (\epsilon_p - \epsilon_s)\left(L_i^{(1)} - f L_i^{(2)}\right)\right] + f\epsilon_s(\epsilon_p - \epsilon_s)\right\}}{\left[\epsilon_s + (\epsilon_p - \epsilon_s)\left(L_i^{(1)} - f L_i^{(2)}\right)\right]\left[\epsilon_m + (\epsilon_s - \epsilon_m) L_i^{(2)}\right] + f L_i^{(2)} \epsilon_s (\epsilon_p - \epsilon_s)} \tag{2.31}$$

$V' = \frac{4}{3}\pi\, a_2 \cdot b_2 \cdot c_2$: total volume of the particle
$f = (a_1 \cdot b_1 \cdot c_1)/(a_2 \cdot b_2 \cdot c_2)$: fraction of particle volume occupied by inner spheroid
ϵ_s: dielectric function of the shell material

and with the geometrical factors L_i^k (with $k = 1, 2$):

$$L_i^k = \frac{1-e_k^2}{e_k^2}\left(-1+\frac{1}{2e_k \ln\frac{1+e_k}{1-e_k}}\right) \tag{2.32}$$

$e_k = \sqrt{1-(b_k^2)/(a_k^2)}$: eccentricity.

In the case of no coating of the spheroid, this equation reduces to Eq. 2.22.

For spherical particles this equation can be simplified, since the geometrical factor is $L_i^k = 1/3$ for any case ($i = 1, 2, 3$ and $k = 1, 2$). Therefore the polarizability for a sphere with a total radius of r_2 and an inner radius of r_1 can be displayed as Myroshnychenko et al. (2008):

$$\alpha = \epsilon_0 3V' \frac{(r_2/r_1)^3\left(2\epsilon_s+\epsilon_p\right)\left(\epsilon_s-\epsilon_m\right)-\left(\epsilon_s-\epsilon_p\right)\left(2\epsilon_s+\epsilon_m\right)}{(r_2/r_1)^3\left(2\epsilon_s+\epsilon_p\right)\left(\epsilon_s+2\epsilon_m\right)-2\left(\epsilon_s-\epsilon_p\right)\left(\epsilon_s-\epsilon_m\right)} \tag{2.33}$$

which recovers Eq. 2.17 in the case of no coating.

2.2.4 Extension for Gold Nanorods

As shown in Eq. 2.22 the polarizability α of a spheroid could be analytically calculated by implementing a geometrical factor L, which enables the determination of the optical properties with respect to their aspect ratio AR. However, the gold particles I used in the present work are described more precisely by a rodshape. Since these differences in the particles' shape lead already for particles with the same aspect ratio to a change in the plasmon resonance spectrum, an appropriate extension for nanorods is necessary. However, the polarizability α of rodshaped nanoparticles could not be performed analytically, therefore Prescott and Mulvaney simulated the extinction spectra of gold nanorods numerically by the discrete dipole approximation (DDA, Sect. 2.4.1) and determined the appropriate geometrical factors L by fit-functions Prescott and Mulvaney (2006).

While in the quasi-static approximation the absolute size of the particles is not considered, the spectra determined by the DDA depend on this factor. For this reason the values for L obtained within this numerical way varies for rods with different diameters. Furthermore, Prescott and Mulvaney found out that also the morphology of the endcaps of the rods influences the resonance. Therefore they calculate the eccentricity e of the endcap according to following equation, where the endcap structure is described by the dimensions d and b as shown in Fig. 2.3a:

$$e = \sqrt{1-\frac{d^2}{b^2}} \tag{2.34}$$

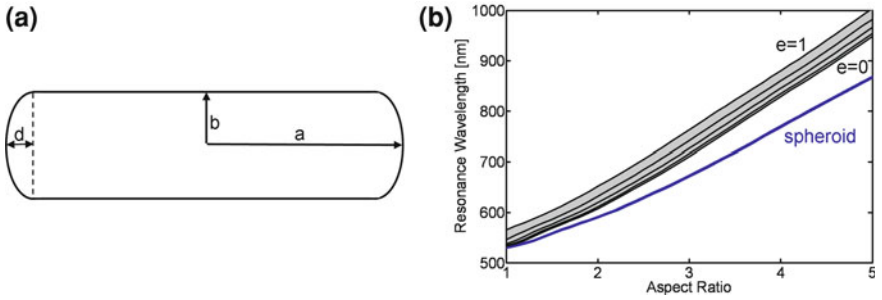

Fig. 2.3 **a** Scheme of the particle morphology for a rod with an ellipsoidally shaped capped cylinder. The eccentricity e is calculated by: $e^2 = 1 - d^2/b^2$, with the limits of a rod with spherical endcaps ($e = 0$) and no endcaps (i.e. just a cylinder, with $e \to 1$). **b** The resonance wavelength in respect to the aspect ratio for spheroidal gold nanoparticles is represented by the *blue line*. For gold nanorods having endcaps with an eccentricity $0 < e < 1$ the resonance wavelength is displayed by the grayish area. The *solid black lines* represents resonances for eccentricity values of ($e = 0, 0.5, 0.8, 0.95, 1$) according to Table 2.1

Table 2.1 Quadratic parameters to fit the geometrical factors for a $b = 10$ nm radius (i.e. 20 nm in diameter) gold nanorod with different endcaps, which are described by the eccentricity e

Morphology endcap	c_1	c_2	c_3
$e = 0$	0.4532	2.0100	−0.3072
$e = 0.5$	0.4495	2.0856	−0.2903
$e = 0.8$	0.4420	2.2417	−0.2489
$e = 0.95$	0.4378	2.3786	0.0144
$e = 1$	0.4473	2.4262	0.6937

The geometrical factor L can be calculated then via Eq. 2.35. Values for rod with different diameter are listed in Ref. Prescott and Mulvaney (2006) and in Prescott and Mulvaney (2008)

within the limits of a spherical endcap morphology ($e = 0$) and no endcaps (i.e. just a cylinder, with $e \to 1$).

They found out that for rods with varying aspect ratio AR but with fixed diameter and eccentricity the geometrical factor can be described by a quadratic polynomial:

$$\frac{1 - L}{L} = c_1 \cdot \mathrm{AR}^2 + c_2 \cdot \mathrm{AR} + c_3 \tag{2.35}$$

The constants (c_1, c_2, c_3) for a rod with $b = 10$ nm and different endcaps can be found in Table 2.1 [values for rods with a different radius b are listed in Ref. Prescott and Mulvaney (2006) and in Prescott and Mulvaney (2008)].

The calculated resonance wavelengths for rods in aqueous solution with different endcap morphologies are shown in Fig. 2.3b. It can be seen, that for a constant aspect ratio the resonance wavelength increases, if the eccentricity of the endcap becomes larger. For comparison the resonance wavelengths of spheroidal shaped gold

nanoparticles are also plotted, which are consistently smaller than the resonances of the rodshaped particles with the same aspect ratio.

The values for the geometrical factor can also be used for the calculations for gold nanorods coated with a thin silver shell. For this purpose the geometrical factor of the spheroid in Eq. 2.22 has to be replaced with the appropriate geometrical factor of gold rods. For this reason the spectrum of gold nanorods with known aspect ratio (from TEM images) was calculated with a matching geometrical factor. Afterwards a thin silver shell was grown on the rods and its thickness was determined again by TEM. Using Eq. 2.31 with the same geometrical factor to calculate the spectrum of the bare gold nanorods, the observed spectrum of the silver coated gold nanorods could be reproduced (Sect. 10.5).

2.3 Mie-Theory

However, the quasi-static approximation assumes a constant electric field in the particle, which is reasonable for particles much smaller compared to the wavelength of the light. For larger particles, the electric field of the electromagnetic wave is not constant any more and the retardation effect takes place. Particularly, opposite charges are separated over the particle's diameter (in dipole mode). Due to the finiteness of the speed of light, a change in one end of the particle leads to a reaction in the opposite end with a certain phase delay. Consequently, the period of one mode oscillation increases to accommodate this delay, which leads to a redshift of the resonance wavelength. Since the phase delay depends on the separation distance of the charges and thus on the diameter of the particle, the redshift is larger for increasing particle size (Fig. 2.4). For spherical gold particles the resonance wavelength can be approximated in dependency on the particles diameter d (in the range $10 \leq d \leq 150\,\text{nm}$) according to following equation (Fig. 2.4):

$$\lambda_{\text{res}}\,[\text{nm}] = 529.8\,[\text{nm}] + 8.3 \cdot 10^{-4} \cdot (d/[\text{nm}])^{2.37}\,\,[\text{nm}] \tag{2.36}$$

Furthermore, the quasi-static approximation neglects that the electromagnetic field cannot penetrate beyond a certain depth inside the metal (so-called skin-depth, about 15 nm for gold in the visible range of the light), which also effects the resonance of the particle (Myroshnychenko et al. 2008).

An exact analytical calculation of the optical properties for spherical particles was found by Mie (1908), who solved Maxwell's equations Maxwell (1865) in spherical coordinates. He calculated for the scattering and the extinction cross-sections (Bohren and Huffman 1983) for a sphere with radius r:

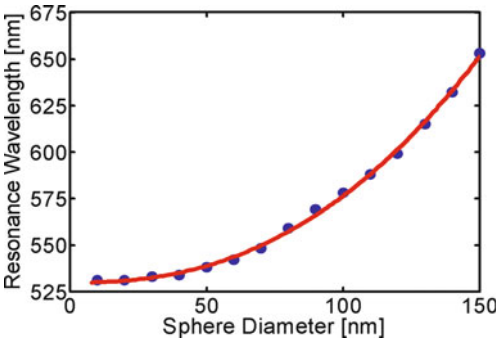

Fig. 2.4 The resonance wavelength of gold nanospheres depends on the particles' diameter due to retardation. This effect occurs since the speed of light is finite, and changes in one particles end leads to a reaction in the opposite end with a certain phase delay, which leads to a *redshift* of the resonance wavelength. The spectra are calculated using Mie's theory and can be fitted by Eq. 2.36

$$C_{\text{sca}} = \frac{2\pi}{k^2} \sum_{l=1}^{\infty} (2l+1)(|a_l|^2 + |b_l|^2) \tag{2.37}$$

$$C_{\text{ext}} = \frac{2\pi}{k^2} \sum_{l=1}^{\infty} (2l+1)\ Re(a_l + b_l) \tag{2.38}$$

$k = 2\pi \frac{\sqrt{\epsilon_m}}{\lambda}$: wave vector
λ: wavelength of the electromagnetic wave

and a_n, b_n are the Mie coefficients, which are calculated by:

$$a_l = \frac{m\psi_l(mx)\psi_l'(x) - \psi_l(x)\psi_l'(mx)}{m\psi_l(mx)\xi_l'(x) - \xi_l(x)\psi_l'(mx)} \tag{2.39}$$

$$b_l = \frac{\psi_l(mx)\psi_l'(x) - m\psi_l(x)\psi_l'(mx)}{\psi_l(mx)\xi_l'(x) - m\xi_l(x)\psi_l'(mx)} \tag{2.40}$$

$m = \sqrt{\epsilon_r} = n_p/n_m$: relative refractive index of the particle
$x = 2\pi\sqrt{\epsilon_m} r/\lambda$: size parameter
ψ_l and ξ_l: Riccati-Bessel functions

while $l = 1$ describes the dipole mode of the resonance, $l = 2$ calculates its quadrupole mode. Consequently larger l-values describe modes of higher order.

For small radii an approximation for the polarizability can be obtained, which includes in contrast to Rayleigh's approximation given in Eq. 2.17 the retardation effects (Myroshnychenko et al. 2008):

$$\alpha_{\text{Mie}} = 3\epsilon_0 V \frac{\frac{1}{\epsilon_m} - 0.025\,(\epsilon_r + 1)\,\theta^2}{\frac{1}{\epsilon_m}\frac{\epsilon_r+2}{\epsilon_r-1} - 0.25\,(0.1\epsilon_r + 1)\,\theta^2 - i\sqrt{\epsilon_m}\,\frac{2}{3}\,\theta^3} \tag{2.41}$$

$\theta = \frac{2\pi r}{\lambda}$: size Parameter
r: radius of the sphere

The second term of the denominator is the correction for the dipolar plasmon shift due to the retardation effect. The third-order term is pure imaginary and represents the radiative loss (Kuwata et al. 2003). For $\theta = 0$ the electrostatic limit in the Rayleigh scattering given by Eq. 2.17 is recovered. The scattering and absorption cross-sections can then be calculated by inserting α_{Mie} into Eq. 2.2.

2.3.1 Mie Theory for Coated Spheres

The Mie theory also allows to calculate the scattering and extinction cross-sections for coated spheres, which includes in contrast to Eq. 2.33 the consideration of retardation effects and the skin-depth. For a sphere with a total radius r_2 and a spherical core with radius r_1, where the shell is homogeneous and of uniform thickness, the cross-sections can be calculated by Eqs. 2.37 and 2.38 but in this case with the Mie coefficients given by Kim et al. (2002):

$$a_l = \frac{\psi_l(y)\left[\psi_l'(m_2 y) - A_l\,\chi_l'(m_2 y)\right] - m_2\psi_l'(y)\left[\psi_l(m_2 y) - A_l\,\chi_l(m_2 y)\right]}{\xi_l(y)\left[\psi_l'(m_2 y) - A_l\,\chi_l'(m_2 y)\right] - m_2\xi_l'(y)\left[\psi_l(m_2 y) - A_l\,\chi_l(m_2 y)\right]} \tag{2.42}$$

$$b_l = \frac{m_2\psi_l(y)\left[\psi_l'(m_2 y) - B_l\,\chi_l'(m_2 y)\right] - \psi_l'(y)\left[\psi_l(m_2 y) - B_l\,\chi_l(m_2 y)\right]}{m_2\xi_l(y)\left[\psi_l'(m_2 y) - B_l\,\chi_l'(m_2 y)\right] - \xi_l'(y)\left[\psi_l(m_2 y) - B_l\,\chi_l(m_2 y)\right]} \tag{2.43}$$

where

$$A_l = \frac{m_2\psi_l(m_2 x)\psi_l'(m_1 x) - m_1\psi_l'(m_2 x)\psi_l(m_1 x)}{m_2\chi_l(m_2 x)\psi_l'(m_1 x) - m_1\chi_l'(m_2 x)\psi_l(m_1 x)} \tag{2.44}$$

$$B_l = \frac{m_2\psi_l(m_1 x)\psi_l'(m_2 x) - m_1\psi_l(m_2 x)\psi_l'(m_1 x)}{m_2\chi_l'(m_2 x)\psi_l(m_1 x) - m_1\psi_l'(m_1 x)\chi_l(m_2 x)} \tag{2.45}$$

$m_1 = \sqrt{\epsilon_{r1}} = n_p/n_m$: relative refractive index of the core
$m_2 = \sqrt{\epsilon_{r2}} = n_s/n_m$: relative refractive index of the shell
$x = 2\pi\sqrt{\epsilon_m} r_1/\lambda$: size parameter of the core
$y = 2\pi\sqrt{\epsilon_m} r_2/\lambda$: size parameter of the whole particle
$\chi_l(\rho)$: Riccati-Bessel function corresponding to the y_l Bessel function

The calculations according to Mie's theory for uncoated as well as for coated spheres in this work where performed with a commercial software.

Table 2.2 Comparison of advantages and disadvantages of DDA and BEM (Myroshnychenko et al. 2008)

	DDA	BEM
Number of discretization points	$\propto$ Volume	$\propto$ Volume$^{2/3}$
Advantages	• Simple parametrization	• Low computational time and storage demand
Disadvantages	• Time consuming	• Complex parameterization

2.4 Numerical Methods

As described before, exact analytical expressions revealing the optical response of nanoparticles to an incoming light wave only exist for spherical particles. In a first approximation also spheroidal particles can be calculated, if retardation effects and the skin-depth of the material are neglected. To calculate the exact optical response of arbitrary shaped particles, numerical methods have to be used. In this work I used two different ones: either discrete dipole approximation (DDA) or the boundary element method (BEM), which I want to describe briefly in the next two sections.An overview of the advantages and disadvantages of both methods is given in Table 2.2.

2.4.1 Discrete Dipole Approximation

The DDA describes a particle of arbitrary shape as an array of N polarizable dipolar elements (Fig. 2.5a). As a response to the local electric field, these elements acquire a dipole moment. Hence, the local field experienced by each individual dipole is constituted by both the external field arising from the incident illumination and the internal field generated by all other dipoles. The polarizability of each element can be obtained from the Clausius–Mossotti relation (Eq. 2.17) using the volume of each element as input and the dielectric constant of the embedding medium in which the particle is placed (Myroshnychenko et al. 2008). The number N of dipoles, which is required to provide an accurate description of the target, is subject to optimization. On the one hand, N should be large (typically $N > 10^4$) to prevent spurious surface effects. Since the ratio of surface to bulk dipoles decreases with increasing N, and therefore these surface effects vanish, a very large number of dipoles N would be favorable. However, computational time increases approximately proportional to N^3, which suggests to choose N as small as possible. For the same reason particles coated with a thin shell cannot be calculated with DDA: to describe a small shell, the dipole distance in this shell has to be chosen very small, since the thickness should consist at least of 10 dipoles. Since the dipole distance has to be constant all over the particle, the number of dipoles increases dramatically in this case. Next to enormous

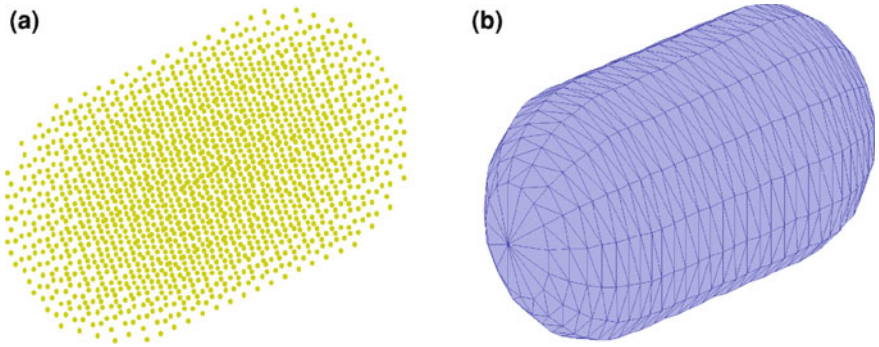

Fig. 2.5 Scheme how a particle is discretized within the (**a**) discrete-dipole approximation (DDA) and (**b**) (the boundary element method (BEM). While in DDA the whole particle is described by an array of N polarizable dipolar elements, in BEM the surface of the particle is discretized into N' surface elements)

computational time needed also the demanded RAM data storage is too large for the computer cluster of the University of Mainz.

The DDA simulations obtained in this work were performed with the software DDSCAT 6.1 published by Draine and Flateau and can be downloaded free of charge (Draine and Flatau 2004).

2.4.2 Boundary Element Method

The electromagnetic field inside each homogeneous region in a composite material is unambiguously determined by the fields and their derivatives at the *boundary of that region*, or equivalently by a distribution of charges and currents on that boundary. The boundary element method (BEM) expresses the electromagnetic field scattered by a nanoparticle in terms of these boundary charges and currents. Imposing the customary boundary conditions for the continuity of the parallel components of the electric and magnetic fields leads to a system of surface-integral equations. This system is solved by discretizing the integrals using a set of N' representative points distributed at the boundaries (Fig. 2.5b). Therefore the system turns into a set of linear equations that are solved numerically by standard linear-algebra techniques. Since only the surface of the particle needs to be parameterized, the number of elements N' is much smaller compared to the numbers needed in DDA.

A software based on the boundary element method used here was written by Andreas Trügler and Ulrich Hohenester from the University of Graz (Austria) and was kindly provided for my simulations. Currently they also work on an extension, which then allows to simulate the optical response of core-shell nanoparticles.

2.5 Results Obtained by Theory and Simulations

The presented theory and simulation methods are used to calculate the resonance position of rodshaped gold nanoparticles with varying aspect ratio. To find thereafter the smallest possible spectral linewidth of plasmonic particles, the same calculation was performed with particles consisting of different materials. For gold nanorods, the resonance wavelength is calculated in dependency of the refractive index of the embedding medium, as well as for different water temperatures. Simulation methods are also used to investigate the influence to the resonance wavelength of a substrate gold nanorods are often immobilized on. Furthermore, the scattering cross-section of gold nanoparticles and silica spheres are compared to get an impression on the scattering efficiency of gold nanoparticles. Additionally, I simulated the scattering spectrum of a dimer consisting of two spherical gold spheres to investigate the resonance position in respect of the interparticle distance, due to plasmon coupling.

2.5.1 Resonance Dependency on Shape of the Particles

According to Eq. 2.22 the longitudinal resonance wavelength along the long axis of spheroids depends on the particles' aspect ratio. To show that the same issue occurs also for rodshaped particles, I simulated the scattering spectrum of these particles with the boundary element method (assuming a rod with spherical endcaps and water as embedding medium). As shown in Fig. 2.6 the resonance wavelength shifts to higher wavelengths for increasing aspect ratios AR. This shift can be explained by the analogy to traditional microwave and radio antennas, having their response when the length of the antenna L is half the wavelength λ_{res}. However, in the case of nanoparticles this relationship between λ_{res} and the length of the particle L is not fulfilled, which can be explained that the dimensions of the nanoparticles becomes comparable with the skin depth of the metal (Novotny 2007; Bryant et al. 2008). Simulations within the quasi-static approximation do not allow to investigate particles with different diameters, since any size-effects are neglected within this theory. For this reason I simulated rods with different diameters, showing that the resonance wavelength of thicker particles is shifted to larger wavelengths (if compared at same aspect ratios), due to retardation effects. The spectra were simulated using BEM assuming gold rods (dielectric functions given by Johnson and Christy (1972)) with spherical endcaps embedded in aqueous solution ($n = 1.33$). I provide here fit-functions for different particle diameters d:

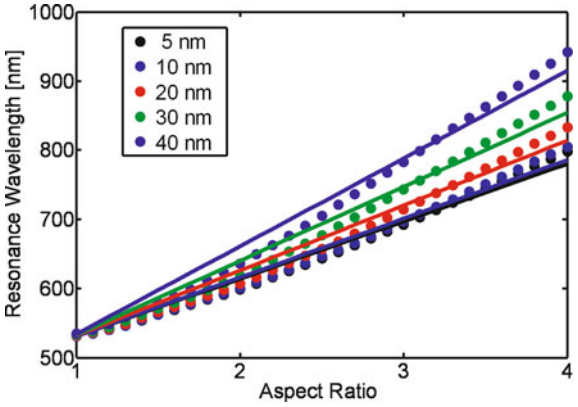

Fig. 2.6 Resonance dependency on aspect ratio for gold nanorods with different diameters. Spectra are simulated using the boundary element method assuming rods with spherical endcaps and water as embedding medium ($n = 1.33$). The fit functions for the rods with different diameters are given in Eqs. 2.46–2.50

$$\lambda_{\text{res}}(d = 5\ \text{nm})[\text{nm}] = 83 \cdot (\text{AR} - 1)[\text{nm}] + 531\ [\text{nm}] \tag{2.46}$$
$$\lambda_{\text{res}}(d = 10\ \text{nm})[\text{nm}] = 85 \cdot (\text{AR} - 1)[\text{nm}] + 531\ [\text{nm}] \tag{2.47}$$
$$\lambda_{\text{res}}(d = 20\ \text{nm})[\text{nm}] = 94 \cdot (\text{AR} - 1)[\text{nm}] + 532\ [\text{nm}] \tag{2.48}$$
$$\lambda_{\text{res}}(d = 30\ \text{nm})[\text{nm}] = 107 \cdot (\text{AR} - 1)[\text{nm}] + 533\ [\text{nm}] \tag{2.49}$$
$$\lambda_{\text{res}}(d = 40\ \text{nm})[\text{nm}] = 127 \cdot (\text{AR} - 1)[\text{nm}] + 534\ [\text{nm}] \tag{2.50}$$

It was chosen to use $(\text{AR} - 1)$ as variable, since an aspect ratio AR smaller then 1 has no meaning. As it can be seen in Fig. 2.6 the fit is valid in the range $1 \leq \text{AR} \leq 4$.

2.5.2 Resonance Dependency on Material

To find the plasmonic particles with the smallest spectral linewidth, I simulated the scattering spectra in aqueous solution of nanoparticles consisting of different materials. The dielectric functions where available for:
silver (Ag), aluminium (Al), gold (Au), cadmium (Cd), cadmium-sulfide (CdS), cadmium-selenide (CdSe), cadmium-telluride (CdTe), copper (Cu), cobalt (Co), iron(III)-oxide (Fe_2O_3), magnetite (Fe_3O_4), germanium (Ge), iridium (Ir), potassium (K), sodium (Na), lead (Pb), lead-selenide (PbSe), palladium (Pd), platinum (Pt), titanium (Ti), silicon (Si), silica (SiO_2), and zinc-sulfide (ZnS).

The simulations shows only for 5 of these materials plasmon peaks in the visible range of light (approximately between 350 nm ($\hat{=}$ 3.5 eV) and 800 nm ($\hat{=}$ 1.5 eV)): gold, silver, copper, sodium and aluminum. Figure 2.7a shows the resonance of the

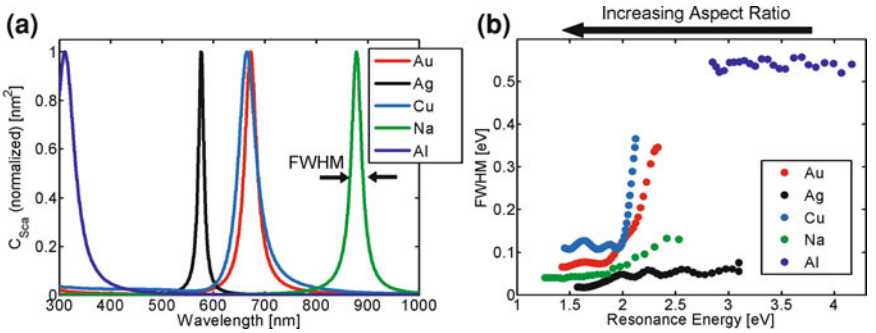

Fig. 2.7 **a** To obtain the "best" (smallest possible spectral linewidth) plasmonic particles, the scattering spectra in aqueous solution of nanoparticles consisting of different materials were simulated. From an array of dielectric functions only 5 materials show a plasmon peak in the visible spectrum: gold (Au), silver (Ag), copper (Cu), sodium (Na), and aluminum (Al). The graph shows the normalized scattering spectra of the long axis of spheroidal prolates with an aspect ratio of AR = 3 calculated within the quasi-static approximation. **b** The quality of a plasmon peak can be determined by the FWHM of the peak. Better than gold are silver and sodium ellipsoidal prolates. However, due to its violent reactivity with water, sodium is not practicable for usage. Since silver is not as inert as gold (e.g. oxygen, ions, light) gold nanoparticles are the most appropriate plasmonic particles in the visible range of light. For higher energies probably aluminum particles could be a candidate for applications, but synthesis methods for rodshaped nanoparticles are still missing

long axis for a particle with an aspect ratio of AR = 3 calculated within the quasi-static approximation for spheroidal prolates (Eq. 2.22).

The "quality" of a spectrum is often described by the linewidth of the spectrum (e.g. full width at half maximum, FWHM). Therefore I calculated the FWHM of the spectra for different aspect ratios ($1.1 < AR < 5$) and plotted this value versus its corresponding resonance energy (Fig. 2.7b). Since the dielectric function for sodium was only available from 1.24 eV, the highest calculated aspect ratio for this element was AR = 3.4. For aluminum only aspect ratios larger than AR = 2.7 could be calculated, because its dielectric function was only available up to 4.1 eV. The performed calculation reveals the best plasmonic properties for silver particles followed by sodium and gold particles. However, since sodium is violently reactive with water, it is not practicable to synthesize such nanoparticles and use them as sensors at all. Furthermore, the synthesis of silver nanorods or nanospheroids was not very successful until now, in most cases the yield of rods in such samples was far to low (less than 20 %), making these samples inapplicable for practical use. Therefore gold nano-rods/ellipsoidal prolates are the "best" plasmonic particles to use so far and are investigated more in detail in the following chapters.

The highest achievable plasmonic resonance energies for gold and silver nanoparticles are 2.3 and 3.3 eV respectively, if the particles are spherically shaped. To achieve even higher energies, aluminum nanoparticles should be chosen. Their energy range was calculated up to 4.2 eV for spheroids with an aspect ratio of AR = 2.7. Higher energies could probably be achieved by smaller aspect ratios, but the correspond-

ing spectra could not be calculated due to lacking dielectric functions. Although aluminium nanoparticles are interesting candidates for high resonance energies ($E > 3\,\text{eV}$), applications couldn't be performed yet, since synthesis methods for aluminium nanorods are still missing.

2.5.3 Resonance Dependency on Embedding Refractive Index

The dependency of the plasmon resonance on the refractive index n of the embedding medium can be understood by having a closer look on the polarizability of a spherical particle (Eq. 2.17):

$$\alpha = 3\epsilon_0 V \frac{\epsilon_r - 1}{\epsilon_r + 2}$$

where ϵ_r is the relative refractive index (Eq. 2.16): a fraction of the dielectric function of the particle material ϵ_p divided through the dielectric function of the surrounding medium ϵ_m (with: $\epsilon_m = n^2$). A resonance is occurring, if the denominator of the given equation is approaching zero (i.e. $\epsilon_\text{r} = -2$). As explained, ϵ_r is directly connected to the refractive index n and therefore it is obvious that also the resonance position depends on this property.

To calculate the resonance position of gold nanorods with spherical endcaps in dependency of the refractive index of the embedding medium, the boundary element method (BEM, Sect. 2.4.2) was used. The resonance can either be given in wavelength λ_res (nanometer [nm]) or in energy units E_res (electronvolt [eV]). The conversion can be performed by:

$$E_\text{res}[\text{J}] = h \cdot \nu = h \cdot \frac{c}{\lambda_\text{res}} \iff E_\text{res}[\text{eV}] = \frac{h \cdot c}{e} \cdot \frac{1}{\lambda_\text{res}} = \frac{1240[\text{eV} \cdot \text{nm}]}{\lambda_\text{res}\,[\text{nm}]} \quad (2.51)$$

ν: frequency of photon
$h = 6.626 \cdot 10^{-34}\,\text{Js}$: Planck constant
$c = 3 \cdot 10^8\,\text{m/s}$: speed of light
$e = 1.602 \cdot 10^{-19}\,\text{J/eV}$: conversion of Joule to Electronvolt

In Fig. 2.8 the calculated resonance wavelengths and energies are shown for gold nanorods of different aspect ratios (diameter 20 nm) with respect to the refractive index (for $1.33 < n < 3.0$). The well known nearly linear dependency (Link et al. 1999; Perez-Juste et al. 2005) can be seen and results in in the following fit functions for the resonance wavelengths and appropriate energies:

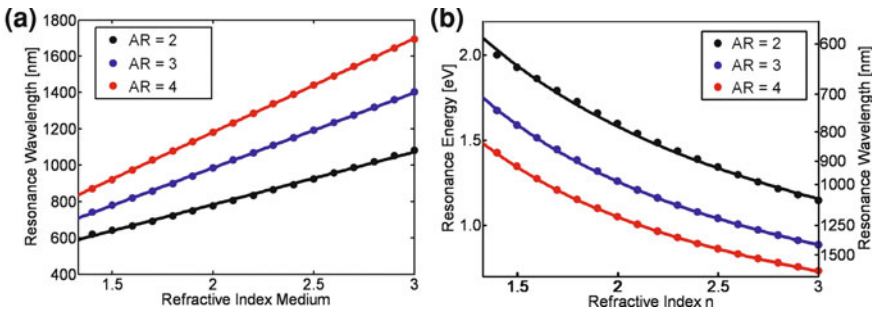

Fig. 2.8 The dependency of the (scattering) resonance-wavelength (**a**) and -energy (**b**) on the refractive index of the environmental solution is shown for rods with different aspect ratios. The calculation was performed using the boundary element method (BEM), assuming gold nanorods having a diameter of 20 nm and spherical shaped endcaps. Obtained resonances were fitted by the functions given in Eqs. 2.52–2.54

$$\lambda_{\text{res}}^{\text{AR}=2}[\text{nm}] = 495 + 289 \cdot (n-1) \iff E_{\text{res}}^{\text{AR}=2}[\text{eV}] = \frac{1240}{495 + 289 \cdot (n-1)} \tag{2.52}$$

$$\lambda_{\text{res}}^{\text{AR}=3}[\text{nm}] = 572 + 414 \cdot (n-1) \iff E_{\text{res}}^{\text{AR}=3}[\text{eV}] = \frac{1240}{572 + 414 \cdot (n-1)} \tag{2.53}$$

$$\lambda_{\text{res}}^{\text{AR}=4}[\text{nm}] = 666 + 516 \cdot (n-1) \iff E_{\text{res}}^{\text{AR}=4}[\text{eV}] = \frac{1240}{666 + 516 \cdot (n-1)} \tag{2.54}$$

It was chosen to use $(n-1)$ as variable, since a refractive index n smaller then 1 makes no physical sense.

General Fit Depended on Aspect Ratio and Embedding Medium

The steepness of the lines in Eqs. 2.52–2.54 represents the linear sensitivity (named S_λ [nm/RIU]) of the different nanorods on changes in the refractive index of the embedding medium for a given aspect ratio. Furthermore it was shown that the resonance wavelength depends also linearly on the aspect ratio for a given refractive index (Eq. 2.48). The combination of these two attributes into one formula is given in the following.

For this reason the S_λ [nm/RIU] values for different aspect ratios are calculated (Fig. 2.9) and fitted by a linear function, which is shown in the inset of the associated figure. From this result a general fit-function with respect to the aspect ratio AR of the particle *and* the refractive index n can be given:

$$\lambda_{\text{res}}[\text{nm}] = (137 \cdot \text{AR} - 14)[\text{nm/RIU}] \cdot n - (88 \cdot \text{AR} - 457)[\text{nm}] \tag{2.55}$$

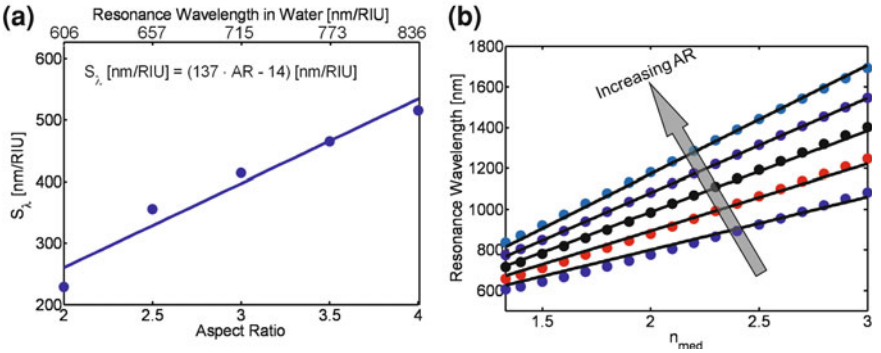

Fig. 2.9 **a** The steepness of the lines in Eqs. 2.52–2.54 represents the sensitivity S_λ [nm/RIU]", which can be fitted with respect to the aspect ratio by the shown equation. This function can be extended to a fit-function describing the resonance in dependency to the aspect ratio and the refractive index of the embedding medium (Eq. 2.55). **b** The resonances calculated with BEM are shown as *dots* and the values obtained by the presented fit-function (Eq. 2.55) are plotted as *black lines*

fulfilling the requirements of linear dependencies of the resonance wavelength on the aspect ratio AR (Eq. 2.48) and the embedding medium n (Eqs. 2.52–2.54).

The given fit-function is valid for rods with a constant diameter of 20 nm and the refractive index range of the embedding medium: $1.33 \leq n \leq 3$ (Fig. 2.9b). While for small aspect ratios AR $= 2$ the error can be up to 4.5 %, for larger aspect ratios ($2 \leq$ AR ≤ 4) the error is less then 3 %. Inserting $n = 1.33$ in this function recovers Eq. 2.48 entirely. A similar fit function was already given in Ref. Link et al. (2005):

$$\lambda_{\text{res}}[\text{nm}] = (53.71 \cdot \text{AR} - 42.29) \cdot \sqrt{n}\,[\text{nm}] + 495.14[\text{nm}] \tag{2.56}$$

however this fit was performed on spectra calculated within the quasi-static-approximation and therefore retardation and skin-depth effects were neglected.

2.5.4 Resonance Dependency on Water Temperature

In many sensing applications based on plasmonic nanoparticles, the dependency of the resonance wavelength on the refractive index of the environment is used (Chap. 8). Most of the time the nanoparticles are embedded in aqueous solution and an attachment of molecules with a higher refractive index onto the particles' surface is monitored. However, since the refractive index of water depends on its temperature, the particle's resonance wavelength is also influenced by temperature changes. To get an impression on the size of the wavelength variations, I simulated the scattering resonances of a gold nanorod with 20 nm in diameter and an aspect ratio of AR = 3 using the BEM. Thereby, the refractive index of the embedding water depends on

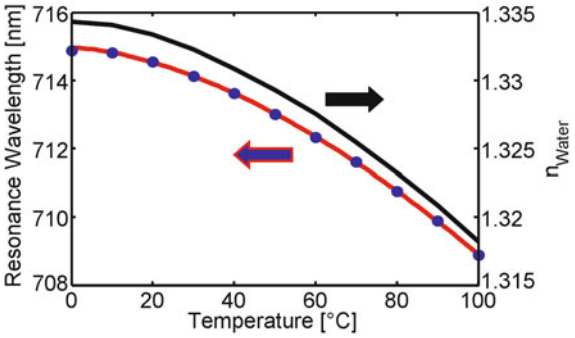

Fig. 2.10 Since the refractive index of water depends on its temperature (*right axis*), the plasmon resonance wavelength changes upon temperature variations of the aqueous solution. On the *left axis* the plasmon resonance wavelength calculated with the BEM of a gold nanorod with a diameter of 20 nm and an aspect ratio of AR = 3 is plotted. The *red line* is a fit according to Eq. 2.57

the temperature as tabulated (Mitra et al. 1972). The resulting resonance positions of this gold nanorod in dependency of the water temperature T [°C] are shown in Fig. 2.10 and can be fitted by following equation:

$$\lambda_{\text{res}}(\text{T})[\text{nm}] = 715[\text{nm}] - 0.00309 \cdot T^{1.646}\,[\text{nm}/^{\circ}\text{C}] \tag{2.57}$$

Hence, in the case the temperature of the aqueous solution for example increases from 20 to 40 °C the resonance wavelength is reduced by approximately 1 nm. This effect reduces the resolution of this sensing approach, since the water temperature is probably influenced for example by the illumination of the microscope's light source. For this reason the water temperature has probably to be controlled actively to achieve a higher resolution of the sensor approach.

2.5.5 *Influence of a Substrate*

For single particle investigation in a microscope the nanoparticles are immobilized on a substrate (Fig. 2.11). Since the substrate usually has a different refractive index n_S compared to the environmental solution n_m, it is useful to calculate the influence of the substrate. For this purpose an effective refractive index n_{eff} is assumed, which is a composition of both refractive indices:

$$n_{\text{eff}} = x \cdot n_S + (1 - x) \cdot n_m \tag{2.58}$$

x: ratio of influence to n_{eff} of the substrate

To estimate the influence of the substrate, initially the sensitivity on changes of the refractive index of the environment has to be calculated. Therefore the resonance

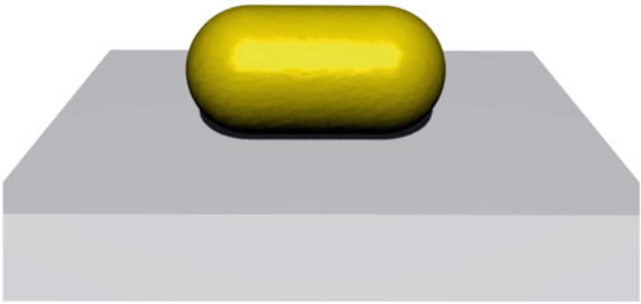

Fig. 2.11 Scheme of a gold nanorod on a substrate. Usually the substrate has a different refractive index n_S compared to the environment n_m and therefore an effective refractive index n_{eff} is assumed, which is a composition of these two refractive indices

wavelength of a gold rod in n_1 (λ_1) and in n_2 (λ_2) was calculated using DDA simulations, which where performed with the help of Olaf Schubert. The sensitivity S_λ on changes per refractive index unit (RIU) is then calculated via:

$$S_\lambda[\text{nm/RIU}] = \frac{\lambda_2 - \lambda_1}{n_2 - n_1} \tag{2.59}$$

By simulating the resonance wavelength (λ_S) of the same particle on a substrate (with n_S) in environmental solution (with n_m), the effective refractive index n_{eff} can be calculated:

$$\lambda_S - \lambda_1 = S_\lambda \cdot (n_{\text{eff}} - n_1) \tag{2.60}$$

$$n_{\text{eff}} = \frac{\lambda_S - \lambda_1}{S_\lambda} + n_1 \tag{2.61}$$

and with Eq. 2.58 the ratio of influence to n_{eff} can be calculated.

I performed simulations for rods with aspect ratios (AR = 2, 2.5, 3) on different substrates ($n_S = 1.5, 2$) and in different environmental solutions ($n_m = 1, 1.33$). The calculations revealed an influence of the substrate to the effective refractive index of:

$$x \approx 0.13 \tag{2.62}$$

The most common cases are, that the nanorods are synthesized in aqueous solution and are afterwards immobilized on a substrate (e.g. glass with $n_S = 1.5$ or semi-conducting wafer with $n_S = 2$) and an environment of water ($n_m = 1.33$) or air ($n_m = 1.0$). For this reason I provide some equations, connecting the extinction resonance wavelength λ_W in water with the scattering resonance wavelength on a substrate λ_S (Fig. 2.12):

Substrate	Environment	Fit-function (nm)
$n_S = 1.5$	$n_m = 1.0$	$\lambda_S = 0.581 \cdot \lambda_W + 212$
$n_S = 1.5$	$n_m = 1.33$	$\lambda_S = 1.025 \cdot \lambda_W - 10$
$n_S = 2.0$	$n_m = 1.0$	$\lambda_S = 0.631 \cdot \lambda_W + 200$
$n_S = 2.0$	$n_m = 1.33$	$\lambda_S = 1.101 \cdot \lambda_W - 38$

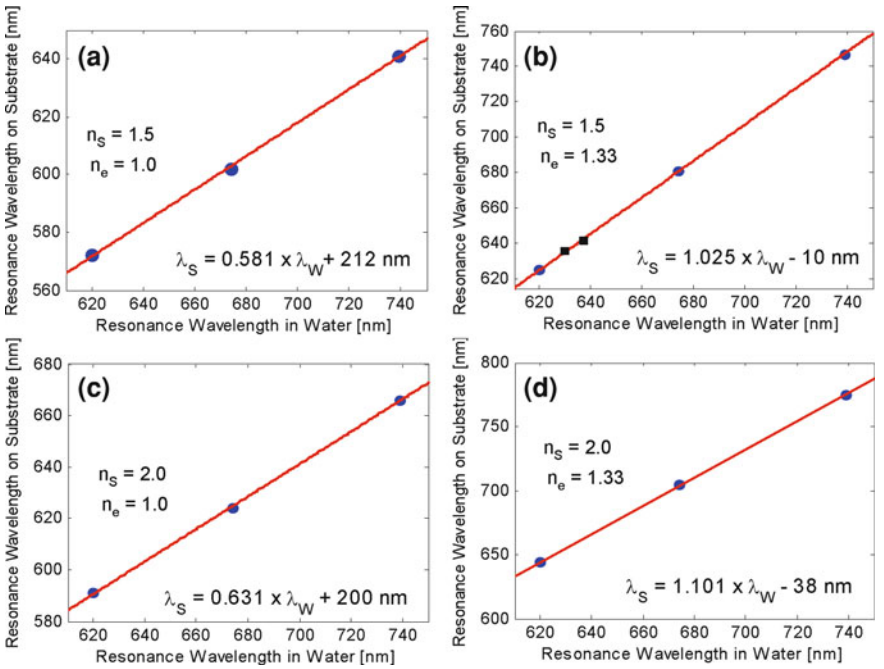

Fig. 2.12 The resonance wavelength of gold nanorods is simulated with DDA in aqueous solution and on a different substrates (n_S) and environments (n_m). If the resonance on a specific substrate and environment λ_S is plotted versus the resonance wavelength in water λ_W, the data points of particles with different aspect ratios (AR = 2, 2.5, 3, *blue dots*) can be fitted by a linear function. The *black dots* in **b** indicate two measured samples, where the resonance wavelength in water of the ensemble was measured as well as the mean resonance wavelength on a glass substrate ($n_S = 1.5$) of many single particles with water ($n_m = 1.33$) as environment. The measured data fit nicely to the simulated results

With these fit-functions it is possible to estimate the scattering resonance wavelength on a specific substrate and environment, if the extinction resonance wavelength in aqueous solution is known.

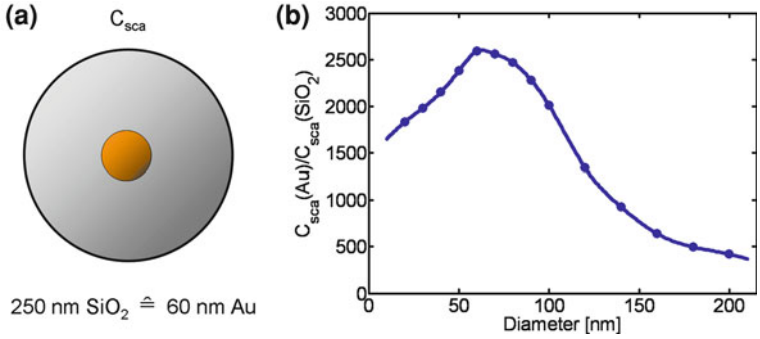

Fig. 2.13 **a** A gold (Au) sphere with 60 nm in diameter embedded in water scatters as much light as a 250 nm sized silica (SiO_2) sphere, compared at the resonance wavelength of the gold sphere ($\lambda_{res} = 548$ nm). **b** Comparing the scattering cross-sections of a Au and a SiO_2 sphere in respect to the particle size reveals a maximum at approximately 60 nm with an approximately 2,500 higher scattering efficiency for the Au sphere

2.5.6 Comparison of Scattering Cross-Sections

To get an impression about the scattering efficiency of gold nanoparticles, a comparison with silica (SiO_2) nanoparticles is useful. For example a gold sphere with 60 nm in diameter embedded in water has according to Mie's theory a scattering cross-section of $C_{sca} = 3130\,nm^2$ at its resonance wavelength of 548 nm. A silica sphere, which should scatter at the same wavelength the equivalent amount of light, has to be 250 nm in diameter (Fig. 2.13a). This means the volume of the silica sphere is enlarged by a factor of 72 compared to the gold sphere, to achieve the same amount of scattering. Since silica spheres do not have a resonance peak like gold spheres, it make sense to compare the values at the resonance wavelength of the gold sphere.

To compare in general the scattering properties of gold spheres with silica spheres, I calculated their scattering cross-sections in aqueous solution for different diameters according to Mie's theory. Therefore, I determined the scattering cross-section of the gold sphere $C_{sca}(Au)$ at its plasmon resonance and compared it with the scattering cross-section of the silica sphere $C_{sca}(SiO_2)$ of the same size at the same wavelength. Figure 2.13b shows that the efficiency depends on the size of the particles and for an approximately 60 nm gold sphere in diameter a maximum is reached. At this size the scattering efficiency of the gold sphere is about 2,500 higher compared to a SiO_2 sphere of the same size. To understand where the maximum is coming from, I performed the same calculation using Rayleigh's quasi-static approximation (Eq. 2.17) instead of Mie's theory. Since this equation is totally independent from the size of the particle, the ratio of the scattering cross-sections of gold and SiO_2 spheres is constant for all sphere sizes. However, using Eq. 2.41 instead, having size dependend terms to describe the retardation effects and radiative losses, helps to understand the observed maximum. In the case the radiative losses are neglected by setting the third term in the denominator to zero, the ratio $C_{sca}(Au)/C_{sca}(SiO_2)$ increases if

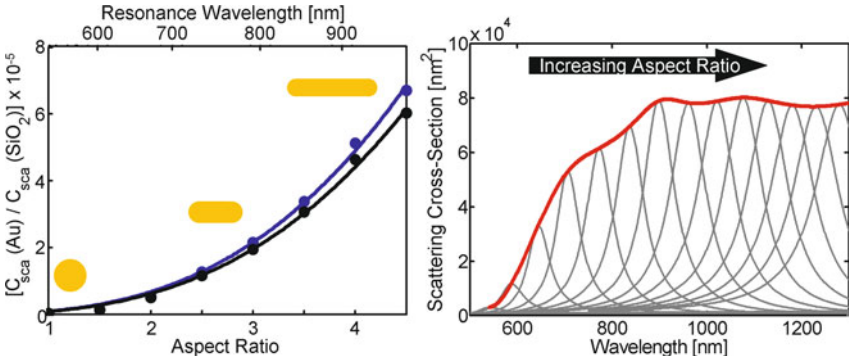

Fig. 2.14 **a** Comparisons of the scattering cross-section of gold nanorods $C_{sca}(Au)$ with a silica sphere (*blue*) or silica rods (*black*) $C_{sca}(SiO_2)$ at the resonance of the rod in water. The volume of the particles was kept constant (i.e. equal to a sphere with 60 nm diameter) by choosing the appropriate rods' length and width to allow a direct comparison. The ratio of the cross-sections compared to the silica sphere and the silica rods in respect to the aspect ratio can be fitted by Eqs. 2.63 and 2.64, respectively. **b** Scattering spectra of the gold nanorods with constant volume, but different aspect ratios. The amount of scattered light increases up to an aspect ratio of AR ≈ 4 due the associated resonance shift to larger wavelengths, where the interband damping gets less. For even higher aspect ratios, the interband damping is not existing at all and therefore the scattering cross-sections are more or less constant

the particle sizes are enlarged. However, if the radiative losses are considered, but the retardation effects are neglected by setting the second term in the denominator to zero, the examined ratio is decreasing for larger spheres. For this reason, two contrary effects are present and are therefore leading to a maximum in the ratio of $C_{sca}(Au)/C_{sca}(SiO_2)$ in respect of the sphere sizes, since the radiative losses are more pronounced for larger sizes due to the third power dependency on the size parameter θ.

Comparison with Rodshaped Particles

Since in this work mainly rodshaped gold nanoparticles are investigated, it is helpful to compare the scattering cross-sections of these particles with the one of a SiO_2 nanosphere, both embedded in water. To allow a direct comparison, the volume of the gold nanorods has to be the same (e.g. equal to the volume of a sphere with 60 nm in diameter) and the aspect ratio is varied by choosing the appropriate length a and width b of the rod. Calculations of the scattering cross-sections are performed using BEM simulations, and the comparison takes place at the resonance wavelength of the long axis of each gold rod. The ratio $C_{sca}(Au)/C_{sca}(SiO_2)$ in respect to the aspect ratio AR of the gold nanorod ($1 \leq AR \leq 4.5$) can be fitted by the following function (Fig. 2.14a, blue line):

$$C_{sca}(Au)/C_{sca}(SiO_2)(\text{spheres}) = 9293 \cdot AR^{2.86} \tag{2.63}$$

Comparing the scattering cross-section of gold nanorods with SiO_2 nanorods of the same dimension reveals a similar ratio as the initial one and can be approximated by the equation (Fig. 2.14a, black line):

$$C_{\text{sca}}(\text{Au})/C_{\text{sca}}(\text{SiO}_2)(\text{rod}) = 8721 \cdot \text{AR}^{2.83} \tag{2.64}$$

The similarity between SiO_2 ($n = 1.5$) spheres and rods of the same volume in aqueous solution ($n = 1.33$) can be explained by Eq. 2.22. The denominator is given by $1 + L(\epsilon_r - 1)$, where $\epsilon_r - 1 = 1.5^2/1.33^2 - 1 = 0.27$. Since the geometrical factor L is in the range $0 \leq L \leq 0.33$ (Eq. 2.24) the denominator D can maximal decrease from $D = 1 + 0.27 \cdot 0.33 = 1.09$ to $D = 1$. Since the volume of the SiO_2 particles is kept constant, the scattering cross-section varies maximal 9 % due to changes in the SiO_2 particle shape.

Looking on the scattering spectra of gold nanorods, it can be seen that the maximal amount of scattered light increases up to rods having an aspect ratio of approximately 4 (Fig. 2.14b). For further enlarged particles the amount of scattered light is more or less constant. The increase can be explained by the resonance shift of the rods to higher wavelengths (i.e. lower energies), where the interband damping becomes less. For all higher resonance wavelengths (particles with aspect ratio >4) the interband damping is even diminished entirely, and therefore the amount of scattered light is constant.

To explain the observed increase in the ratio of scattered light for gold nanorods compared to silica spheres (Fig. 2.14) for rods with an aspect ratio larger than 4, the scattering cross-sections of a silica sphere in respect of the wavelength has to be considered (Fig. 2.15). It can be seen, that for higher wavelengths the scattering cross-section of a silica sphere is reduced due to Rayleigh's law ($C_{\text{sca}} \propto 1/\lambda^4$) (Rayleigh 1899). This leads to the mentioned increase in the scattering ratio, although the amount of scattered light of the rods is constant in this wavelength region.

Indeed, in general particles with higher aspect ratio (i.e. higher resonance wavelength) are more adequate for practical applications, if a laser with the appropriate wavelength of the rods' resonance is used for illumination. Since dielectric particles in the sample (e.g. dirt) are usually producing an undesired background, their smaller scattering cross-section for higher wavelengths is leading to an increase in the image contrast (i.e. signal to noise ratio).

2.5.7 *Resonance Dependency on Interparticle Distance of Spheres*

If two or more plasmonic nanoparticles are getting close together, the resonance wavelength of each of the particles is influenced. Due to the presence of neighboring particles, the electric field E' felt by each particle is the sum of the incident light-field E and the near-field of the electric dipole of the neighboring particles.

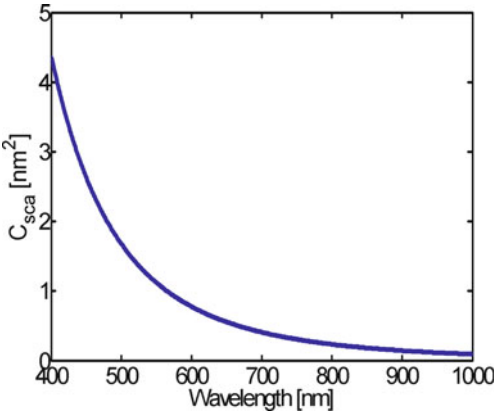

Fig. 2.15 The scattering cross-section of a silica sphere with 60 nm in diameter in aqueous solution follows Rayleigh's law and decreases for larger wavelengths. Therefore, the scattering ratio between gold nanorods and SiO_2 spheres increases continuously, although the maximal scattering cross-section is constant for aspect ratios of the gold nanorods larger then 4 (Fig. 2.14a and b)

This effect (also named *plasmon coupling*) leads to an increase of the resonance wavelength compared to an isolated particle. Since for single particle spectroscopy gold spheres with a diameter of 40 or 60 nm are commonly the most used particles, I simulated the resonance wavelengths of dimers consisting of two equally sized spheres with different interparticle distances (Fig. 2.16). For the simulation the boundary element method was used, and the embedding material was chosen to be water with a refractive index of $n = 1.33$. The obtained resonance wavelengths of the longitudinal axis (i.e. the interparticle axis) can be fitted for 40 and 60 nm in diameter spheres in respect of the interparticle distance d by following equations in the range $3[\text{nm}] < d < 50[\text{nm}]$, respectively:

$$\lambda_{\text{res}}(40\ \text{nm})[\text{nm}] = 538.7\ [\text{nm}] \cdot \left[1 - \exp\left(\frac{-d\ [\text{nm}]}{8.7\ [\text{nm}]}\right)\right]^{-0.067} \tag{2.65}$$

$$\lambda_{\text{res}}(60\ \text{nm})[\text{nm}] = 552.7\ [\text{nm}] \cdot \left[1 - \exp\left(\frac{-d\ [\text{nm}]}{15.2\ [\text{nm}]}\right)\right]^{-0.067} \tag{2.66}$$

These functions are only provided for empirical estimations to simplify the transformation between interparticle distance and resonance wavelength.In general, the electric field felt by each particle is the sum of the incdent light field and the near-field of the dielectric dipole of the neighboring particle, which is known to decay as the cube of the inverse particle distance (Jain et al. 2007). Due to this sum, the resonance wavelength of a dimer cannot be fitted by a function which is simply proportional to the cube of the inverse particle distance. For this reason, in literature (Reinhard et al. 2005; Jain and El-Sayed 2008) the resulting resonance wavelength

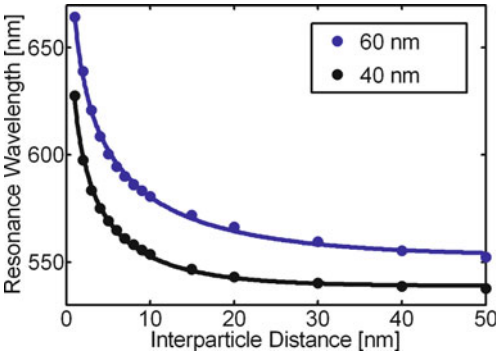

Fig. 2.16 For a dimer, the resonance wavelength of the longitudinal axis depends on the interparticle distance. Here, the dependency is plotted for dimers consisting of 40 and 60 nm spheres in diameter simulated using the boundary element method (*dots*). Appropriate fit functions (*solid lines*) are given in Eqs. 2.65 and 2.66 for both sizes

of a dimer in dependency of the interparticle distance d is often approximated by a simple exponential decay-function ($\lambda_{\text{res}} = y_0 + a \cdot \exp(-d/b)$). Both, this type of function as well as my provided ones, are approximations with the same number of parameter (i.e 3), but the latter ones fit the data points better. Therefore these stretched exponential equations are used in further calculations (Chap. 11).

2.5.8 Optical Response of a Dimer

Since the optical response of a nanoparticle depends on its volume (Eq. 2.18), a dimer consisting of two spherical particles should scatter and adsorb more light compared to a single sphere of the same diameter. The extinction is in a first approximation direct proportional to the particle volume and therefore someone could assume that the extinction of a dimer is twice as large as in the case of a single sphere. But the plasmon coupling leads to an increase of the longitudinal resonance wavelength and therefore the interband-absorption is reduced (Sönnichsen et al. 2002). Hence, the extinction for a dimer is even larger then the factor of 2 and approaches only in the limit of a large interparticle distance (e.g. no plasmon coupling) the value of 2. In the case of the scattering, this effect is also present, however additionally the fact that the scattering cross-section depends on the square of the volume has to be considered. Nevertheless, again the scattering is twice as much for the dimer compared to a single sphere in the limit of a large interparticle distance, where both particles can be considered as two single ones. In Fig. 2.17 the ratio of the optical responses F of a dimer versus a single sphere are plotted for the extinction as well as for the scattering in respect to different interparticle distances, where F_{ext} and F_{sca} are defined as:

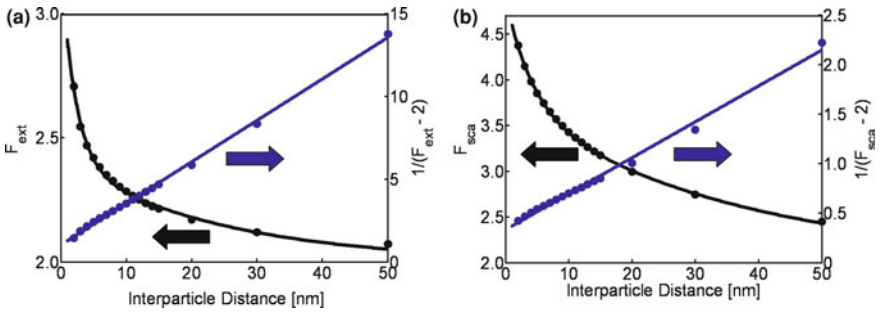

Fig. 2.17 The optical response of a dimer depends on the interparticle distance for the extinction **a** as well as for the amount of scattered light **b**. In the limit of a large interparticle distance the optical response of a dimer consisting of two spherical particles is twice as much compared to a single sphere of the same diameter. The figures show the ratio F of the optical response of a dimer compared to a single sphere. Calculations are based on BEM simulations with gold spheres with 60 nm in diameter in water. The fit functions of the factor F (Eq. 2.67) and $1/(F-2)$ are given in Eqs. 2.68–2.70

$$F_{\text{ext}} = \frac{\int_{400}^{1000} C_{\text{ext}}(\text{Dimer})d\lambda}{\int_{400}^{1000} C_{\text{ext}}(\text{Single sphere})d\lambda} \quad F_{\text{sca}} = \frac{\int_{400}^{1000} C_{\text{sca}}(\text{Dimer})d\lambda}{\int_{400}^{1000} C_{\text{sca}}(\text{Single sphere})d\lambda} \tag{2.67}$$

The factor F can then be fitted with a double exponential function, which follows the requirement of approaching the value 2 for large interparticle distances d ($3\,\text{nm} \leq d \leq 50\,\text{nm}$):

$$F_{\text{ext}} = 2 + 0.788 \cdot \exp\left(\frac{-d}{2.18}\right) + 0.412 \cdot \exp\left(\frac{-d}{24.21}\right) \tag{2.68}$$

$$F_{\text{sca}} = 2 + 1.153 \cdot \exp\left(\frac{-d}{4.16}\right) + 1.741 \cdot \exp\left(\frac{-d}{36.01}\right) \tag{2.69}$$

For reasons of simplification, the fraction $\frac{1}{F-2}$ was plotted, which then could be fitted with linear functions ($3\,\text{nm} \leq d \leq 50\,\text{nm}$) :

$$\frac{1}{F_{\text{ext}} - 2} = 1.02 + 0.251 \cdot d, \quad \frac{1}{F_{\text{sca}} - 2} = 0.336 + 0.036 \cdot d; \tag{2.70}$$

However, in single particle measurements it is often interesting to compare the amount of scattered light at each resonance wavelength instead of the integrated spectrum (Fig. 2.18a):

$$f_{\text{sca}} = \frac{C_{\text{sca}} \text{ of dimer at its resonance}}{C_{\text{sca}} \text{ of single sphere at its resonance}} = \frac{\text{C}_\text{D}}{\text{C}_\text{M}} \tag{2.71}$$

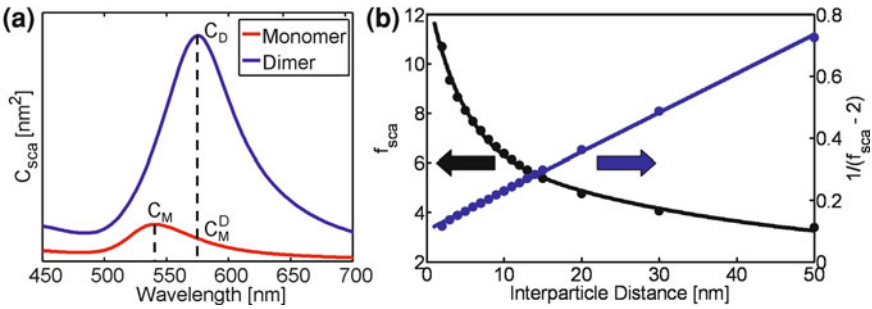

Fig. 2.18 **a** For single particle measurements it is often interesting to compare the ratio of the scattering cross-sections of the longitudinal mode of a dimer with the one of a single particle. The scattering cross-sections of a single nanosphere (*red line*) and a dimer (*purple line*) can be compared at each maximum (C_M and C_D, respectively), or at a specific resonance wavelength (e.g. maximal scattering cross-section of the dimer) with the cross-sections C_M^D for the monomer and C_D for the dimer. **b** Ratio of the maximal scattering cross-sections of the monomer (C_M) and the dimer (C_D). The fit functions of the factor f_{sca} (Eq. 2.71) and $1/(f_{\text{sca}} - 2)$ shown are given in Eqs. 2.72 and 2.73, respectively. The calculations are based on BEM simulations with gold spheres with 60 nm in diameter in aqueous solution

For this purpose only the scattering of the longitudinal axis is considered since in single particle measurements often a polarizer is used to separate the longitudinal mode from the transversal one. The factor f_{sca} can then be fitted in respect of the interparticle distance d ($3\,\text{nm} \leq d \leq 50\,\text{nm}$) by the following equations (Fig. 2.18b):

$$f_{\text{sca}} = 2 + 6.21 \cdot \exp\left(\frac{-d}{4.28}\right) + 4.84 \cdot \exp\left(\frac{-d}{36.98}\right) \tag{2.72}$$

$$\frac{1}{f_{\text{sca}} - 2} = 0.102 + 0.0127 \cdot d; \tag{2.73}$$

Instead of comparing the scattering cross-sections of a monomer and a dimer at each resonance, in single particles measurements the scattering cross-section of both structures could also be compared at one specific wavelength (e.g. the resonance wavelength of the dimer, Fig. 2.18a):

$$\overline{f_{\text{sca}}} = \frac{C_{\text{sca}} \text{ of dimer at its resonance}}{C_{\text{sca}} \text{ of single sphere at dimers resonance}} = \frac{\text{C}_\text{D}}{\text{C}_\text{M}^\text{D}} \tag{2.74}$$

Again, only the the scattering cross-section of the dimer's longitudinal plasmon mode is considered and the factor $\overline{f_{\text{sca}}}$ can be fitted in respect of the interparticle distance d ($3\,\text{nm} \leq d \leq 50\,\text{nm}$) according to (Fig. 2.19):

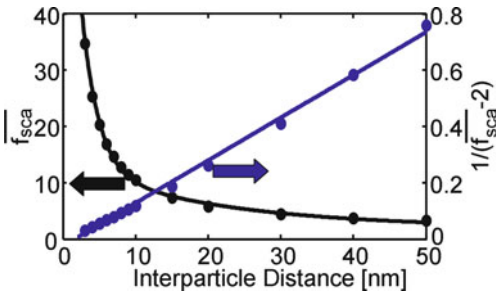

Fig. 2.19 Comparission of the scattering cross-sections of the monomer and the dimer at the dimer's resonance (C_M^D and C_D, respectively according to Fig. 2.18a). The fit functions of the factor $\overline{f_{sca}}$ (Eq. 2.74) and $1/(\overline{f_{sca}}-2)$ shown are given in Eqs. 2.75 and 2.76, respectively. The calculations are based on BEM simulations with gold spheres with 60 nm in diameter in aqueous solution

$$\overline{f_{sca}} = 2 + 87.9 \cdot \exp\left(\frac{-d}{2.29}\right) + 11.5 \cdot \exp\left(\frac{-d}{20.14}\right) \tag{2.75}$$

$$\frac{1}{\overline{f_{sca}} - 2} = 0.024 + 0.01517 \cdot d \tag{2.76}$$

References

Bohren, C., & Huffman, D. R. (1983). *Absorption and scattering of light by small particles*. New York: Wiley-Interscience.

Bryant, G., Garcia de Abajo, F., & Aizpurua, J. (2008). Mapping the plasmon resonances of metallic nanoantennas. *Nano Letters*, *8*(2), 631–636.

Draine, B., & Flatau, P. (2004). User guide to the discrete dipole approximation code ddscat 6.1. http://arxiv.org/abs/astro-ph/0409262v2

Faraday, M. (1857). The Bakerian Lecture—on the experimental relations of gold (and other metals) to light. *Philosophical Transactions of the Royal Society of London*, *147*, 145–181.

Gans, R. (1912). über die Form ultramikroskopischer Goldteilchen. *Annalen der Physik*, *342*(5), 881–900.

Greiner, W. (1991). Theoretische Physik, Band 3: Klassische Elektrodynamik (5th ed.), p. 155. Fulda: Verlag Harri Deutsch.

Jain, P. K., & El-Sayed, M. (2008). Noble metal nanoparticle pairs: Effect of medium for enhanced nanosensing. *Nano Letters*, *8*, 4347–4352.

Jain, P. K., Huang, W. Y., & El-Sayed, M. (2007). On the universal scaling behavior of the distance decay of plasmon coupling in metal nanoparticle pairs: A plasmon ruler equation. *Nano Letters*, *7*, 2080–2088.

Johnson, P., & Christy, R. (1972). Optical constants of the noble metals. *Physical Review B*, *6*(12), 4370–4379.

Kim, Y. J., Johnson, R. C., Li, J. G., Hupp, J. T., & Schatz, G. C. (2002). Synthesis, linear extinction, and preliminary resonant hyper-rayleigh scattering studies of gold-core/silver-shell nanoparticles: Comparisons of theory and experiment. *Chemical Physics Letters*, 352(5–6), 421–428.

Kooij, E. S., & Poelsema, B. (2006). Shape and size effects in the optical properties of metallic nanorods. *Physical Chemistry Chemical Physics*, *8*(28), 3349–3357.

Kuwata, H., Tamaru, H., Esumi, K., & Miyano, K. (2003). Resonant light scattering from metal nanoparticles: Practical analysis beyond rayleigh approximation. *Applied Physics Letters*, *83*(22), 4625–4627.

Link, S., El-Sayed, M. A., & Mohamed, M. B. (2005). Simulation of the optical absorption spectra of gold nanorods as a function of their aspect ratio and the effect of the medium dielectric constant (vol 103b, pg 3073, 1999). *Journal of Physical Chemistry B*, *109*(20), 10531–10532.

Link, S., Mohamed, M. B., & El-Sayed, M. A. (1999). Simulation of the optical absorption spectra of gold nanorods as a function of their aspect ratio and the effect of the medium dielectric constant. *Journal of Physical Chemistry B*, *103*(16), 3073–3077.

Liu, M. Z., & Guyot-Sionnest, P. (2004). Synthesis and optical characterization of au/ag core/shell nanorods. *Journal of Physical Chemistry B*, *108*(19), 5882–5888.

Maxwell, J. C. (1865). A dynamical theory of the electromagnetic field. *Philosophical Transactions of the Royal Society of London*, *155*, 459–512.

Mie, G. (1908). Beiträge zur Optik trüber Medien, speziell kolloidaler Metallösungen. *Annalen der Physik*, *25*(3), 377–445.

Mitra, S., Dass, N., & Varshneya, N. (1972). Temperature dependence of refractive-index water. *Journal of Chemical Physics*, *57*, 1798–1799.

Myroshnychenko, V., Rodriguez-Fernandez, J., Pastoriza-Santos, I., Funston, A. M., Novo, C., Mulvaney, P., et al. (2008). Modelling the optical response of gold nanoparticles. *Chemical Society Reviews*, *37*(9), 1792–1805.

Nolting, W. (1997). Grundkurs Theoretische Physik, Band 3: Elektrodynamik (5th ed.), pp. 138. Braunschweig: Friedr, Vieweg und Sohn Verlagsgesellschaft.

Novotny, L. (2007). Effective wavelength scaling for optical antennas. *Physical Review Letters*, *98*(26), 266802.

Osborn, J. A. (1945). Demagnetizing factors of the general ellipsoid. *Physical Review*, *67*(11), 351–357.

Perez-Juste, J., Pastoriza-Santos, I., Liz-Marzan, L. M., & Mulvaney, P. (2005). Gold nanorods: Synthesis, characterization and applications. *Coordination Chemistry Reviews*, *249*(17–18), 1870–1901.

Prescott, S. W., & Mulvaney, P. (2006). Gold nanorod extinction spectra. *Journal of Applied Physics*, *99*(12), 123504.

Prescott, S. W., & Mulvaney, P. (2008). Gold nanorod extinction spectra. *Journal of Applied Physics*, *103*(11), 119901.

Rayleigh, L. (1899). On the transmission of light through an atmosphere containing small particles in suspension, and on the origin of the blue of the sky. *Philosophical Magazine* (Series 5), 47(287), 375–384.

Reinhard, B. M., Siu, M., Agarwal, H., Alivisatos, A. P., & Liphardt, J. (2005). Calibration of dynamic molecular rule based on plasmon coupling between gold nanoparticles. *Nano Letters*, *5*(11), 2246–2252.

Sönnichsen, C. (2001). *Plasmons in metal nanostructures*. München: Cuvillier Verlag Göttingen.

Sönnichsen, C., Franzl, T., Wilk, T., von Plessen, G., Feldmann, J., Wilson, O., et al. (2002). Drastic reduction of plasmon damping in gold nanorods. *Physical Review Letters*, *88*(7), 077402.

Strutt, J. L. R. (1871a). On the light from the sky, its polarization and colour. *Philosophical Magazine* (Series 4), 41(271), 107–120.

Strutt, J. L. R. (1871b). On the light from the sky, its polarization and colour. *Philosophical Magazine* (Series 4), 41(273), 274–279.

Strutt, J. L. R. (1871c). On the scattering of light by small particles. *Philosophical Magazine* (Series 4), 41(275), 447–454.

Chapter 3
Synthesis of Nanoparticles

In this chapter I describe the synthetic methods for the particles used in this work. Initially bare gold nanorods are synthesized (Sect. 3.1), which are used to investigate continuously the growth of bigger nanoparticles (Chap. 6) and the protein-membrane interaction on a single particle level (Chap. 7). To reduce the single particle linewidth and therefore to increase the sensitivity on changes in the refractive index (Sect. 9.2), these rods are coated with a thin silver shell (Sect. 3.2). Another method to increase the sensitivity of nanoparticles is to produce hollow rod-shaped nanorattles, which were synthesized by Yuriy Khalavka (Sect. 3.3). To investigate the polarization depend scattering spectra of different shapes with the RotPOL setup (Sect. 5.2), differently shaped silver nanoparticles like cubes, rods and triangles (Sect. 3.4) were synthesized by Luigi Carbone, Yuriy Khalavka and myself.

3.1 Gold Nanorods

The gold nanorods we use here are produced according to the seeded-growth technique of (Nikoobakht and El-Sayed 2003) in a highly concentrated aqueous surfactant solution. The seeds are prepared by adding 50 μL of 0.1 M hydrogen tetrachloroaurate(III)hydrate ($HAuCl_4$, Sigma-Aldrich) to 5.0 mL deionized water (18 MΩ), and mixed with 5.0 mL of a 0.2 M cetyltrimethylammoniumbromide solution (CTAB, Sigma-Aldrich, Batch #: 026k0185). Under vigorous shaking, 0.6 mL of ice-cold 0.01 M sodium borohydride solution ($NaBH_4$, Aldrich) are added resulting in the formation of a brownish yellow solution. The seed solution is kept at 37 °C for 2 h before use. In a second step these seeds are added to a "growth solution" containing 50 μL of 0.1 M $HAuCl_4$ diluted in 5.0 mL deionized water and mixed with 5.0 mL of 0.2 M CTAB solution. Typically, 20 μL of 0.04 M silver nitrate ($AgNO_3$, Sigma-Aldrich) and 70 μL of 0.0788 M l-ascorbic acid (Sigma) solution are added (in this order). After the final addition of 12 μL of the preformed seeds, the solution gradually develops a strong blue or brown color (depending on the final size and shape of

J. Becker, *Plasmons as Sensors*, Springer Theses,
DOI: 10.1007/978-3-642-31241-0_3, © Springer-Verlag Berlin Heidelberg 2012

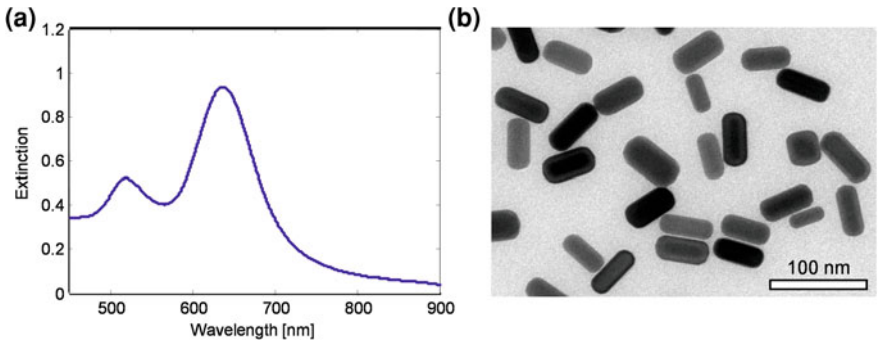

Fig. 3.1 **a** Extinction spectra and **b** Transmission electron microscope image (TEM) of a typical gold nanorod sample

the nanoparticles) within 10–20 min, indicating the formation of gold nanorods. A typical extinction spectrum (Sect. 4.1) and transmission electron microscope image (TEM, Sect. 4.3) of such synthesized nanorods is shown in Fig. 3.1.

3.2 Silver Coated Gold Nanorods

The silver coating of gold nanorods follows a procedure described recently by (Liu and Guyot-Sionnest 2004) by adding preformed gold nanorods to a coating solution containing silver ions. In contrast to Liu and Guyot-Sionnest, we first remove excessive growth solution from the gold rods, which contains additional silver and gold ions, by centrifugation and re-dispersion in 0.1 M CTAB. Thereafter 0.8 ml of the CTAB-goldrods solution is diluted in 4 ml of 1 wt% aqueous polyvinyl pyrrolidone (PVP, Aldrich). To the mixture of PVP, CTAB and gold nanoparticles, different amounts of 1 mM $AgNO_3$ (e.g. 180 µL) and 0.1 M ascorbic acid (e.g. 100 µL) are added. Raising the pH by adding 200 µL of 0.1 M sodium hydroxide (NaOH, Merck) initiates the coating reaction and leads to a color change within a few minutes. We keep the molar ratio between $AgNO_3$, ascorbic acid and NaOH constant (0.6:25:50), when the concentration of silver nitrate is changed.

Sample Characterization

Increasing the silver concentration in the coating solution leads to a strong color shift (Fig. 3.2a, c). The different electron density of silver and gold makes it possible to visualize clearly the silver shell around the original gold nanorod in TEM (Fig. 3.2b). The images confirm the expected increase of the silver shell thickness with increasing concentration of silver in the coating solution. When the silver concentration becomes too high, the shell grows inhomogeneously. High-resolution TEM and spatially resolved elemental analysis by nanospot energy dispersive X-ray spectroscopy (EDX, Sect. 4.3) confirm the monocrystallinity of the particles and the epitaxial growth of the silver shell on the gold particles (Fig. 3.2d–g). Extinction spectra of the solutions

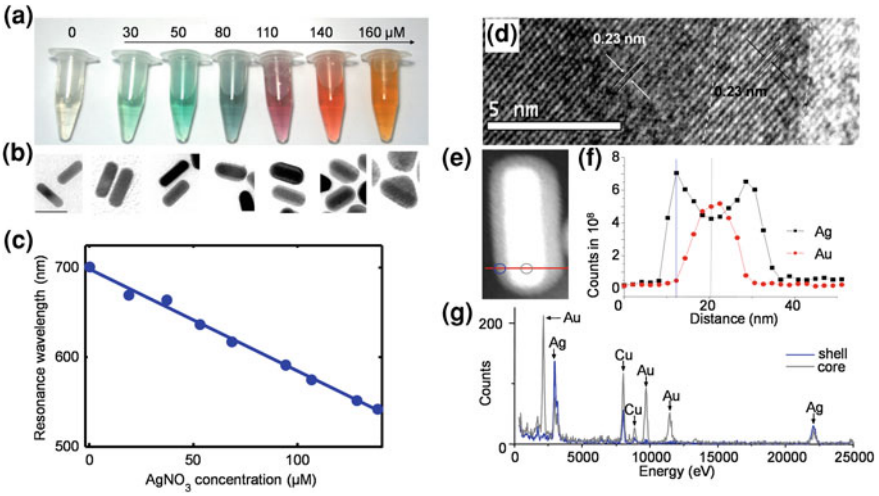

Fig. 3.2 **a** True color photograph showing the color change of the pure gold nanorods (mean dimensions 51 × 18 nm, left sample) upon increasing silver concentration in the coating solution (indicated by the number above each vial). **b** Representative TEM images corresponding to the samples shown above. Images show the increasing thickness of the silver shell with higher silver concentration. At very high silver concentrations the shell becomes inhomogeneous (scalebar for all images 50 nm). **c** Resonance wavelength as a function of silver concentration in the coating solution for a gold nanorod sample with a starting resonance wavelength of 700 nm. The shift in the resonance wavelength is approximately linearly dependent on the amount of silver present with a slope of −1.15 nm/μM (*dashed line*). **d** High-resolution TEM image of a silver-coated gold nanorod. *Dashed lines* indicate the borders of the silver shell. Equal lattice spacing (0.23 nm) in the Au core and the Ag shell confirms epitaxial growth ([111] planes). **e** Scanning TEM image of a silver-coated gold nanorod with the position of the EDX linescan (*red line*). **f** Profile of the Au and Ag elemental distributions. **g** Two representative EDX spectra (at the positions indicated in **e** and **f**) [Image reprinted with permission of the American Chemical Society (Becker et al. 2008)]

reveal a blueshift of the plasmon resonance wavelength of up to 150 nm (Fig. 3.2c), which is approximately linearly dependent on the amount of silver present (slope about −1.15 nm/μM).

3.2.1 Coating on a Substrate for Single Particle Observation

In order to observe coating of single particles with the dark-field microscope, gold nanorods are first immobilized on a glass surface via the addition of sodium chloride (NaCl, Ambion). After extensive washing with deionized water, they are immersed in 40 μL 0.01 M NaOH, which is simultaneously used as the immersion media for a water immersion objective (Zeiss, 100×, NA 1.0). Best results are obtained when detaching the drop of NaOH from the objective, mixing it with 80 μL growth solution containing PVP, $AgNO_3$ and ascorbic acid in the same ratios as mentioned above and reattaching the solution again to the objective. If the experiment is performed the other way around (first putting in the growth solution, then mixing with NaOH),

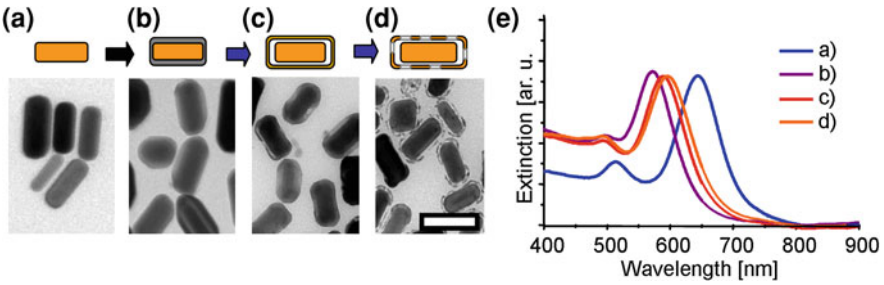

Fig. 3.3 Growth of gold nanorattles. Starting with gold nanorods (**a**), a silver layer is deposited (**b**). By means of reaction with Au ions (*blue arrows*), a shell of Ag-Au grows and then transforms into a cage with the dealloying of silver leading to a closed (**c**) or porous shell (**d**),depending on the amount of gold added. Representative TEM images corresponding to all the steps are shown on the bottom (scalebar is 50 nm). **e** Extinction spectra corresponding to each step. While the silver coating leads to a *blue*-shift of the resonance wavelength, the replacement of the silver shell with a gold cage *red*-shifts the resonance wavelength [Image reprinted with permission of the American Chemical Society (Khalavka et al. 2009)]

silver particles form all over the glass surface and completely cover the (silver coated) gold rods. All solutions are filtered through a syringe filter (0.02 μm) to prevent the introduction of dust.

3.3 Synthesis of Gold Nanorattles

Here, a strategy for the preparation of rod-shaped gold nanorattles, i.e. hollow gold nanostructures with a solid nanorod inside (Fig. 3.3) is reported. These rod-shaped gold nanorattles combine the advantages of rods (low plasmon resonance frequency, high polarizability, and small plasmon linewidth (Sonnichennsen et al. 2002)) with the high surface area of hollow structures and show improved optical sensitivity on changes in the refractive index of the environmental solution, compared to gold nanorods, spheres, and hollow spheres in the visible range of light (Sect. 9.3). In contrast to the spherical Au/Ag nanorattles reported by Xia et al. (Sun et al. 2004), our rod-shaped nanorattles consist entirely of pure gold, making them chemically stable in aqueous environments.

3.3.1 Chemical Procedure

The strategy of rod-shaped nanorattle synthesis closely follows the general procedure used by Xia et al. (Sun et al. 2004) to form spherical nanorattles with a Au–Ag core. Preformed gold nanorods (Sect. 3.1) are coated with a thin silver layer (Fig. 3.3c) via reduction with ascorbic acid (Asc):

$$2Ag^{+} + H_2Asc + 2OH^{-} \rightarrow 2Ag^{0} + 2H_2O + Asc \quad (3.1)$$

The silver layer produced by the function of silver with ascorbic acid in the presence of PVP grows epitaxially on the CTAB-coated gold nanorod surface in contrast to citrate-stabilized spheres (Liu and Guyot-Sionnest 2004; Becker et al. 2008). In a second step, this silver layer is replaced by gold:

$$3Ag^{0} + [AuCl_4]^{-} \rightarrow Au^{0} + 3Ag^{+} + 4Cl^{-} \quad (3.2)$$

A further addition of $HAuCl_4$ produces a porous Au cage around the rods (Fig. 3.3d). The size of the silver shell is 6 nm as estimated from the difference in the mean diameter between coated and bare rods measured on TEM images.

The second step is a galvanic replacement reaction between the silver shell and an aqueous $HAuCl_4$ solution at 100 °C. Hollow rattles form instead of a simple gold shell on a gold core due to the nanoscale Kirkendall effect (Kirkendall 1942; Yin et al. 2004; Fan et al. 2007; Yin et al. 2006). The higher diffusion rate of silver compared to that of gold and the imbalance of the material flow (see Eq. 3.2) lead to an accumulation of vacancies on the inner silver-gold interface (Meyer 1969). Depending on the amount of gold added in the second step, rattles with closed and porous outer shells are synthesized (Fig. 3.3).

The maximum of the extinction spectra corresponding to the longitudinal plasmon mode of the nanorattles is in-between the maxima for the initial gold nanorods and the silver-coated particles (Fig. 3.3e). The distance between the shell and the particle is small enough to lead to an effective plasmon coupling, creating a mode similar to the one of a completely filled nanoparticle with the same outer dimensions as the nanorattles. Since the nanorattles have a lower overall aspect ratio than the initial rods, the resonance wavelength is shifted slightly to the blue compared to the initial rods.

3.4 Synthesis of Silver Samples

To investigate the polarization anisotropy of differently shaped nanoparticles with the RotPOL setup (Sect. 5.2), silver samples with rod-, cubic- and triangular-shaped particles were synthesized. Typical TEM images of these synthesized silver nanoparticles are shown in Fig. 3.4.

3.4.1 Synthesis of Silver Nanocubes

Samples of silver nanocubes were obtained by reducing silver nitrate with ethylene glycol in the presence of PVP and a mM amount of sodium sulfide (Na_2S, Sigma-

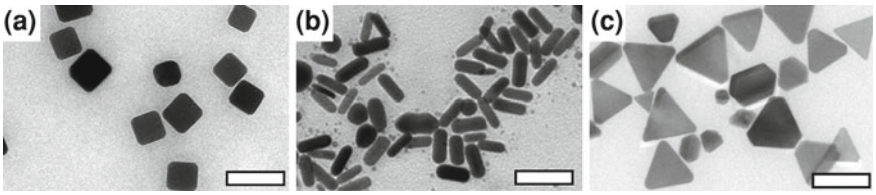

Fig. 3.4 TEM images of (**a**) rod-, (**b**) cubic-,(**c**) triangular-shaped particles used for polarization anisotropy measurements with the RotPOL setup (Sect. 5.2). Scalebar is 100 nm [Image reprinted with permission of the American Chemical Society (Becker et al. 2008)]

Aldrich) as described in reference (Siekkinen et al. 2006). The molar ratio between the PVP monomer and $AgNO_3$ is set to 1.9:1. The reaction time was 5 min.

3.4.2 Synthesis of Silver Nanorods

For the silver nanorod synthesis, we used the same approach as for cubes, but at higher temperature (180 °C) and longer reaction time (9 min). We used size-selective precipitation with acetone to separate rods from the other particles and remove excess of reactants.

3.4.3 Synthesis of Silver Nanotriangles

Silver triangles were synthesized by a photo-induced process (radiation time: 5 h) using poly(vinyl pyrrolidone) (PVP) and citrate anions. During illumination silver spherical colloids transform into triangular nanoplates according to literature procedure Sun and Xia (2003).

References

Becker, J., Zins, I., Jakab, A., Khalavka, Y., Schubert, O., & Sönnichsen, C. (2008). Plasmonic focusing reduces ensemble linewidth of silver-coated gold nanorods. *Nano Letters, 8*(6), 1719–1723.

Fan, H. J., Gösele, U., & Zacharias, M. (2007). Formation of nanotubes and hollow nanoparticles based on kirkendall and diffusion processes: A review. *Small, 3*(10), 1660–1671.

Khalavka, Y., Becker, J., & Sönnichsen, C. (2009). Synthesis of rod-shaped gold nanorattles with improved plasmon sensitivity and catalytic activity. *Journal of the American Chemical Society, 131*(5), 1871–1875.

Kirkendall, E. (1942). Diffusion of zinc in alpha brass. *Trans. AIME, 147*, 104–110.

Liu, M. Z., & Guyot-Sionnest, P. (2004). Synthesis and optical characterization of au/ag core/shell nanorods. *Journal of Physical Chemistry B, 108*(19), 5882–5888.

Meyer, R. O. (1969). Pressure and vacancy-flow effects on kirkendall shift in silver-gold alloys. *Physical Review, 181*(3), 1086.

Nikoobakht, B., & El-Sayed, M. A. (2003). Preparation and growth mechanism of gold nanorods (nrs) using seed-mediated growth method. *Chemistry of Materials, 15*(10), 1957–1962.

Siekkinen, A. R., McLellan, J. M., Chen, J. Y., & Xia, Y. N. (2006). Rapid synthesis of small silver nanocubes by mediating polyol reduction with a trace amount of sodium sulfide or sodium hydrosulfide. *Chemical Physics Letters, 432*(4–6), 491–496.

Sönnichsen, C., Franzl, T., Wilk, T., von Plessen, G., Feldmann, J., Wilson, O., et al. (2002). Drastic reduction of plasmon damping in gold nanorods. *Physical Review Letters, 88*(7), 077402.

Sun, Y. A., & Xia, Y. N. (2003). Triangular nanoplates of silver: Synthesis, characterization, and use as sacrificial templates for generating triangular nanorings of gold. *Advanced Materials, 15*(9), 695–699.

Sun, Y., Wiley, B., Li, Z.-Y., & Xia, Y. (2004). Synthesis and optical properties of nanorattles and multiple-walled nanoshells/nanotubes made of metal alloys. *Journal of the American Chemical Society, 126*(30), 9399–9406.

Yin, Y., Rioux, R. M., Erdonmez, C. K., Hughes, S., Somorjai, G. A., & Alivisatos, A. P. (2004). Formation of hollow nanocrystals through the nanoscale kirkendall effect. *Science, 304*(5671), 711–714.

Yin, Y., Erdonmez, C., & Alivisatos, A. P. (2006). Faceting of nanocrystals during chemical transformation: From solid silver spheres to hollow gold octahedra. Paper LBNL, (pp. 60696).

Chapter 4
Analytical Methods

Probably the most easiest characterization technique for nanoparticles is to measure the extinction spectrum of the sample (Sect. 4.1). Since in this measurement an ensemble of particles is investigated, darkfield-microscopy is used to investigate the scattering spectrum on a single particle level (Sect. 4.2). However, due to the diffraction limit of light, the nanoparticle's shape cannot be resolved in a light microscope, and therefore a transmission electron microscope is used for this purpose [Sect. 4.3, describes also energy-dispersive X-ray (EDX) electron microscopy]. Since the stabilizing molecules on the particle's surface cannot be imaged by this technique, the influence to the particle size of these molecules is measured with an approach based on dynamic light scattering (Sect. 4.4).

4.1 Ensemble Spectra

The characterization of the optical properties of an ensemble of nanoparticles in solution is obtained by the measurement of its extinction spectrum (fiber spectrometer: Ocean Optics, USB-2000). From this spectrum e.g. the resonance wavelength of the ensemble can be determined and a first estimation about the particles' shape can be performed. For example, spherical particles have an isotropic shape and therefore its extinction spectrum has only one resonance. In contrast, rodshaped particles have two resonances resulting from the longitudinal and the transversal resonance mode (Fig. 4.1a). In the case of gold nanorods, the resonance wavelength of the longitudinal mode can be used to estimate the aspect ratio (length/diameter) of the particles (Fig. 4.1b) according to Eq. 2.55:

$$\lambda_{\mathrm{res}}[\mathrm{nm}] = (137 \cdot \mathrm{AR} - 14)[\mathrm{nm/RIU}] \cdot n - (88 \cdot \mathrm{AR} - 457)[\mathrm{nm}] \qquad (4.1)$$

λ_{max}: position of the longitudinal resonance wavelength [nm]
AR: aspect ratio of the nanorods
n: refractive index of the surrounding medium.

J. Becker, *Plasmons as Sensors*, Springer Theses,
DOI: 10.1007/978-3-642-31241-0_4, © Springer-Verlag Berlin Heidelberg 2012

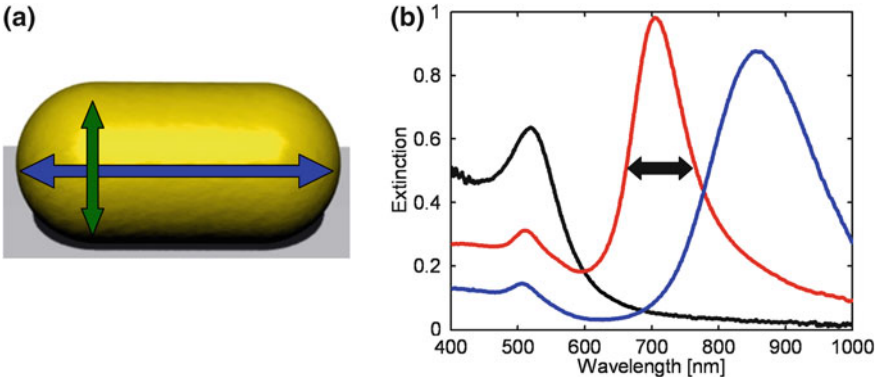

Fig. 4.1 **a** Rodshaped particles show a longitudinal (*blue arrow*) as well as a transversal (*green arrow*) resonance due to their non-isotropic shape. **b** Ensemble extinction spectra of gold spheres (*black*) and gold rods with different aspect ratio (AR = 3 and AR = 4, *red* and *blue lines*, respectively). While spherical particles have only one resonance peak, rods show two peaks resulting from the transversal and the longitudinal resonance mode. Thereby the position of the longitudinal peak strongly depends on the aspect ratio of the particles. The *arrow* indicates the linewidth (FWHM) of the ensemble spectrum, which is connected to the polydispersity of the sample

However, the particles in the ensemble are not all identical and therefore the resonance wavelength of each single particle varies. Since the ensemble peak is a superposition of all single particle resonances, it is broadened depending on the quality of the sample. For this reason, the linewidth (also termed: full width at half maximum, FWHM) of the ensemble extinction spectrum is an indicator for the polydispersity of the particles with a simple connection: the smaller the linewidth the better the quality of the sample. Furthermore, the concentration of the sample can be calculated using Lambert-Beer's law (Beer 1852):

$$E = c \cdot d \cdot \epsilon \tag{4.2}$$

$E = -\log_{10}(I_{\text{trans}}/I_{\text{reference}})$: extinction
c: concentration of particles in the sample [mol/L]
d: distance, the light has to travel through the absorbing media [cm]
ϵ: molar decadic extinction coefficient [L/(mol cm)]

which is true for diluted samples, with $E < 1$. For higher values of E, this simple equation is not valid anymore due to a possible change of ϵ because of multiple scattering events. To estimate the concentration of the samples, the molar decadic extinction coefficient of the particles in the sample is required. This coefficient can be calculated if the absorption cross-section σ of one single nanoparticle is known. The calculation of σ can either be done by Mie (for spherical particles), quasi-static-approximation (for small spheroidal particles) or by BEM or DDA (for all other shapes) (see Sects. 2.4.2 or 2.4.1, respectively). The required size and shape of the particles can be obtained from TEM imaging (Sect. 4.3). Using the following

formula, the molar extinction coefficient ϵ can be calculated (Lakowicz 2006):

$$\epsilon = \frac{N_A \cdot \sigma}{\ln(10)} \tag{4.3}$$

$N_A = 6.022 \cdot 10^{23}\ \mathrm{mol}^{-1}$: Avogadro constant
σ: absorption cross section of one single particle.

Insertion of the constants and subsequent conversion of units results in:

$$\epsilon / \left[\frac{\mathrm{L}}{\mathrm{mol\,cm}}\right] = 2.6 \cdot 10^6\, \sigma / [\mathrm{nm}^2] \tag{4.4}$$

4.2 Darkfield Microscopy

Since single metallic nanoparticles scatter light very efficiently, it is possible to investigate their scattering spectrum using a conventional transmission light microscope in dark-field mode (Zeiss, Axioskop Fig. 4.2a). In this approach, a dark-field condenser is implemented in the illumination path, which focuses the light onto the substrate (Fig. 4.2c). Using a condenser having a larger numerical aperture then the objective, direct light does not enter the objective. The numerical aperture $N.A.$ is hereby defined as the range of angles over which the system (objective or condenser) can accept or emit light:

$$N.A. = n \sin \alpha \tag{4.5}$$

α: half-angle of the maximum cone of light that can enter or exit the lens
n: refractive index of the medium in which the lens is working.

Using a condenser with a $N.A. = 1.2$–1.4 allows therefore the use of objectives with a $N.A.$ up to 1.2, which is fulfilled by all air- and most water-immersion objectives. Having objects in the focal plane scattering light, this light is able to enter the objective and therefore the resulting image will show bright spots on a dark background (Fig. 4.2d). The investigation of the light is carried out by a coupled spectrometer (Acton, SP-2150i), where the light gets dispersed by a grating (300 g/mm). Thereafter the spectrum is captured by a peltier-cooled (−75 °C) CCD camera (Princeton Instruments, Pixis400) (Fig. 4.2b).

Theoretically it would also be possible to investigate the particles in bright-field mode, where the sample is illuminated in conventional transmission. In this case the extinction of the particles is measured (Muskens et al. 2006). However, the extinction of the investigated nanoparticles is very small. Since it is difficult to measure very small losses ($\sigma_{\mathrm{ext}}/\pi \cdot r^2_{\mathrm{diffraction\ limit}} \sim 10^{-4}$ for a sphere with 20 nm in diameter) on a bright background compared to the initial described measurement of scattered light on a black background, the latter one is used.

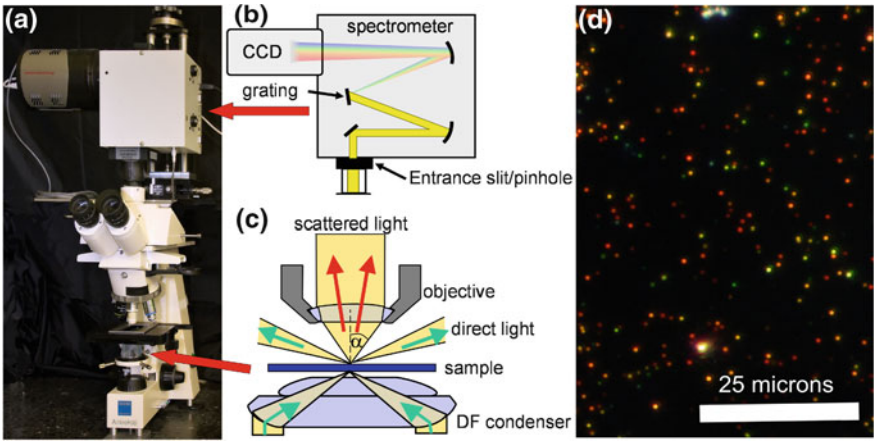

Fig. 4.2 **a** Picture of a conventional light microscope in darkfield mode, which is used to image gold nanorods and investigate them spectrally by a spectrometer and a coupled CCD camera (**b**). Illumination of the sample is through a darkfield oil immersion condenser (**c**), and therefore the direct light does not enter the objective and only the scattered light of the nanoparticles is collected. **d** The resulting image shows *bright spots* on a black background, each spot representing the scattered light of one single nanoparticle

4.3 Transmission Electron Microscopy

Since the investigated nanoparticles are smaller than the wavelength of visible light, it is not possible to resolve the shape of these particles by darkfield microscopy. Therefore a transmission electron microscope (TEM) is used to investigate the structural properties of the nanoparticles (Philips CM-12 and a FEI Tecnai-F30). Here the fundamental property is used that *all* matter (not just light) has a wave-like structure according to de Broglie (de Broglie 1924):

$$\lambda = \frac{h}{p} \tag{4.6}$$

λ: wavelength of the particle [m]
$h = 6.626 \cdot 10^{-23}$ Js: Planck's constant
p: relativistic momentum of the particle [kg m/s] $= \left[\sqrt{\text{kg J}}\right]$
$= \left[\sqrt{1.602 \cdot 10^{-19}\,\text{kg eV}}\right]$

In principle a TEM works similar to a light microscope, using accelerated electrons instead of photons. Magnetic lenses are used to guide the electrons (see Fig. 4.3).

The most common mode is the brightfield imaging mode, were the electrons are parallelized by the lenses in the microscope before hitting the specimen. In the case of a region containing a sample the electrons are scattered and the image appears dark, while regions without any sample will appear bright. The number of scattered

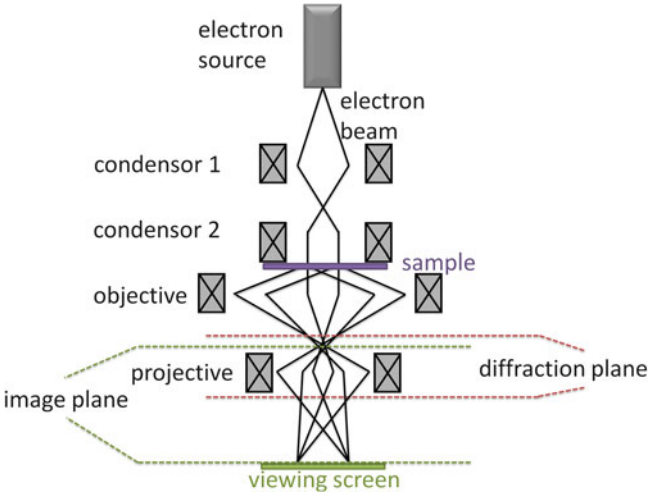

Fig. 4.3 Scheme of a transmission electron microscope. A TEM can in principle be compared to a light microscope, if photons are substituted for electrons. The bright field image plane is used to image the sample, while the diffraction image plane reveals the elemental composition of the sample

and absorbed electrons depends on the electron capture cross-section of the sample's material which scales with the atomic number Z and the material density. For this reason gold (Z = 79) appears darker compared to silver (Z = 47, see Fig. 3.2b).

Energy-Dispersive X-Ray Detection

To investigate the elemental composition of a sample, energy dispersive X-ray spectroscopy (EDX) is a common technique. Here, the accelerated electrons are focused on a very small spot where they interact with the electrons of the atoms in the sample. Therefore an electron of the atomic inner shell can be kicked out and leaves a hole. The atom is then in an excited state. This hole is filled by an electron from an outer shell. Since the electrons in the outer shell have more energy compared to electrons in the inner shell, the de-excitation leads to the emission of X-rays. The frequencies of those X-rays are unique for each element, which allows to characterize the elemental composition of the sample. Due to the focusing of the spot on a very small size, core-shell-structures composed of different elements can be resolved (see Fig. 3.2f).

4.4 Size Measurements by Dynamic Light Scattering

To measure the size of metal nanoparticles TEM is the ideal tool. But the metal particles are usually surrounded by molecules [e.g. citrate, cetrimonium bromide (CTAB) or polyethylenglycol (PEG)] to stabilize them against aggregation. Since these molecules do not show enough contrast in the TEM to estimate their size a

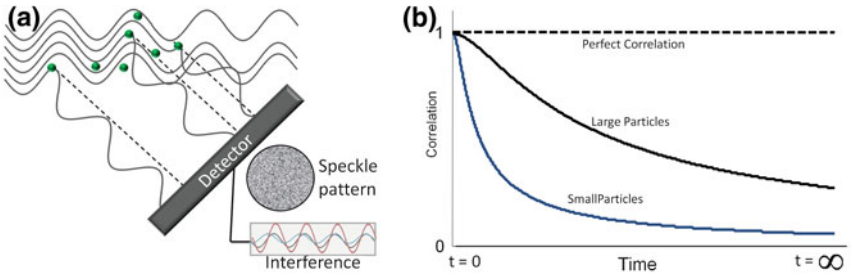

Fig. 4.4 **a** Scheme of an approach using the dynamic light scattering process. The particles in the sample scatter the propagating waves which leads to a speckle pattern on the detector (inset). **b** Correlation function for large and small particles. As can be seen, the rate of decay for the correlation function depends on the particle size [Image taken from Ref. (Malvern Instruments Ltd 2005)]

different approach is needed. One possibility is to measure the hydrodynamic radius using a process called dynamic light scattering (DLS). This procedure measures the diffusion constant of the Brownian motion and relates this to the size of the particles, using the attribute that this motion depends on the particle size (the larger the particles the slower they move). In practice a laser illuminates the sample and the light is scattered by the particles. Since many particles are illuminated at the same time, the scattered light interferes and therefore a speckle pattern will appear (Fig. 4.4a). As the particles are constantly in motion, this pattern will change over time. If the intensity signal of a particular part of the speckle pattern is continuously recorded the analysis by a auto-correlation function reveals the diffusion speed of the particles (Fig. 4.4b). The Brownian motion can be described by the diffusion constant D, which can be calculated via the Stokes-Einstein equation according to (Einstein 1905):

$$D = \frac{k_B \cdot T}{6\pi\,\eta r} \tag{4.7}$$

$k_B = 1.38 \cdot 10^{-23}$ [J/K]: Boltzmann constant
T: temperature
η: viscosity of the solvent
r: radius of the particle

which is related to the size of the particles if the viscosity of the suspension is known. With this setup the size of an absorbed molecule on the surface of particles can be investigated (Sect. 11.4). I performed such measurements using a commercial instrument of Malvern Instruments (model: Nano).

References

Beer, A. (1852). Bestimmung der Absorption des rothen Lichts in farbigen Flüssigkeiten. *Annalen der Physik, 162*(5), 78–88.

de Broglie, L. (1924). Recherches sur la théorie des quanta. Paris: Ph.D. Thesis.

Einstein, A. (1905). über die von der molekularkinetischen Theorie der Wärme geforderte Bewegung von in ruhenden Flüssigkeiten suspendierten Teilchen. *Annalen der Physik, 322*(8), 549–560.

Lakowicz, J. R. (2006). Principles of Fluorescence Spectroscopy (3rd ed., p. 59). New York: Springer.

Malvern Instruments Ltd. (2005). Zetasizer Nano Series User Manual (2.2th ed.). Malvern, UK: Worcestershire.

Muskens, O. L., Del Fatti, N., Vallee, F., Huntzinger, J. R., Billaud, P., & Broyer, M. (2006). Single metal nanoparticle absorption spectroscopy and optical characterization. *Applied Physics Letters, 88*(6), 063109.

Chapter 5
Novel Setups

Several techniques have been used to extract optical spectra of single plasmonic nanoparticles (Kalkbrenner et al. 2004; Van Dijk et al. 2005; Arbouet et al. 2004), most efficiently using dark-field microscopy. This setup investigates the spectrum of an individual nanoparticle by dispersing the scattered light with a spectrometer and capturing it with a connected charge-coupled device (CCD) camera. In setups used until now, one single particle is imaged onto a small pinhole in front of a spectrometer. Therefore it is only possible to investigate one single particle at the same time. The investigation of many particles was realized by manual moving each particle separately into the focus, which results in a very time consuming measurement. In this chapter I describe the development of a novel setup (fastSPS setup, Sect. 5.1), which measures the spectrum of all particles in the field of view automatically. Furthermore many particles are investigated at the same time, which results in an enormous decrease of the time needed for the measurement and the ability to monitor the spectra of many particles continuously in parallel. The development of the setup was performed with the help of Olaf Schubert and was published in the journal Nano Letters (Becker et al. 2007).

A second novel setup was also developed in collaboration with Olaf Schubert. It enables us to investigate the degree and direction of polarization of the scattered light of single nanoparticles (RotPOL setup, Sect. 5.2). Before, the polarization was obtained by rotating a polarizer stepwise by hand, missing spectroscopic information (Sönnichsen et al. 2002; Müller et al. 2002). The RotPOL setup automatically investigates the polarization pattern of many particles in parallel and the combination with a variable wavelength interference filter allow to measure the spectra of these particles. In a first approach, we investigate polarization patterns of dimers consisting of two equally sized gold nanospheres, gold and silver nanorods, silver nanocubes and silver nanotriangles. The description of the setup and the first obtained results have been published in reference (Schubert et al. 2008).

J. Becker, *Plasmons as Sensors*, Springer Theses,
DOI: 10.1007/978-3-642-31241-0_5,

5.1 The Fast Single-Particle Spectroscopy (FastSPS) Setup

Here, I present a novel fast single-particle spectroscopy method (fastSPS) based on an electronically addressable spatial shutter, which allows the simultaneous investigation of many particles in parallel with high temporal resolutions on a single-particle level in real time and in situ. The method is presently at least an order of magnitude faster than the traditional serial measurement, where each single particle was investigates separately. Furthermore, the FastSPS setup uses no mechanical parts or sample movement, which potentially allows this method to become an inexpensive, sturdy system for use outside of a laboratory environment, for example for medical sensoring applications (Raschke et al. 2003; Liu et al. 2006). We use fastSPS to study the growth process of rodshaped gold nanoparticles in the presence of surfactant molecules (Sect. 6.2) and to investigate the protein-membrane interaction on single nanoparticles (Chap. 7). Additionally the setup is used to show the increase of sensitivity of silvercoated gold rods (Sect. 9.2) and of gold nanorattles (Sect. 9.3) compared to bare gold nanorods. The FastSPS setup will also be useful for other realtime spectral monitoring applications such as the use of plasmon particles as labels in single-molecule studies (Sönnichsen et al. 2005; Liu et al. 2006).

Replacing the Entrance Slit with a Liquid Crystal Device (LCD)

To optically observe single nanoparticles, we use a standard transmission type dark-field microscope (Zeiss, Axioplan) (Sönnichsen et al. 2002; Sönnichsen and Alivisatos 2005; Sönnichsen 2001) with a high numerical aperture condenser (NA 1.2–1.4) and a 40x air objective (NA 0.75) coupled with an imaging spectrometer (SP-2150i, Acton; grating: 300 gr/mm; spectral resolution: 1.6 nm) and read out by a peltier-cooled (−75 °C) backilluminated charged-coupled device (CCD) camera (Pixis400, Princeton Instruments; 1340 × 400 pixels per $(20\ \mu m)^2$). The novel aspect is that we replace the entrance slit of the spectrometer by an electronically addressable liquid crystal device (LCD) (LC2002, Holoeye; 800 × 600 pixels (230 × 230 pixels used in our setup) with $(32\ \mu m)^2$ pixel size; response time: 40 ms; the pixel size corresponds to the diffraction-limited spot of one nanoparticle magnified by our 40x objective) (Fig. 5.1a). LCDs are currently used in a variety of optical setups including optical-sectioning fluorescence spectroscopy (Hanley et al. 1998) and speckle-illuminated confocal fluorescence microscopy (Jiang and Walker 2005), but have, to the best of my knowledge, not been used as a spatial addressable shutter for spectrometers. The LCD is placed in the image plane of the microscope so that each of its pixels corresponds to a distinct point in the focal plane of the objective and effectively acts as an individual electronically addressable shutter for this area. Furthermore the LCD is at the same time placed in the entrance plane of an imaging spectrometer. By setting an LCD pixel to transparent, a corresponding particle is spectrally investigated. Currently, the spectrometer allows the imaging of up to 20 vertically separated spectra on the CCD chip before overlap between spectra becomes problematic. By using more sophisticated spectrometer optics, it can be expected to improve this value considerably in a future system.

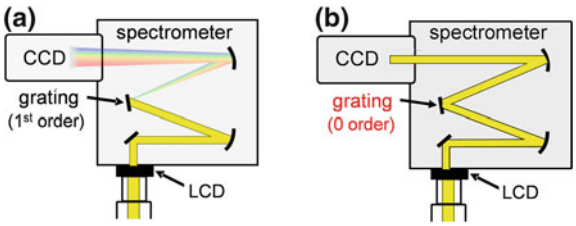

Fig. 5.1 **a** Scheme of the spectrometer of the fastSPS setup, where the entrance slit of the spectrometer is replaced by an electronically addressable liquid crystal device (LCD) placed in the microscope's image plane. **b** To take an image of the sample the grating is moved to zero's order and operates then as a mirror

Acquiring the Spectra

In a standard measurement, first all LCD pixels are set to transparent and a black-and-white image of the whole sample is taken by moving the spectrometer grating to zero's order (Fig. 5.1b). In principle, a second camera attached to another output port of the microscope could be used for this as well, which would further speed up the measurement. N nanoparticles are then selected by hand or by setting a threshold, which differs bright spots from background noise. The nanoparticle positions $(X_\mathrm{i}, Y_\mathrm{i})$ are arranged into n nonhorizontally overlapping groups (G^n) of up to 20 particles. Each group (G^n) is then measured consecutively by setting the corresponding pixels to transparent (Fig. 5.2). The resulting images (I_n) are decomposed into the particle spectra (S_i), taking into account a small wavelength shift due to the horizontal position offset $(X_\mathrm{i} - X_\mathrm{c})$ from the center of the spectrometer entrance (X_c). A dark image (I^0), taken by setting all pixels to black, can be subtracted from all images (I^n) to account for light leaking through black LCD pixels despite the >1:1000 contrast achievable with LCD displays. Furthermore, the spectra (S_i) need to be corrected for background from diffuse light originating from out-of-focus areas of the sample, i.e., dust on the glass surface. Therefore, one additional spectrum (S_0) from a point of the sample without a particle is measured and subtracted from each particle spectrum (S_i). Finally, the spectra are normalized to the spectral characteristic determined for a "white" particle (W), either dust or large silicon dioxide beads, $S_\mathrm{final} = (S_\mathrm{i} - S_0)/W$. After these corrections, the spectra are smoothed over 5 points (4 nm) and the maximum of the plasmon resonance is determined by a parabolic fit around the absolute maximum. The stability of the setup, determined by observing a single particle continuously for about 3 h, shows subnanometer deviations limited mainly by focus drift (Fig. 5.3a).

Measuring Speed of the FastSPS Setup

To compare the speed of our new fastSPS setup with other methods for spectral investigation of particles in a microscope, it is important to realize that the density of randomly deposited particles on the substrate is necessarily low in single-particle studies. Because the diffraction limit makes it impossible to reliably distinguish

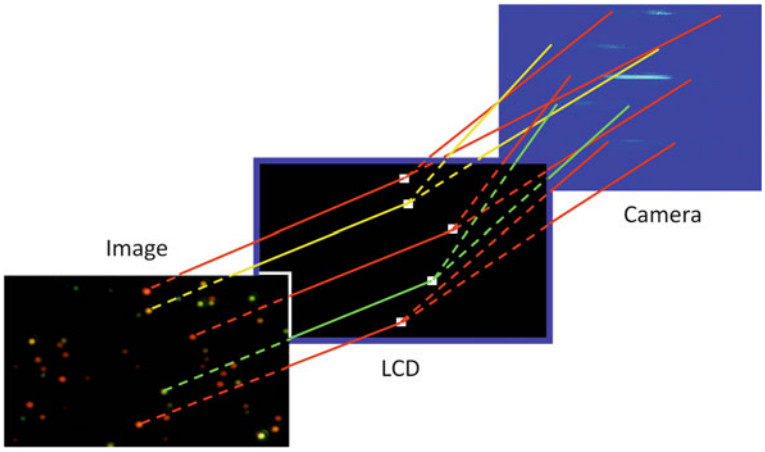

Fig. 5.2 Each of the LCD pixels acts as an electronically addressable shutter for a small area of the sample. LCD pixels which are corresponding to vertically separated particles are set to transparent in order to spectrally investigate those particles simultaneously [Image reprinted with permission of the American Chemical Society (Becker et al. 2007)]

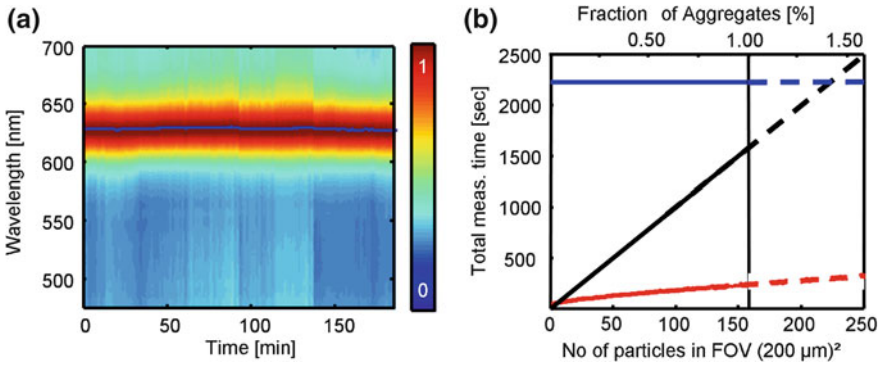

Fig. 5.3 **a** Continuous measurement of the same particle with the fastSPS setup to test its stability. The spectra have a mean of 628.6 nm, a standard deviation of 0.65 nm and a maximal deviation of 1.58 nm. Refocusing (after about 90 and 140 min) leads to a maximal change of 1.47 nm (*stripes in the image*). The maximal deviation between two consecutive measurements is 0.58 nm. **b** For randomly deposited particles, higher particle densities on the sample (*lower horizontal axis*) lead to a higher percentage of more than one particle in a diffraction limited spot (*particle aggregates, upper horizontal axis*). The total measurement time for all particles in the field of view increases linearly for a serial method (*black line*) and is independent for all spectral imaging methods, which determine the spectra of all points in the field of view (*blue line*). The fastSPS method (*red line*) is by far the fastest method for realistic particle densities around 160 particles in the field of view (FOV = 200 μm)^2 corresponding to roughly 1 % of particle aggregates [Image reprinted with permission of the American Chemical Society (Becker et al. 2007)]

two particles from a single particle, if they are closer than the current resolution, the only way to investigate single particles (on average) is to dilute them on the substrate up to a point where it is very unlikely to find two particles in the same diffraction limited spot. The probability p of such "aggregates" is given by $p = 1 - (1 - N/M)^m$ with N the number of particles in the field of view, M the number of "absorption areas" in this field of view, assuming that one absorption area has the size of one nanoparticle and m is the size of the optical resolution as a multiple of the absorption area. p increases to more than 1 % of the deposited particles for densities around 160 particles in the field of view of $(200\ \mu\text{m})^2$ assuming a resolution of 900 nm. Any method measuring the spectra of each point in the field of view ("spectral imaging") produces therefore a vast amount of unnecessary data. Several technical possibilities exist for realizing such a spectral imaging approach, from scanning the illumination wavelength (Liu et al. 2005), using an interferometric approach (Gemperlein 1988) to moving the sample relative to the entrance slit of the spectrometer (Herrala and Okkonen 1996; Kim et al. 2001). Depending on particle density, automatization grade, speed of sample movement, etc., the more traditional "serial" approach of investigating exactly the particle in the center of view and positioning all particles of interest in this spot consecutively is usually faster for low particle densities. Figure 5.3b numerically compares our fastSPS approach using a spatial addressable shutter with the serial and spectral imaging method for different particle densities. In addition, we have compared the fastSPS setup with spectral imaging realized by moving the spectrometer with a fixed entrance slit relative to the sample with a stepper motor (Fig. 5.3b). Both, simulation and experiment show at least an order of magnitude faster spectra acquisition time for realistic particle densities of about 160 particles per $(200\ \mu\text{m})^2$. We have adjusted the exposure time of the fastSPS method in these calculations to account for light blocked by the LCD's polarization filters (about 60 % of the incoming light). It will be, however, relatively simple to circumvent this issue by splitting the light into two optical pathways of orthogonal polarization with a polarizing beam splitter and using two LCD displays. In this improved configuration, not only spectral but also orientation information can be gained, which can be used to extract particle orientation of optically anisotropic particles (Sönnichsen and Alivisatos 2005; Muskens et al. 2006).

5.2 The Polarization Resolved Spectroscopy (RotPOL) Setup

Polarization analysis of light from single fluorescent emitters has been a major advancement in single molecule optics used to study the conformational dynamics of biomolecules and their spatial arrangement (Weiss 2000). There are several techniques (among them polarization modulation (Ha et al. 1999), defocusing (Bartko and Dickson 1999; Toprak et al. 2006), back-plane imaging (Lieb et al. 2004), or polarization analysis (Chung et al. 2003)), which give the orientation of an emission or absorption dipole but not the degree and symmetry of the emitted light polarization itself. For the dipolar emission of typical fluorescent molecules, the $\cos^2\theta$

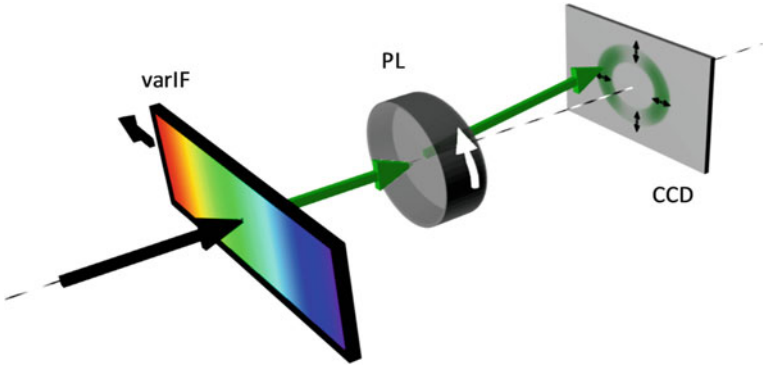

Fig. 5.4 Schematics of the rotPOL setup. One wavelength is selected by a linear variable interference filter (varIF), then the light is dispersed into the different polarization directions by a wedge-shaped rotating polarizer (PL), resulting in ring-shaped intensity profiles of a pointlike light source on the digital camera [Image reprinted with permission of the American Chemical Society (Schubert et al. 2008)]

dependency of the light intensity on the polarization angle θ is well known and usually not at the center of interest. For larger nanoparticles, the light emission is not necessarily of dipolar character (Nelayah et al. 2007). In particular, the resonant light scattering from plasmons in noble metal particles is expected to show the symmetry of the oscillation mode and the particle shape. At different wavelengths of the excitation light, different oscillation modes are excited making it important to know the polarization pattern as a function of wavelength. Knowing the polarization pattern of plasmonic nanostructures is therefore not only important to understand the fundamental physics of light interaction with these structures, but allows one to discriminate different oscillation modes within one particle and to distinguish differently shaped particles within one sample.

Description of the RotPOL Setup

The unique component for the polarization resolved single particle spectroscopy (rotPOL) is a rotating polarizer (Fig. 5.4).

We use a standard polarization filter (analyzer for polarization contrast imaging) rotated by an external motor at a frequency of more than 4 Hz. The polarizer slightly displaces the image by a few pixels, which means that images taken with exposure times longer than the full rotation time will show a ring in the image plane for a normally point-like single particle and therefore encodes the polarization information in a spatial image (Fig. 5.5a). Each point on the ring corresponds to the light intensity $I(q)$ in the corresponding polarization direction. A dipole, for example, will show two loops at opposite sides (Fig. 5.5b). We combine this rotating polarizer with a standard transmission dark-field microscope with white light excitation from a 100 W halogen lamp, 40x water-immersion objective (NA 0.8) and a high numerical aperture condenser (NA 1.2–1.4). To simultaneously record spectral and

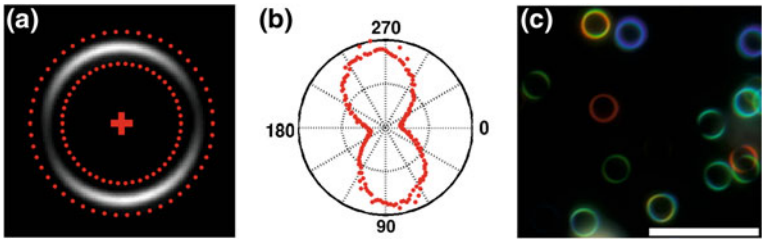

Fig. 5.5 **a** The wedge-shaped rotating polarizer encodes the polarization information in a spatial image. **b** In order to get the polarization profile (intensity $I(\theta)$ as a function of polarization angle θ), the image is integrated between an inner and outer ring diameter (*dashed lines in panel b*)). The center of the rings is chosen to minimize asymmetry between opposite sides. **c** Real-color image of an inhomogeneous silver nanoparticle sample containing spheres, rods, and triangles as seen through the rotPol-microscope. Two colors in one ring correspond to two different plasmon modes at the respective wavelengths. Scalebar is 25 μm [Image reprinted with permission of the American Chemical Society (Schubert et al. 2008)]

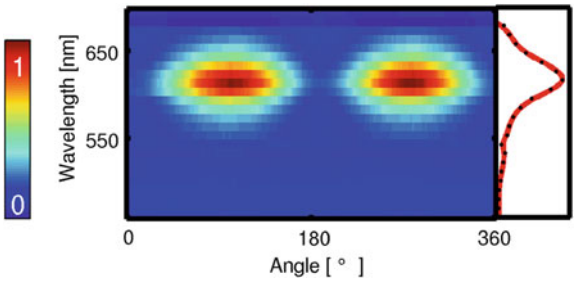

Fig. 5.6 By inserting a variable wavelength interference filter the polarization profile is determined for a single wavelength. Repeating this procedure for a wavelength regime (by moving the interference filter with a stepper motor) produces intensity values as a function of wavelength and polarization angle $I(\lambda, \theta)$, which is shown here color-coded [Image reprinted with permission of the American Chemical Society (Schubert et al. 2008)]

polarization information (Fig. 5.6) we place a variable wavelength interference filter (varIF, *VERIL S 200*, Schott AG, 400–700 nm) in front of the digital camera (either a peltier-cooled CCD (CoolSnapHQ2, Photometrics) or a consumer digital DSL camera (EOS 400D, Canon)). In this case, the measured intensity $I(q)$ is the polarization dependent scattering intensity $I(q, \lambda)$ at the corresponding transmission wavelength λ_0 of the filter. Polarization and spectral dependent scattering spectra $I(q, \lambda)$ are obtained by moving the interference filter with a stepper motor (T-LLS260, Zaber Technologies Inc.) and recording one image for each position with the exposure time adjusted to correct for the spectral characteristics of the setup. We extract the polarization dependent scattering intensity $I(q)$ for each frame with an image analysis algorithm, which finds the center of each ring by minimizing the differences between the intensity of opposite sides of the ring. A starting point for the algorithm is pro-

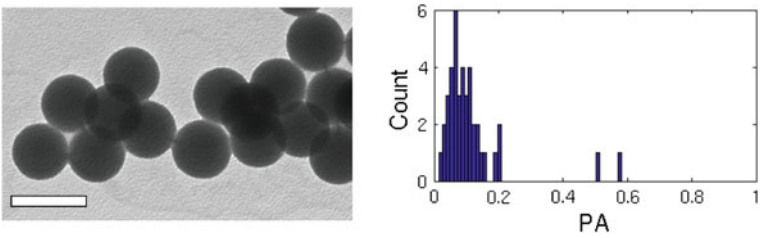

Fig. 5.7 **a** TEM-image (scalebar: 500 nm) of SiO_2-spheres and **b** results of a measurement of these perfectly spherical particle, sing the rotPOL-setup. The imperfections of the optical components induce an error of about 0.1 in the polarization anisotropy (PA) [Image reprinted with permission of the American Chemical Society (Schubert et al. 2008)]

vided by summing all frames up and selecting the particles by hand. The intensity at the center of the ring is used to correct for background signal (i.e. CCD-noise and scattering from out-of focus dust particles). A real color image of nanoparticles in the RotPOL setup can be seen in Fig. 5.5c.

Calculation of the Polarization Anisotropy

The combination (rotPOL, varIF) allows the recording of single particle scattering spectra $I(\lambda)$, the polarization anisotropy PA(λ), and/or the determination of full wavelength and polarization dependent scattering intensity $I(\theta, \lambda)$ for up to 50 particles in parallel. The polarization anisotropy PA(λ) is defined as (Yguerabide and Yguerabide 1998):

$$\mathrm{PA}(\lambda) = (I_\mathrm{a} - I_\mathrm{b})/(I_\mathrm{a} + I_\mathrm{b}), \tag{5.1}$$

where I_a and I_b correspond to the scattering intensity of light polarized parallel to the major and minor particle axis, respectively. For rodlike particles, the PA(λ) may become negative near the short axis resonance, where I_b is high. The polarization inhomogeneity of the setup itself is tested, by measuring polarization-dependent spectra of perfectly spherical SiO_2-spheres (Ø 314 nm, Corpuscular Inc.) and obtained a median PA of 0.1 (Fig. 5.7). This corresponds to the error in the polarization values obtained in this work.

Performance of the Setup

A polarization dependent spectral image (450–700 nm, spectral resolution: 5 nm, angle resolution 1–2°) with a field of view of 133 × 100 µm (with a 40x objective) takes about 10–20 min, depending on the exposure time and the sample studied. The stability of the setup is tested by measuring one sample repeatedly (Fig. 5.8).

Furthermore the rotPOL method is not limited to non-changing samples, but may record polarization dependent particle spectra with high temporal resolution, especially if high spectral resolution is not required. In this case, instead of the variable wavelength interference filter and the peltier-cooled digital camera a digital

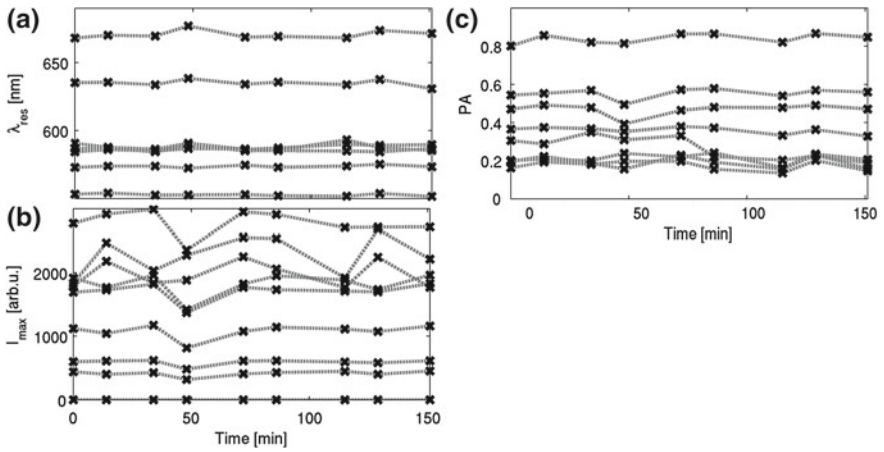

Fig. 5.8 Stability of the setup. The same particles were measured repeatedly for more than two hours. The standard deviation is below 1, about 6 and about 10 % for the resonance energy, PA and maximum intensity, respectively [Image reprinted with permission of the American Chemical Society (Schubert et al. 2008)]

consumer camera (EOS 400D, Canon) is used. The images are then taken with an exposure time between 10 and 30 s and an ISO setting between 100 and 400 and the spectral information can be gained from the RGB colors of these images. With this setup the PA of nanorods exposed to a growth solution was investigated (see Sect. 6.3).

5.2.1 First Results Obtained With RotPOL

To explore the possible polarization states of simple plasmonic nanostructures, we determine the wavelength and polarization dependent scattering intensity $I(\theta, \lambda)$ of gold and silver nano-rods, -triangles, gold nanospheres, and pairs of these spheres (representative examples in Fig. 5.9), the gold spheres were purchased from BBI international, UK. Synthesis procedures of the silver samples are described in Sect. 3.4.

Comparison with Theory

To compare our experimental results to theory, we simulated polarization dependent spectra of rod-shaped, cubic, and triangular gold and silver particles within the discrete dipole approximation (DDA, Sect. 2.4.1) using the particle sizes and shapes determined by transmission electron microscopy (TEM, Sect. 4.3). Particle sizes and shapes vary significantly within one batch of nanoparticles. Since we are not able to measure identical particles with rotPOL and TEM, the simulations have some degree of freedom regarding the precise particle dimensions.

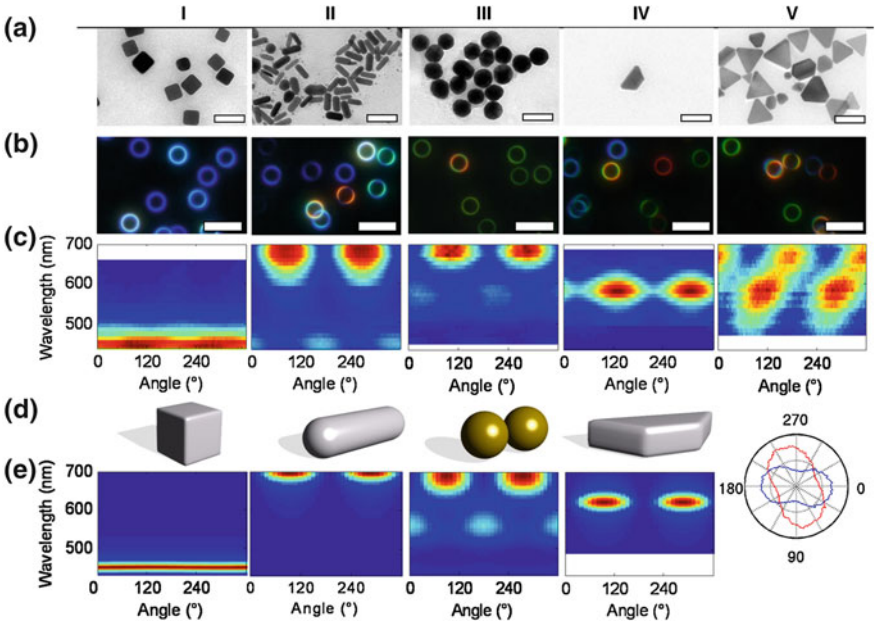

Fig. 5.9 Typical plasmon polarization results for simple gold and silver plasmonic nanostructures. **a** TEM images of samples containing silver (*I, II, IV, V*) and gold (*III*) nanoparticles (scale bar: 100 nm). In line **b**, typical real-color microscopic images of those samples are shown (scale bar: 15 μm). The polarization dependent single-particle-scattering-spectra $I(\lambda, \theta)$ of representative particles are shown in **c** color-coded as in Fig. 5.6. These results can be compared to simulations by discrete dipole approximation shown in **e** with the model sketched in **d**. For the triangular particle in column V, a polar graph of the intensity $I(\theta)$ at the two particle resonances visible in Vc is shown in the bottom panel. Two loops with the expected 60° offset are clearly visible [Image reprinted with permission of the American Chemical Society (Schubert et al. 2008)]

The qualitative results for all investigated nanoparticles agree well with simulations. Interestingly the complete absence of polarization anisotropy for silver cubes, both theory and experiment surprises at first. However, two orthogonal dipoles with $\cos^2\theta$ intensity dependency cancel each other out completely ($\cos^2\theta + \sin^2\theta = 1$). Rods show the expected dipolar behavior with sometimes the short axis peak visible at lower wavelength in the orthogonal direction. In samples containing only spheres, some particles show an unexpectedly high PA combined with a red-shifted resonance wavelength. The polarization dependent spectra of these particles agree well with simulations of a pair of two spheres within close distance. The shift of the plasmon mode along the interparticle axis ("long axis") depends strongly on the interparticle distance (Reinhard et al. 2005). Measuring $I(\lambda, \theta)$ allows the extraction of the orientation of the particle pair, the interparticle spacing ("plasmon ruler") (Sönnichsen et al. 2005) and may allow the construction of a "self-calibrating" plasmonic ruler insensitive to changes in the dielectric environment (Chap. 11). Samples containing triangles show very often "rodlike" resonances, which is probably due to a shape

asymmetry of the triangles. DDA simulations of such "truncated triangles" show reasonable agreement with measured spectra. Since it is not easily possible to correlate directly particle shape and optical spectra and our samples of triangles are particularly polydisperse, the interpretation remains tentative. In some polarization spectra $I(\lambda, \theta)$, we observe the 60° symmetry expected for triangles. In the cases where we observed this 60° symmetry, each resonance was shifted in wavelength (Fig. 5.9, particle V), again most likely due to small differences for the plasmon modes in the direction of the three corners. We were not able to simulate the polarization spectrum $I(\lambda, \theta)$ of such particles so far due to the high number of possible ways to modify the corners.

Closer Look on Nanorods

Nanorods are the most often used and conceptually most simple "antenna-like" plasmonic structures, and it is therefore important to study their emission pattern more closely. We synthesized gold nanorods (average sizes determined from TEM: 57×28 nm) according to Sect. 3.1 and measured polarization dependent single particle scattering spectra $I(\lambda, \theta)$ for these particles and compare those with two batches of spherical gold particles with nominal diameters of 60 and 80 nm, respectively. First, we extract the polarization anisotropy PA at the resonance wavelength λ_{res}. As expected, rod-shaped particles show a high degree of polarization anisotropy (average $\text{PA}(\lambda_{\text{res}}) = 0.84$, Fig. 5.10a) (Sönnichsen et al. 2002) while spherical particles have an average $\text{PA}(\lambda_{\text{res}})$ of about 0.35 (Fig. 5.10a). Looking at the polarization anisotropy $\text{PA}(\lambda)$ over the full optical spectrum, we observe almost no wavelength dependency for spheres, but a strong spectral dependency for rods. This reflects the lack of excitation of the long-axis plasmon mode with light-waves out-of resonance. Surprisingly the spheres showed a $\text{PA}(\lambda_{\text{res}})$ much greater than zero, but this could be explained by the fact that the nominally round particles have a mean aspect ratio (shape anisotropy) determined from TEM images of about 1.1 (Fig. 5.11).

Simulations for Ag, Au, and SiO_2-particles (Fig. 5.10c) show that the strong sensitivity of the polarization anisotropy is a plasmonic effect: gold and silver nanoparticles with an aspect ratio as low as 1.8 and 1.6 (respectively) already have a PA of 0.9, for SiO_2 this value is reached only for an aspect ratio of 4. The plasmon damping in silver is lower than in gold, which may explain the steeper $\text{PA}(a/b)$ function. These theoretical results explain the unexpectedly high polarization anisotropy of nominally round gold spheres.

5.3 Conclusion

In this chapter I presented two novel setups (fastSPS and RotPOL) I developed, to investigate automatically the scattering spectra of many nanoparticles.

The fast single particle spectroscopy (fastSPS) setup is optimized to measure automatically the scattering spectra of all plasmonic nanoparticles in the field of view with high temporal resolution, and is currently an order of magnitude faster

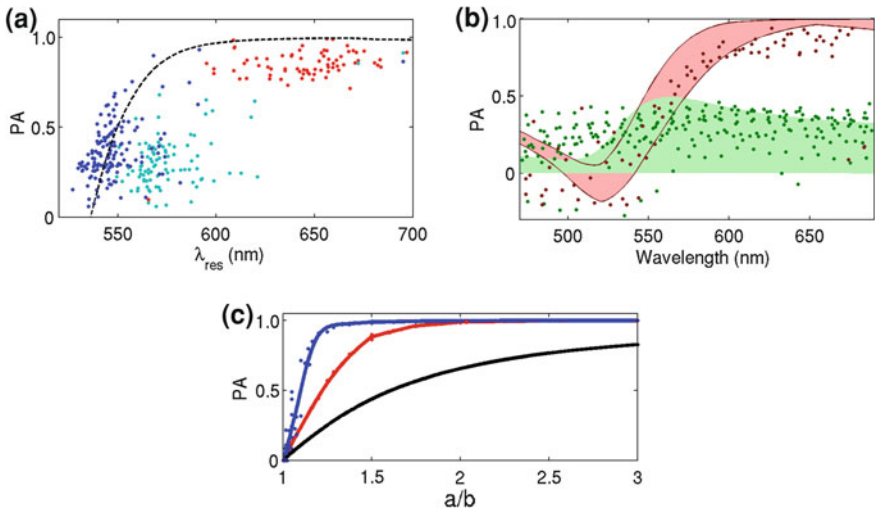

Fig. 5.10 **a** The polarization anisotropy $\mathrm{PA}(\lambda_{\mathrm{res}}) = (I_{\mathrm{a}} - I_{\mathrm{b}})/(I_{\mathrm{a}} + I_{\mathrm{b}})$ at the longitudinal plasmon resonance wavelength λ_{res} is shown as a function of the resonance wavelength for three different gold particle samples (*blue dots*) nominally spherical gold particles with 60 nm diameter; *teal dots* 87 nm diameter; and *red dots* gold nanorods). We extract each point from a full wavelength and polarization dependent single particle scattering spectrum $I(\lambda, \theta)$. *The dashed black line* is a theoretical prediction from simulations of gold rods of different aspect ratios and sizes embedded in water (refractive index $n = 1.34$). The polarization anisotropy $\mathrm{PA}(\lambda)$ for a given particle varies as a function of wavelength λ, which we show in **b** for gold rods (*red dots*) and spheres (*green dots*). The *shaded red* and *green areas* correspond to theoretical predictions for particles with aspect ratios (a/b) of $2 < a/b < 3$ and $a/b < 1.2$, respectively. The theoretical prediction of polarization anisotropy PA at the resonance wavelength as a function of aspect ratio (a/b) for silver (*blue dots*), gold (*red dots*) and SiO_2 (*black dots*) particles is shown in **c**. Dots correspond to DDA-simulations, the lines are fits. The simulations do not perfectly follow a common trend due to a small influence of particle volume on the polarization anisotropy [Image reprinted with permission of the American Chemical Society (Schubert et al. 2008)]

than other methods. Additionally up to 30 particles can be monitored continuously at the same time. In principle, the spectrometer's entrance pinhole is replaced by an electronically addressable spatial shutter (liquid crystal device - LCD), and therefore no mechanically moving parts are required. This enables the possibility to implement this device in small, robust future devices, e.g., for ultrasmall volume sensors "in the field".

However, due to the utilized polarizers in the LCD, particles having their resonance with a perpendicular orientation to the polarizer direction cannot be investigated. Furthermore, these polarizers are only usable in the wavelength range of 450–700 nm. To dispose these drawbacks, the LCD could be exchanged by an digital micromirror device (DMD, trademark of Texas Instruments), consisting of several thousands microscopic mirrors. Each of these mirrors can be rotated separately and therefore this device acts also as an shutter if the appropriate mirrors are reflecting the light

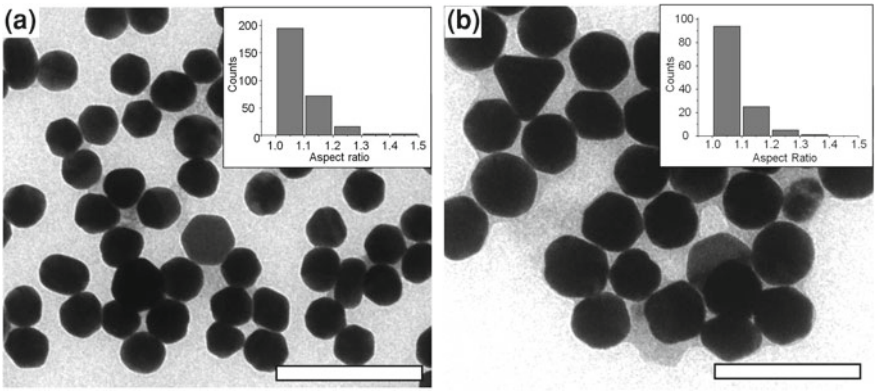

Fig. 5.11 Shape of gold nanospheres (BBI Inc. UK.) determined from TEM images for 60 nm particles (**a**) and 80 nm particles (**b**) (scalebars 200 nm). Histograms of the aspect ratio determined from such TEM images for more than 100 particles per sample are shown in the appropriate insets. The nominally round particles have a mean aspect ratio (shape anisotropy) of about 1.1 for both samples, which is enough to induce strongly polarized light scattering [Image reprinted with permission of the American Chemical Society (Schubert et al. 2008)]

into the spectrometer. The advantages compared to the LCD are an enlarged applicable wavelength range as well an independency of the polarization direction of the incoming scattered light.

The rotPOL method is a versatile tool to study polarization anisotropy of the light emission pattern from nanoparticles, especially for plasmonic structures but possibly also for fluorescent quantum structures. Furthermore, the possibility to record dynamic changes of the polarization emission pattern of single particles allows studying particle modes in situ. In a first test experiment, the polarization anisotropy of different particle morphologies (spheres, rods, triangles, cubes, and particle pairs) were investigated. The observed large variety of plasmon emission patterns provides a wide field for optimization of applications such as light guiding and allows detailed theoretical modeling of plasmon modes. The high polarization anisotropy, found even for only moderately elongated spheres highlights the strong influence of polarization even for nominally round particles.

Both setups were used to monitor spectrally the further growth of rodshaped nanoparticle in situ (Chap. 6). Additionally, the fastSPS setup was used to investigate protein membrane interactions (Chap. 7) as well as to investigate the sensing properties on changes in the refractive index of the environment of silver coated gold nanorods and hollow gold nanorattles (Chap. 9).

References

Arbouet, A., Christofilos, D., Del Fatti, N., Vallee, F., Huntzinger, J. R., Arnaud, L., et al. (2004). Direct measurement of the single-metal-cluster optical absorption. *Physical Review Letters, 93*(12), 127401.

Bartko, A. P., & Dickson, R. M. (1999). Imaging three-dimensional single molecule orientations. *Journal of Physical Chemistry B, 103*(51), 11237–11241.

Becker, J., Schubert, O., & Sönnichsen, C. (2007). Gold nanoparticle growth monitored in situ using a novel fast optical single-particle spectroscopy method. *Nano Letters, 7*(6), 1664–1669.

Chung, I. H., Shimizu, K. T., & Bawendi, M. G. (2003). Room temperature measurements of the 3d orientation of single cdse quantum dots using polarization microscopy. *Proceedings of the National Academy of Sciences of the United States of America, 100*(2), 405–408.

Gemperlein, R. (1988). Fourier interferometric stimulation (fis) in biology and medicne. *Microchimica Acta, 94*, 353–356.

Ha, T., Laurence, T. A., Chemla, D. S., & Weiss, S. (1999). Polarization spectroscopy of single fluorescent molecules. *Journal of Physical Chemistry B, 103*(33), 6839–6850.

Hanley, Q. S., Verveer, P. J., & Jovin, T. M. (1998). Optical sectioning fluorescence spectroscopy in a programmable array microscope. *Applied Spectroscopy, 52*(6), 783–789.

Herrala, E., & Okkonen, J. (1996). Imaging spectrograph and camera solutions for industrial applications. *International Journal of Pattern Recognition and Artificial Intelligence, 10*(1), 43–54.

Jiang, S. H., & Walker, J. G. (2005). Non-scanning fluorescence confocal microscopy using speckle illumination and optical data processing. *Optics Communications, 256*(1–3), 35–45.

Kalkbrenner, T., Hakanson, U., & Sandoghdar, V. (2004). Tomographic plasmon spectroscopy of a single gold nanoparticle. *Nano Letters, 4*(12), 2309–2314.

Kim, M. S., Chen, Y. R., & Mehl, P. M. (2001). Hyperspectral reflectance and fluorescence imaging system for food quality and safety. *Transactions of the Asae, 44*(3), 721–729.

Lieb, M. A., Zavislan, J. M., & Novotny, L. (2004). Single-molecule orientations determined by direct emission pattern imaging. *Journal of the Optical Society of America B-Optical Physics, 21*(6), 1210–1215.

Liu, G. L., Doll, J. C., & Lee, L. P. (2005). High-speed multispectral imaging of nanoplasmonic array. *Optics Express, 13*(21), 8520–8525.

Liu, G. L., Yin, Y. D., Kunchakarra, S., Mukherjee, B., Gerion, D., Jett, S. D., et al. (2006). A nanoplasmonic molecular ruler for measuring nuclease activity and dna footprinting. *Nature Nanotechnology, 1*(1), 47–52.

Müller, J., Sönnichsen, C., von Poschinger, H., von Plessen, G., Klar, T. A., & Feldmann, J. (2002). Electrically controlled light scattering with single metal nanoparticles. *Applied Physics Letters, 81*(1), 171–173.

Muskens, O. L., Del Fatti, N., Vallee, F., Huntzinger, J. R., Billaud, P., & Broyer, M. (2006). Single metal nanoparticle absorption spectroscopy and optical characterization. *Applied Physics Letters, 88*(6), 063109.

Nelayah, J., Kociak, M., Stephan, O., de Abajo, F. J. G., Tence, M., Henrard, L., et al. (2007). Mapping surface plasmons on a single metallic nanoparticle. *Nature Physics, 3*(5), 348–353.

Raschke, G., Kowarik, S., Franzl, T., Sönnichsen, C., Klar, T. A., Feldmann, J., et al. (2003). Biomolecular recognition based on single gold nanoparticle light scattering. *Nano Letters, 3*(7), 935–938.

Reinhard, B. M., Siu, M., Agarwal, H., Alivisatos, A. P., & Liphardt, J. (2005). Calibration of dynamic molecular rule based on plasmon coupling between gold nanoparticles. *Nano Letters, 5*(11), 2246–2252.

Schubert, O., Becker, J., Carbone, L., Khalavka, Y., Provalska, T., Zins, I., et al. (2008). Mapping the polarization pattern of plasmon modes reveals nanoparticle symmetry. *Nano Letters, 8*(8), 2345–2350.

Sönnichsen, C. (2001). *Plasmons in metal nanostructures*. München: Cuvillier Verlag Göttingen.

Sönnichsen, C., & Alivisatos, A. P. (2005). Gold nanorods as novel nonbleaching plasmon-based orientation sensors for polarized single-particle microscopy. *Nano Letters, 5*(2), 301–304.

Sönnichsen, C., Franzl, T., Wilk, T., von Plessen, G., Feldmann, J., Wilson, O., et al. (2002). Drastic reduction of plasmon damping in gold nanorods. *Physical Review Letters, 88*(7), 077402.

Sönnichsen, C., Reinhard, B. M., Liphardt, J., & Alivisatos, A. P. (2005). A molecular ruler based on plasmon coupling of single gold and silver nanoparticles. *Nature Biotechnology, 23*(6), 741–745.

Toprak, E., Enderlein, J., Syed, S., McKinney, S. A., Petschek, R. G., Ha, T., et al. (2006). Defocused orientation and position imaging (dopi) of myosin v. *Proceedings of the National Academy of Sciences of the United States of America, 103*(17), 6495–6499.

Van Dijk, M. A., Lippitz, M., & Orrit, M. (2005). Far-field optical microscopy of single metal manoparticies. *Accounts of Chemical Research, 38*(7), 594–601.

Weiss, S. (2000). Measuring conformational dynamics of biomolecules by single molecule fluorescence spectroscopy. *Nature Structural Biology, 7*(9), 724–729.

Yguerabide, J., & Yguerabide, E. E. (1998). Light-scattering submicroscopic particles as highly fluorescent analogs and their use as tracer labels in clinical and biological applications - i. theory. *Analytical Biochemistry, 262*(2), 137–156.

Chapter 6
Single Gold Nanoparticle Growth Monitored in situ

The novel fastSPS setup (see Sect. 5.1) is used to study the growth process of rodshaped gold nanoparticles in the presence of surfactant molecules. It is observed that the particles grow mainly in the direction of the short rod axis, resulting in a decrease of the aspect ratio (Sect. 6.2). This is, to the best of my knowledge, the first real-time optical observation of nanoparticle growth on a single-particle level (results were published in Ref. Becker et al. 2007). In collaboration with Olaf Schubert the nanoparticle growth was also monitored using the novel RotPOL setup. Here a decrease of the average polarization anisotropy PA is observed (Sect. 6.3).

6.1 Introduction

Compared to the atomic level of control achievable in organic syntheses, the wet chemical production of nanoparticles often suffers from low yield and/or a relatively broad size and shape distribution. Circumventing the issue of inhomogeneous samples, microscopic techniques to study optical properties of individual nanoparticles have become a major characterization tool (Eustis and El-Sayed 2006). The origin of the inhomogeneous growth of nanoparticle samples and details of the growth mechanism are not well understood in most cases (Yin and Alivisatos 2005). The study of the particle growth process itself on a single-particle level has so far been limited, due to difficulties in obtaining enough statistics and due to technical complexity. Most studies rely on stopping the growth reaction at various points and determine particle morphology at aliquots taken at those times (Petroski et al. 1998; Peng and Peng 2002; Wei and Zamborini 2004; Agarwal et al. 2006; Festag et al. 2007).

The key for our optical study of nanoparticle growth on a single-particle level is the fact that the light-scattering spectra of gold nanorods depend delicately on size and shape of the particles (Sect. 2.5.1, (Nikoobakht and El-Sayed 2003; Murphy et al. 2005)). The scattering spectrum is dominated by the long axis plasmon resonance, which shifts towards longer wavelengths for higher aspect ratios (Link et al. 1999)

J. Becker, *Plasmons as Sensors*, Springer Theses,
DOI: 10.1007/978-3-642-31241-0_6, © Springer-Verlag Berlin Heidelberg 2012

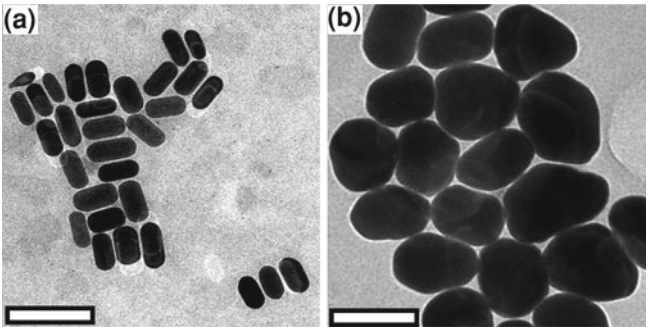

Fig. 6.1 **a** TEM image of original gold nanorod sample. **b** TEM image of the sample after 2.5 h incubation in growth solution in a batch experiment. The particles are considerably larger and more spherical. Scalebars are 100 nm [Image reprinted with permission of the American Chemical Society (Becker et al. 2007)]

and broadens for larger particles due to increased radiation damping (Sönnichsen et al. 2002). Hence, it is possible to deduce the particle size and shape by observing the resonance energy and linewidth of single particles, assuming the particles stay rodshaped and the particle environment stays the same. In other words, the "phase space" of particle shape (size and aspect ratio) maps bijective onto the experimentally observable "phase space" of linewidths and resonance energy (Prescott and Mulvaney 2006).

6.2 Investigation with the FastSPS Setup

Description of the Experiment

We use the fastSPS method (5.1) to investigate nanoparticle growth, specifically gold nanorods in a "growth solution" containing gold ions and surfactant molecules (Sect. 3.1). The interest in this system originates in the recent observation of a change in particle growth mode from one to three dimensional on particles grown in a continuous flow reactor (Boleininger et al. 2006). We first synthesize small gold nanorods in a batch synthesis (Sect. 3.1). Figure 6.1a shows a transmission electron microscope (TEM, Sect. 4.3) image of the rods used in this work. Statistical image analysis of 160 rods results in a mean length of 48 ± 4 nm, a mean width of 22 ± 3 nm, and a mean aspect ratio of 2.2 ± 0.3.

Batch Control Experiment

Before investigating single particles, we performed a batch control experiment by measuring the extinction of an ensemble (Sect. 4.1), diluting 50 µL of the above rod solution in 950 µL of CTAB (0.1M). After 10 min, we added 1000 µL of a double concentrated growth solution containing twice the amount of gold, silver, and ascorbic acid compared to the values given in Sect. 3.1 in order to get the normal

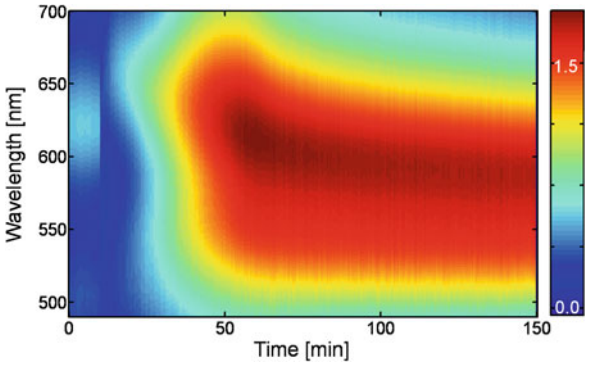

Fig. 6.2 Continuous ensemble extinction spectra (*color coded*) of previously grown gold nanorods. After 10 min, a growth solution is added to achieve a further nanoparticle growth. The peak shifts to smaller wavelengths and increases in intensity due to the nanoparticle growth process [Image reprinted with permission of the American Chemical Society (Becker et al. 2007)]

values in the final reaction mixture. After 2.5 h of incubation we take TEM images of the resulting particles (Fig. 6.1b). Statistical analysis of 160 particles yields a mean length of 97 ± 12 nm, a mean width of 73 ± 12 nm, and a mean aspect ratio of 1.4 ± 0.2. The extinction spectrum of the particles during the growth process is continuously monitored with a fiber spectrometer (Fig. 6.2) and shows a shift in peak extinction wavelength from 636 to 597 nm in the course of the reaction. This batch experiment is not directly comparable to particle growth near surfaces, but shows the general trend that we expect for particle growth under these conditions: mainly in the direction of the short axis.

Comparison Particles Before and After Growth

To investigate the growth on a single-particle level, we dilute the rod-solution 1:100 with distilled water and rinse them for 5 min through a flow-cell consisting of a thin, flat glass capillary (0.1 mm × 2 mm × 100 mm) connected to tubes made of polyethylene terephthalate (PET). Some of the rods stick to the glass surface, which is enhanced by addition of small amounts of sodium chloride. When enough rods are immobilized in the field of view, we rinse with pure CTAB (0.1 M) and measure the spectra of all particles in this field of view. About 20 of those particles are now continuously monitored in parallel for about 165 min every 30 s. We replace the pure CTAB rinsing solution after 10 min with a growth solution containing 1/10 of the values of gold, silver, and ascorbic acid given in Sect. 3.1 and rinse for about 2.5 h. The amount of gold ions in relation to the number of particles in the flow cell is chosen to match the batch experiment, which leads, however, to a slower reaction kinetics because of the lower absolute concentration. Figure 6.3 shows the full width at half-maximum (FWHM) of each spectrum against its resonance energy at the start of the experiment (triangles) as well as at the end (dots). Both, the resonance energy of the particles and the FWHM increases, confirming that the aspect ratio of the particles decreases and the overall size increases. The inset shows the full

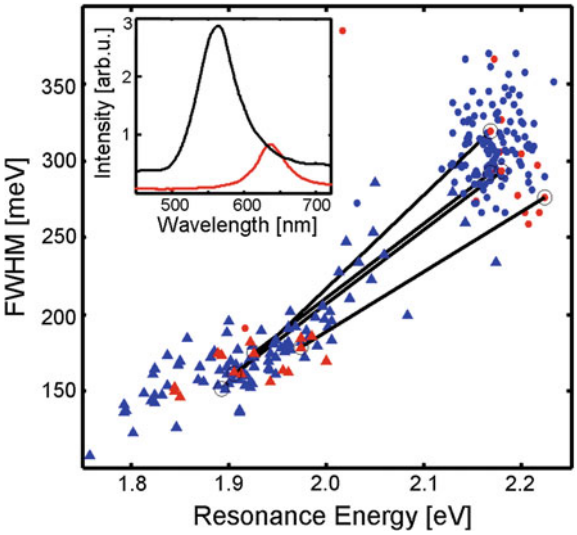

Fig. 6.3 Optical single-particle spectra of particles before *triangles* and after *dots* rinsing them with growth solution for about 180 min. For each spectrum, the full width at half-maximum (FWHM) is plotted against its resonance energy. The particles corresponding to the red markers are continuously measured. *Red dots* represent 16 of the particles investigated continuously during rinsing with growth solution. The inset shows an example of a single particle spectrum before *red* and after *black* rinsing with growth solution. The increase of absolute intensity is caused by the increased particle volume [Image reprinted with permission of the American Chemical Society (Becker et al. 2007)]

spectra of one single particle before (red) and after (black) rinsing with the growth solution, where we see, in addition to the shifts in linewidth and resonance energy, a considerable increase in peak intensity, which is discussed below.

Continuous Investigation of Particles during Growth Process

The fastSPS setup allows to investigate up 20 particles continuously in parallel. For one of the 20 particles observed continuously, the resulting spectra are shown (color coded) as a function of time in Fig. 6.4a. Figure 6.4b shows the development of the FWHM of the same article (left axis) and the (integrated) scattered light intensity (right axis).

Initially, there is a constant period where the particles are incubated in pure CTAB solution. A small step-like change in the FWHM and intensity occurs at the start of the rinsing process, a phenomenon previously observed (Sönnichsen et al. 2005) and currently unexplained. During rinsing with growth solution, the FWHM increases nearly linear over time (the steps after about 28, 58, and 127 min are due to refocusing). The intensity of the scattered light integrated over all wavelengths (I_{sca}) increases strongly over time. Because I_{sca} scales, in general, with the square of the particle volume (Sect. 2.2), the increase shows the overall particle growth. The scaling of I_{sca} with the square of the particle volume is, however, not strictly applicable for plasmon resonant particles, because a shift in resonance energy and/or the amount

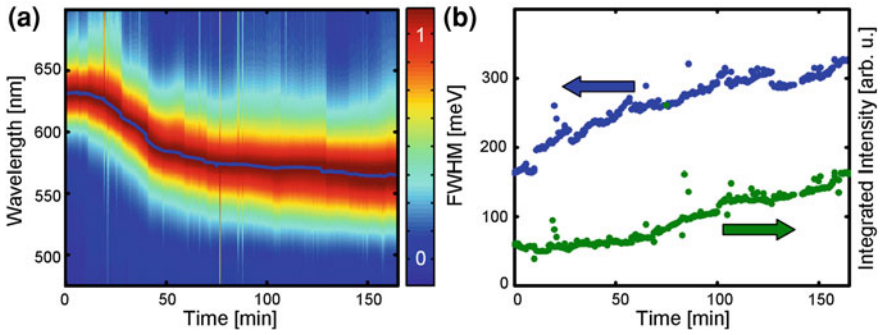

Fig. 6.4 **a** Normalized scattering spectra of one single particle during rinsing with growth solution shown color-coded as a function of time. During the first 10 min, the particle is incubated in pure CTAB solution (0.1 M). For the same measurement, the time development of the FWHM *blue dots* and the integral of intensity over the wavelengths *green dots* are shown in **b** [Image reprinted with permission of the American Chemical Society (Becker et al. 2007)]

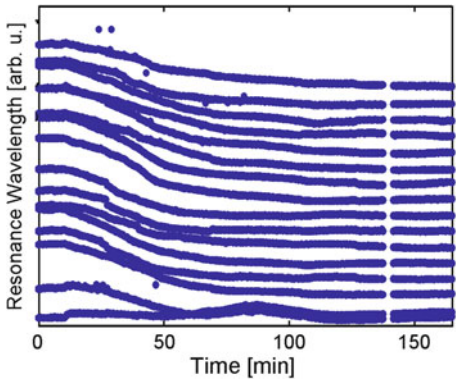

Fig. 6.5 The resonance wavelength of 16 particles from one experimental run (arbitrary offset) decreases as a function of time for 14 particles *upper lines*, while it stays nearly constant for two particles. The gap after 140 min is due to refocusing [Image reprinted with permission of the American Chemical Society (Becker et al. 2007)]

of damping may also have some effect (Sönnichsen et al. 2002; Novo et al. 2006). Figure 6.5 shows the development of the resonance wavelength of 16 particles investigated in parallel during rinsing with growth solution (four particles turned out to be useless for analysis, for example, due to a dust particle setting down nearby during observation).

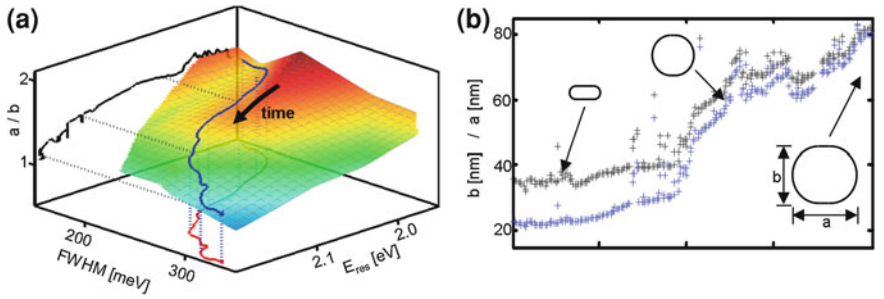

Fig. 6.6 **a** The particle geometry (given by the long and short axes a and b, or the aspect ratio a/b and the volume V) are related to the measured spectral quantities resonance position (E_{res}) and linewidth (FWHM) by a bijective function F (shown as colored surface area). The function F was calculated by interpolation between values obtained by DDA simulations and Mie calculations. We have indicated a measured trajectory of E_{res} and the FWHM *red line* and the corresponding trajectory of the aspect ratio *blue line*. **b** Time development of the long *black*/short *blue* axis of one single nanorod as a function of time (respectively) as determined by the function F. The insets indicate the size of the rod at three moments in time [Image reprinted with permission of the American Chemical Society (Becker et al. 2007)]

6.2.1 Comparison Experimental of Data with Theory

The measured optical scattering spectra of individual particles allow the direct deduction of particle size and shape. The particle shape is either described by the particle aspect ratio (a/b) and volume (V), or the dimensions of the particle's long (a) and short axis (b). In principle, the plasmon resonance position E_{res} and its linewidth (FWHM) of a particle with a given geometry (e.g., cylindrical) and embedded in a given environment is directly connected with the geometrical parameters a and b (or a/b and V) via a bijective function $F: a, b \leftrightarrow E_{\mathrm{res}}$, FWHM converting optically measured values into particle sizes. This function F can be calculated solving Maxwell's equations either analytically, e.g., using Mie's equations (for spherical particles, see Sect. 2.3) or numerically, for example by the method of discrete dipoles approximation (DDA, Sect. 2.4.1). We use a combination of values from Mie theory and DDA simulations obtained with the software DDSCAT 6.1 (Draine and Flatau 2004). Our DDSCAT calculations were performed with dipole distances of 2 nm using a spherically capped cylinder as particle shape. For all calculations, we use the values for the dielectric function of gold as provided by (Johnson and Christy 1972) Fig. 8.6). The resulting form of the function F is shown in part in Fig. 6.6a in a three-dimensional plot. We also indicate the trajectory of one particle in this space. The resulting particle geometry evolution is shown in Fig. 6.6b. Because the measured spectral linewidth is very sensitive to defocusing, the resulting particle geometry data are relatively noisy and show jumps at points in time where we refocused.

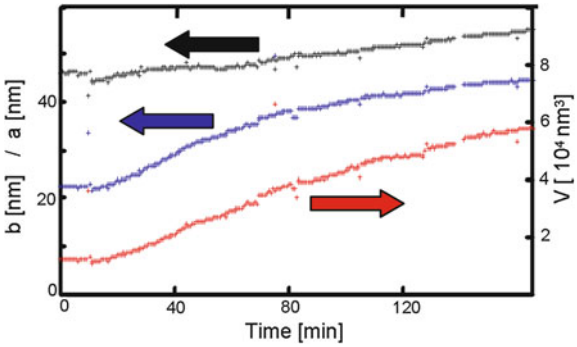

Fig. 6.7 Average shape development of 12 particles calculated from E_{res} and the measured scattering intensity I_{sca} by the simplified function G [Image reprinted with permission of the American Chemical Society (Becker et al. 2007)]

Using the Scattered Light Intensity as Parameter

An alternative to the method used above is the use of the scattered light intensity I_{sca} (at the maximum) as the second experimental parameter instead of the FWHM. The time dependence of I_{sca} is easily extracted from the measured data and shows a stronger increase over the course of the particle growth than the FWHM. The conversion of E_{res} and I_{sca} into particle size parameters a/b and V requires, however, the a priori knowledge of the initial particle size V_0. We use the average value of V_0, determined from TEM images (Fig. 6.1a), as an approximation. By taking only the dependency of E_{res} on a/b into account, a/b is calculated by the empirically (Link et al. 2005) derived formula $1240\,eV/E_{\mathrm{res}} = (53.71\,a/b - 42.29)\epsilon_m + 495.14$ with the dielectric permittivity of the surrounding medium $\epsilon_m = (1.33)^2$. The relationship of V to I_{sca} and E_{res} follows from $I_{\mathrm{sca}} \propto \lambda^{-4}\,|\alpha|^2$ (Eq. 2.2) with the complex polarizability α (Bohren and Huffman 1983). Using the quasistatic approximation to calculate R for ellipsoidal particles, we obtain for the intensity at the resonance wavelength λ_{res}) (real part of the denominator of α diminishes: $1 + L_a(\epsilon'_{\mathrm{r}}) = 0$, Eq. 2.2):

$$I(\lambda_{\mathrm{res}}) \propto \frac{1}{\lambda_{\mathrm{res}}^4}\left|\frac{\epsilon'_{\mathrm{r}} + i\epsilon''_{\mathrm{r}} + 1}{i\epsilon''_{\mathrm{r}}}\right|^2 \cdot \frac{V^2}{L_{\mathrm{a}}^2} \tag{6.1}$$

with:

$\epsilon_{\mathrm{r}} = \epsilon_{\mathrm{metal}}/\epsilon_{\mathrm{medium}} = \epsilon'_{\mathrm{r}} + i\epsilon''_{\mathrm{r}}$: complex relative dielectric permittivity
$L_{\mathrm{a}} \approx (1 + a/b)^{-1.6}$: shape parameter of the long axis (Sönnichsen 2001)

The development of the particle geometry of 12 individual particles is derived from I_{sca} and E_{res}. The mean of these results are shown in Fig. 6.7.

Therefore regardless of the method used to derive the particle size development, a faster growth of the short axis compared to the long particle axis is evident (Figs. 6.6b and 6.7). Even though the derivation of particle sizes using the linewidth is theoreti-

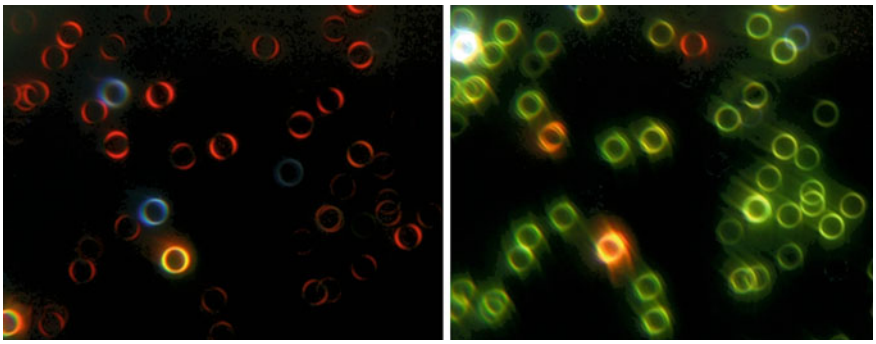

Fig. 6.8 In situ particle growth observation of gold nanorods exposed to a growth solution using the RotPOL setup with a consumer digital camera. Starting with rod-shaped nanoparticles with light scattering mostly in the *red* (*left panel*), the resonance wavelength decreases over time until the particles scatter light mostly in the *green* (*right panel*) [Image reprinted with permission of the American Chemical Society (Schubert et al. 2008)]

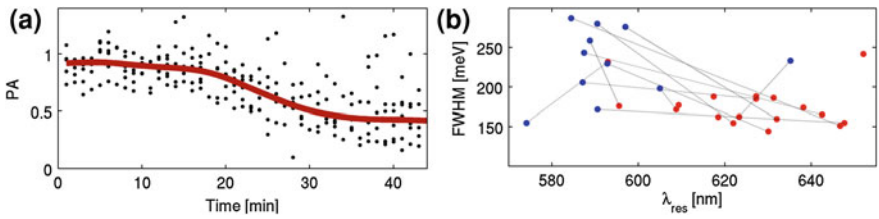

Fig. 6.9 **a** The initial rod-shaped nanoparticles have a high degree of polarization anisotropy PA which decreases over time due to the additional growth until nearly all particles show a much lower anisotropy. The *red line* is an average over six particles. Before and after the growth process, detailed polarization-dependent scattering spectra $I(\lambda, \theta)$ are obtained. **b** The linewidth FWHM and resonance wavelength λ_{res} extracted from these measurements are shown in (*red dots* at start of growth process, *blue dots* afterward). *Dashed lines* connect dots corresponding to the same particle. For most particles, the resonance wavelength decreases and the linewidth increases. The decrease of polarization anisotropy over time, the simultaneous decrease in resonance wavelength, and the increase in linewidth suggest that the rod-shaped particles grow mainly along the short axis, resulting in particles that are more spherical [Image reprinted with permission of the American Chemical Society (Schubert et al. 2008)]

cally more elegant, the current limitations in the experimental accuracy favors the use of the second method, the derivation from the measured scattering intensity, and the resonance energy. The mean over several simultaneously measured particles shown in Fig. 6.7 is an accurate description of the growth behavior of gold nanorods in the given environment. The volume increases linearly over time with a rate of about $5\,\mathrm{nm}^3/\mathrm{s}$, which is comparable to the rate expected from diffusion-limited growth. Thus, diffusion or mass transport limits the reaction in our case. Knowing the growth kinetics and the limiting step of the reaction will be useful for controlled particle growths on surfaces and in solution.

6.3 Polarization Anisotropy Investigation with RotPOL Setup

The growth of 18 gold nanorods immobilized in a glass flow cell is monitored using the RotPOL setup (Sect. 5.2) combined with a digital consumer camera, which is adjusted with a time resolution of 60 s. While the initial rodshaped particles scatter mostly red light their resonance is changed into the green (Fig. 6.8) due to the decrease of the aspect ratio. With the RotPOL setup a decrease of the average polarization anisotropy (PA) over time from 0.9 to 0.4 within 43 min can be observed (Fig. 6.9). This decrease of PA is consistent with the decrease of aspect ratio for gold rods exposed to a growth solution due to the preferential growth in width we observed before (Chap. 6). To confirm the preferential growth in width, full polarization dependent scattering spectra $I(\lambda, \theta)$ were recorded before and after the growth-process for a subset of 16 particles. A shift of the resonance wavelength to lower wavelengths and an increase in linewidth is observed for most particles as expected for larger, rounder nanoparticles.

6.4 Conclusions

The optical investigation of particle growth in real time provides insight into the second part of gold nanorod synthesis, where particle growth is preferentially into the direction of the short axis, yielding more and more spherical particles. By converting the measured single-particle spectra into particle geometry using a theoretically derived transfer function, we deduce absolute values for particle geometry at each point in time. These values will provide basic input data to compare quantitatively theoretical models of nanoparticle growth.

References

Agarwal, V., Aruna, I., Banerjee, V., & Mehta, B. R. (2006). Growth of palladium nanoparticles: An experimental and numerical study. *Physical Review B, 74*(3), 035412.

Becker, J., Schubert, O., & Sönnichsen, C. (2007). Gold nanoparticle growth monitored in situ using a novel fast optical single-particle spectroscopy method. *Nano Letters, 7*(6), 1664–1669.

Bohren, C., & Huffman, D. R. (1983). *Absorption and Scattering of Light by Small Particles*. New York: Wiley-Interscience.

Boleininger, J., Kurz, A., Reuss, V., & Sönnichsen, C. (2006). Microfluidic continuous flow synthesis of rod-shaped gold and silver nanocrystals. *Physical Chemistry Chemical Physics, 8*(33), 3824–3827.

Draine, B. and Flatau, P. (2004). User guide to the discrete dipole approximation code ddscat 6.1. http://arxiv.org/abs/astro-ph/0409262v2

Eustis, S., & El-Sayed, M. A. (2006). Why gold nanoparticles are more precious than pretty gold: Noble metal surface plasmon resonance and its enhancement of the radiative and nonradiative properties of nanocrystals of different shapes. *Chemical Society Reviews, 35*(3), 209–217.

Festag, G., Steinbrueck, A., Csaki, A., Moeller, R., & Fritzsche, W. (2007). Single particle studies of the autocatalytic metal deposition onto surface-bound gold nanoparticles reveal a linear growth. *Nanotechnology, 18*(1), 015502.

Johnson, P., & Christy, R. (1972). Optical constants of the noble metals. *Physical Review B, 6*(12), 4370–4379.

Link, S., Mohamed, M. B., & El-Sayed, M. A. (1999). Simulation of the optical absorption spectra of gold nanorods as a function of their aspect ratio and the effect of the medium dielectric constant. *Journal of Physical Chemistry B, 103*(16), 3073–3077.

Link, S., El-Sayed, M. A., & Mohamed, M. B. (2005). Simulation of the optical absorption spectra of gold nanorods as a function of their aspect ratio and the effect of the medium dielectric constant (vol 103b, p. 3073, 1999). *Journal of Physical Chemistry B, 109*(20), 10531–10532.

Murphy, C. J., San, T. K., Gole, A. M., Orendorff, C. J., Gao, J. X., Gou, L., et al. (2005). Anisotropic metal nanoparticles: Synthesis, assembly, and optical applications. *Journal of Physical Chemistry B, 109*(29), 13857–13870.

Nikoobakht, B., & El-Sayed, M. A. (2003). Preparation and growth mechanism of gold nanorods (nrs) using seed-mediated growth method. *Chemistry of Materials, 15*(10), 1957–1962.

Novo, C., Gomez, D., Perez-Juste, J., Zhang, Z. Y., Petrova, H., Reismann, M., et al. (2006). Contributions from radiation damping and surface scattering to the linewidth of the longitudinal plasmon band of gold nanorods: a single particle study. *Physical Chemistry Chemical Physics, 8*(30), 3540–3546.

Peng, Z. A., & Peng, X. G. (2002). Nearly monodisperse and shape-controlled cdse nanocrystals via alternative routes: Nucleation and growth. *Journal of the American Chemical Society, 124*(13), 3343–3353.

Petroski, J. M., Wang, Z. L., Green, T. C., & El-Sayed, M. A. (1998). Kinetically controlled growth and shape formation mechanism of platinum nanoparticles. *Journal of Physical Chemistry B, 102*(18), 3316–3320.

Prescott, S. W., & Mulvaney, P. (2006). Gold nanorod extinction spectra. *Journal of Applied Physics, 99*(12), 123504.

Schubert, O., Becker, J., Carbone, L., Khalavka, Y., Provalska, T., Zins, I., et al. (2008). Mapping the polarization pattern of plasmon modes reveals nanoparticle symmetry. *Nano Letters, 8*(8), 2345–2350.

Sönnichsen, C. (2001). *Plasmons in metal nanostructures*. München: Cuvillier Verlag Göttingen.

Sönnichsen, C., Franzl, T., Wilk, T., von Plessen, G., Feldmann, J., Wilson, O., et al. (2002). Drastic reduction of plasmon damping in gold nanorods. *Physical Review Letters, 88*(7), 077402.

Sönnichsen, C., Reinhard, B. M., Liphardt, J., & Alivisatos, A. P. (2005). A molecular ruler based on plasmon coupling of single gold and silver nanoparticles. *Nature Biotechnology, 23*(6), 741–745.

Wei, Z. Q., & Zamborini, F. P. (2004). Directly monitoring the growth of gold nanoparticle seeds into gold nanorods. *Langmuir, 20*(26), 11301–11304.

Yin, Y., & Alivisatos, A. P. (2005). Colloidal nanocrystal synthesis and the organic-inorganic interface. *Nature, 437*(7059), 664–670.

Chapter 7
Protein-Membrane Interaction

In the following chapter I present a nanosized and addressable protein sensor platform based on membrane coated plasmonic particles. I show unequivocally the covering of gold nanorods with lipid bilayers and thereafter the subsequent detection of streptavidin binding to biotin moities in the lipids. The binding of the streptavidin on the membrane covered gold nanorods is detected by monitoring the spectral shift by fast single particle spectroscopy (fastSPS) on many particles in parallel. This approach allows for local analysis of protein interaction with biological membranes as a function of the lateral composition of phase separated membranes. In Sect. 7.2 I describe the preparation of the large unilamellar vesicles and accompanying fluorescence recovery after photo-bleaching (FRAP) and ellipsometry measurements, which were performed by my collaboration partner Baciu from the group of Janshoff. The investigation of the binding process on single particle level is described in Sect. 7.3, while Sect. 7.4 discusses the influence of a small spacer between the biotin and the membrane on the spectral shifts. The results of these investigations are published in Ref. Baciu et al. (2008).

7.1 Introduction

The detection of non-covalent binding events is a fundamental goal of contemporary bio-analytical chemistry, for example in high throughput screening (HTS) of drug candidates from large libraries of molecules that potentially recognize a specific surface receptor. HTS heavily relies on sophisticated strategies to miniaturize the devices, in particular the sensing area. However, miniaturization is ultimately limited by the increasing stochastic noise emitted by the small area, which eventually exceeds the actual sensor signal. This small-area regime, however, renders conventional analysis of surface binding cumbersome due to decreasing signal to noise ratios. Often overlooked is the fact that the noise produced in small systems comprises valuable information about all involved rate constants as produced by equi-

J. Becker, *Plasmons as Sensors*, Springer Theses,
DOI: 10.1007/978-3-642-31241-0_7, © Springer-Verlag Berlin Heidelberg 2012

librium coverage fluctuations (Luthgens and Janshoff 2005). It is in principle possible to extract relevant kinetic parameters from a system that is inherently in equilibrium without interference with mass transport as often faced in diluted systems. Small sensing areas are required to exploit the noise generated by coverage fluctuations and this work deals with the necessary requirements of the next generation of stochastic sensing on surfaces. Single gold nanoparticles can be used as sensors for their local environment by detecting the plasmon shift induced by changes in the refractive index (Chap. 8, (Sönnichsen et al. 2000; Raschke et al. 2003; Nusz et al. 2008; McFarland and Van Duyne 2003)). Motivation for single particle based detection of membrane protein interaction is also provided by contemporary research on the lateral organization of biological membranes (Rajendran and Simons 2005). Particularly, elucidation of occurrence and function of nanodomains (also termed rafts) that are required for general membrane function is a challenging target for the proposed detection scheme based on membrane coated particles (Yethiraj and Weisshaar 2007). Employing particles as nanoscopic reporters for biomolecular interactions on the level of few (< 50) proteins offers the possibility to screen lateral inhomogeneities of native membranes.

Proper functionalization remains an issue if it comes to real world applications; in particular biological relevant samples such as membrane associated proteins and peptides. In this context, membrane mimics are an attractive solution to achieve an almost native environment with high surface coverage and miniscule non-specific adsorption. Solid supported membranes are among the most versatile sensing platforms to study both. Molecular recognition events usually taking place at cellular membranes and ionic transport across bilayers (Janshoff and Steinem 2006). A large variety of different model systems have been successfully established and the approaches range from simple self-assembled lipid bilayers on various supports such as glass, metal electrodes or semiconductors (Tanaka and Sackmann 2005). Lately, more advanced systems were created employing porous supports or using tethered lipids that allow functional insertion of membrane proteins (Schmitt et al. 2008). Only few studies report on particles successfully covered with lipid bilayers (Mornet et al. 2005; Roiter et al. 2008). This is mostly because parameters such as membrane curvature and adhesion properties need to be carefully adjusted.

7.2 Sensor Platform Based on Gold Nanorods

We create a sensor platform based on individual gold nanorods immobilized randomly on a solid support and covered entirely with a fluid membrane displaying biotin moieties (Fig. 7.1). The gold nanorods we use are synthesized using the procedure described in Sect. 3.1 and have a mean length of 56 ± 5 nm, a mean width of 26 ± 5 nm, and a mean aspect ratio of 2.2 ± 0.4 nm as determined from measuring 100 particles on TEM (Sect. 4.3) images (Fig. 7.2a).

The fluorescently labeled (BodiPY-PC) membrane is formed by vesicle spreading (Mayer et al. 1986). The homogeneous green fluorescence from the membrane,

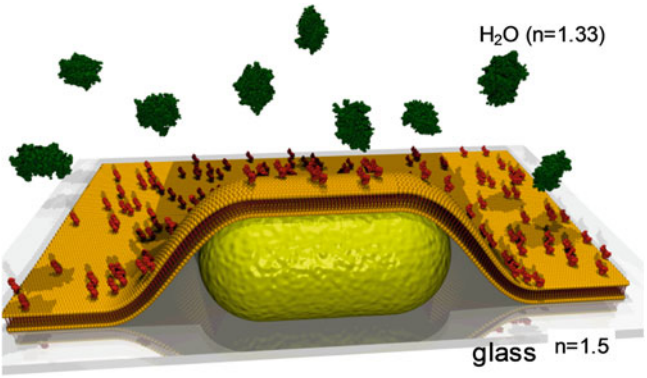

Fig. 7.1 Schematics of a gold nanorod (*yellow*) coated with a partly biotinylated (*red*) membrane (*orange*) and exposed to streptavidin (*green*). The scheme presents the ideal case of a complete membrane coverage without any defects. The glass support has a refractive index of n = 1.5, the aqueous buffer of n = 1.33 [Image reprinted with permission of the American Chemical Society (Baciu et al. 2008)]

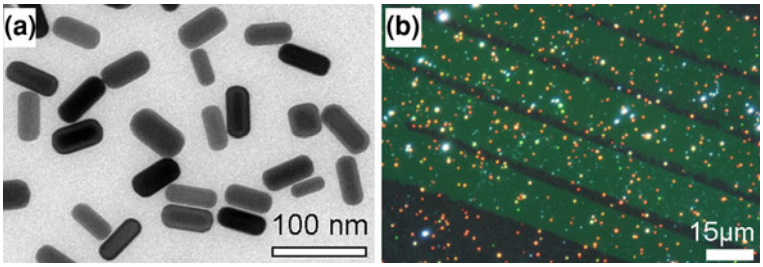

Fig. 7.2 **a** Transmission electron microscope (TEM) image of gold nanorods used in this work (mean length 56 ± 5 nm, width 26 ± 5 nm, aspect ratio 2.2 ± 0.4 nm, determined from 100 particles). **b** Darkfield image of gold nanorods (*bright spots*) covered by a lipid membrane. The membrane (*greenish background*) is structured on this substrate by a micromolding in capillaries (Janshoff and Kunneke 2000) [Image reprinted with permission of the American Chemical Society (Baciu et al. 2008)]

visible directly under white light dark-field illumination, shows successful spreading of a closed lipid bilayer (Fig. 7.2b). The gold nanorods appear as brightly colored spots under dark-field illumination, due to the excitation of plasmons at their specific plasmon resonance wavelength.

7.2.1 Creation of Lipid Membranes on Substrates

Large unilamellar vesicles (LUVs) where produced by Christina Baciu, who composed the desired lipid mixtures including low concentration (1 mol%) of fluorescent probe molecules are prepared by extrusion method and used to form supported

lipid bilayers. The lipids are mixed in methanol/chloroform (3:1 v/v) and then dried under nitrogen stream followed by desiccation for 3 h in vacuum to remove remaining organic solvent. The resulted lipid films are hydrated in buffer (20 mM Tris/HCl, 100 mM NaCl, pH 7.4) for about 15 min and the lipid suspension is then vortexed five times for 20 s every 5 min to form multilamellar vesicles that are afterwards extruded 31 times through a polycarbonate membrane (100 nm pore diameter) by using a LiposoFast miniextruder (Avestin, Ottawa, Canada). In this way LUVs vesicles are formed at a final concentration of 0.5 mg/ml. Individually addressable micropatterned solid supported lipid bilayers are achieved by flowing LUVs through the capillaries formed by conformal contact with the glass substrate. The thickness of the membrane was measured by Christina Baciu by ellipsometry and was determined as 3.95 nm.

Some fraction (2−10 mol%) of the lipids in the membrane could be labeled with biotinylated lipids (Biotin-DHPE or Biotin-X-DHPE), sufficient to produce a complete streptavidin monolayer on top of the membrane. The streptavidin layer revealed an additional height increase of 2.34 nm for the Biotin-DHPE and 3.12 nm for the Biotin-X-DHPE membrane.

7.3 FastSPS Measurements

We are able to detect streptavidin binding to several membrane coated gold nanorods in parallel using the fast single particle spectroscopy (fastSPS) setup (see Sect. 5.1).

7.3.1 Experimental and Measurement Procedure

To immobilize gold nanorods on a glass substrate, we dilute the as prepared rod-solution 1:10 with distilled water and rinse them for 5 min. through a flow-cell consisting of a thin, flat glass capillary (0.1 mm × 2 mm × 100 mm) connected to PET tubing. Some of the rods stick to the glass surface, which is enhanced by addition of a small amount of sodium chloride. When enough rods are immobilized in the field of view, we rinse with distilled water for 30 min to remove unbound rods and surfactant from the growth-solution. Subsequently, the sample is rinsed with PBS buffer for additional 5 min to ensure that the gold particles are in the same environment in all of the following measurements. At this point, we record the spectra of 29 particles in the field of view. Each particle is investigated five times to get statistics and enhance the accuracy of the mean.

In order to spread a membrane on the substrate, we flush in lipid vesicles and incubate for 30 min. Subsequent washing with PBS buffer for 60 min removes excess lipid vesicles. BodiPy-fluorescence from markers in the lipids (1 mole%) is used to ensure that the glass surface in the field of view is indeed covered by a membrane. The illumination light bleaches fluorescence after some minutes simplifying subsequent measurements by removing unwanted light from fluorescence dyes. Spectra

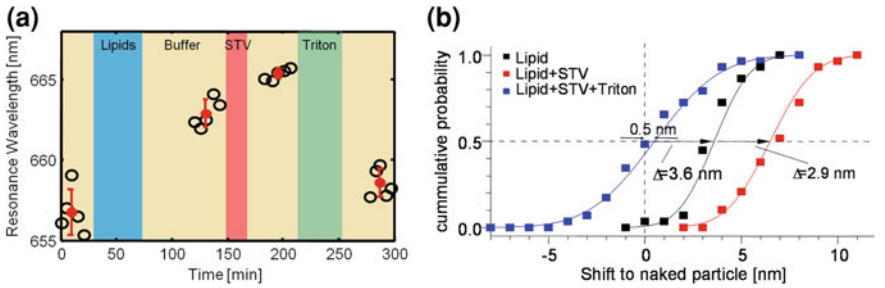

Fig. 7.3 **a** The resonance wavelengths extracted from single particle spectra of one individual particle measured over the course of the experiment (*black circles*, mean in *red* with standard deviations). Shadings indicate the experimental steps: initially naked, then covered by a biotinylated membrane, followed by a layer of streptavidin, and finally after washing with Triton x-100 to remove the entire membrane coating. **b** Cumulative probability of spectral shifts derived from observing 29 particles parallel to the particle in **b**. We observe a median shift of $\Delta_m = 3.6 \pm 1.5$ nm (*black dots*) after covering the particles with a membrane. Addition of streptavidin leads to a second shift of $\Delta_s = 2.9 \pm 1.8$ nm. After rinsing with protease and Triton x-100 (to remove the proteins and the membrane), the resonance wavelength is $\Delta_t = 0.5 \pm 2.7$ nm shifted compared to the beginning of the experiment. The *solid lines* show the cumulative probability for a Gaussian distribution with the listed median values and standard deviations [Image reprinted with permission of the American Chemical Society (Baciu et al. 2008)]

of the 29 particles previously investigated are recorded again at this point five times consecutively (Fig. 7.3a shows the resulting resonance wavelength for one particle as a function of experimental time elapsed). To bind streptavidin to the biotinylated membrane, we rinse with a solution containing 1 mg/mL streptavidin in the identical buffer solution and incubate for 20 min. Unbound streptavidin is removed by rinsing for another 20 min with pure buffer and the particle spectra are measured again. In the next step, we remove the streptavidin layer with protease (Protease from *Streptomyces griseus*, Sigma Aldrich: P8811, 2 mg/mL). The protease causes a white precipitate and thus an enormous increase of the scattering background making a direct spectral investigation of single nanoparticles impossible. Therefore, we wash with a cleaning solution (Triton x-100, 4 % (v/v)) for 10 min to remove the proteins and the membrane and rinse for 10 min with buffer. At this point, the final spectra of the 29 particles monitored in this experiment are measured.Fig. 7.3a shows the single particle scattering spectra for a typical gold rod used in the experiments. Initially, the particle is immersed in buffer and has a resonance wavelength of 656.8 ± 1.4 nm (the error quoted is the standard deviation from five independent measurements). Spreading the membrane on the substrate over the particles results in a red-shifted resonance at 662.9 ± 0.9 nm—a shift of 6.1 nm to the initial value. Addition of streptavidin to the system further increases the resonance wavelength to 665.4 ± 0.3 nm, i.e. an additional shift of 2.5 nm, presumably due to a layer of streptavidin on the membrane. Removing the streptavidin and the membrane by protease and Triton x-100 shifts the spectrum back to 658.6 ± 0.9 nm, only 1.8 nm higher than the initial resonance wavelength.

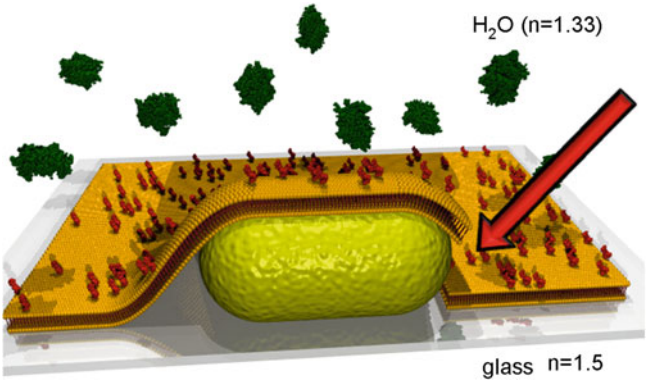

Fig. 7.4 Schematics of a gold nanorod (*yellow*) coated with a partly biotinylated (*red*) membrane (*orange*) and exposed to streptavidin (*green*). In contrast to Fig. 7.1 the scheme here presents the case of a incomplete membrane coverage (see *red arrow*) which can lead to a non-specific binding of streptavidin to the rod surface

7.3.2 Statistics

The same data as above is available for 29 particles analyzed in parallel during the same experiment. Considering all 29 particles, we observe a median shift of 3.6 ± 0.3 nm due to spreading the membrane and a second shift of 2.9 ± 0.3 nm because of the binding of streptavidin to the membrane. After removing both layers, the resonance wavelength shifts 0.5 ± 0.5 nm compared to the beginning of the experiment (Fig. 7.3b). Repeated experiments under similar conditions show shifts due to spreading of the membrane between 3.5 and 5.4 nm , depending on lipid-concentration and incubation time. Furthermore, we perform a control experiment with lipids containing no biotin. Here, the incubation with streptavidin results in a negligible shift of 0.6 ± 0.3 nm. This small shift may be a sign that not all rods are completely membrane covered (Roiter et al. 2008) and streptavidin attaches non-specifically to their surface (Fig. 7.4). Perfectly wrapping of particles as envisioned in Fig. 7.1 is governed by the interplay of membrane adhesion to both the particle as well as the glass surface with curvature energy required to bend the membrane at the boundary. The exact shape of the membrane is therefore a function of adhesion energy, particle size, and phospholipid structure.

7.3.3 Comparison with Theory

In order to compare our experimental findings with theory, we estimate the plasmon shifts using the quasi-static approximation (Sect. 2.2) for rods with spherical shaped endcaps (Liu and Guyot-Sionnest, 2004; Prescott and Mulvaney, 2006). This theory

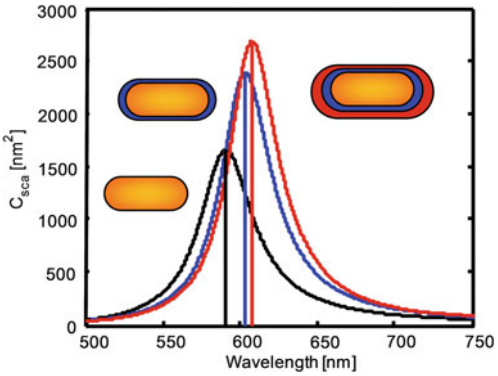

Fig. 7.5 Theoretical scattering spectra based on the quasi-static approximation for rods with spherical endcap geometry. While bare gold spheroids with a size of 56 × 26 nm show a resonance wavelength of 622.1 nm (*black line*), the same rod coated with a 3.95 nm thick shell with a refractive index of n = 1.5 shows a resonance wavelength of 637.3 nm (*blue line*). Increasing the shell thickness by additional 2.34 nm shifts the resonance wavelength further to 643.0 nm (*red line*) [Image reprinted with permission of the American Chemical Society (Baciu et al. 2008)]

neglects the effects of particle volume and glass substrate. Within this approximation, a 'naked' rod of 56 × 26 nm size and immersed in water, has a resonance wavelength of 622.1 nm. For the same particle surrounded by a shell corresponding to the membrane thickness (3.95 nm) with a refractive index of $n = 1.5$, the resonance wavelength shifts by 15.2 nm. Increasing the shell-thickness to 6.29 nm (3.95 nm thickness of the membrane plus 2.34 nm for streptavidin) leads to a second shift of 5.8 nm (Fig. 7.5). The theoretically predicted shifts are therefore 2−4 x larger than the experimental results. Since the calculations above assume a completely coated rod but in the experiments, the rods touch the membrane only on one side (Fig. 7.1), a smaller shift in the experiment is reasonable. Another reason for the smaller measured shift can be due to a smaller refractive index of the membrane and the streptavidin then the assumed one ($n = 1.5$).

7.4 Influence of a Small Spacer in the Membrane

Furthermore, I test whether the sensitivity of the plasmon shift is sufficient to determine the influence of a small spacer connecting the biotin to the lipid head group. For this purpose, three identical experiments as described above are performed with the only difference in the composition of the lipids: (I) with biotin directly connected to the lipid head-group (Biotin-DHPE), (II) with biotin attached via a short C_6 spacer (Biotin-X-DHPE), and (III) a control experiment with no biotin at all. Figure 7.6 shows the cumulative probabilities for finding plasmon shifts in the three cases. The median shift due to attaching streptavidin is 5.3 ± 0.7 nm for membrane containing

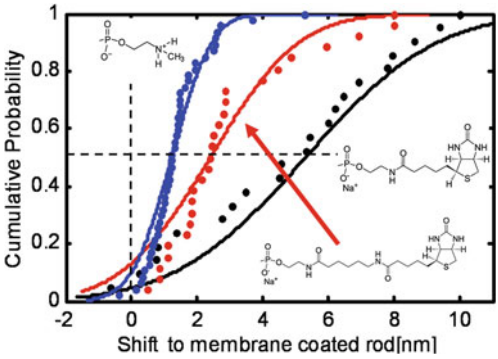

Fig. 7.6 Cumulative probability of the spectral shifts due to attachment of streptavidin to gold nanorods coated with different lipids. Attaching streptavidin to rods coated with lipids including biotin leads to a shift of $\Delta_s = 5.3 \pm 3.1$ nm (*block dots*). Using instead lipids with biotin including a spacer the spectral shift is smaller and results in $\Delta_s = 2.4 \pm 2.1$ nm (*red dots*). A lipid without any biotin leads to a small shift of $\Delta_s = 1.2 \pm 1.0$ nm due to a nonspecific binding to the gold rod surface (*blue dots*). The solid lines show the cumulative probability for a Gaussian distribution with the listed median values and standard-deviations [Image reprinted with permission of the American Chemical Society Baciu et al. (2008)]

biotin without a spacer, 2.4 ± 0.4 nm for the membrane with a spacer between the membrane and the biotin, and only 1.2 ± 0.1 nm for the membrane without any biotin. Attaching the streptavidin to membrane via a short linker results therefore in a smaller spectral shift, due to the increased separation compared to the direct linking. This can be explained by the well known decay in plasmon sensitivity with distance from the nanoparticle surface.

7.5 Conclusion

Membrane coated plasmonic nanoparticles provide a sensing platform that combines single particle sensing with a perfectly functionalized native coating. In this way, nanoparticles can serve as reporters for cellular reactions taking place on and within biological membranes. Lateral heterogeneity of cellular membranes can be probed with nanometer resolution employing monoclonal antibodies to detect small lipid domains or protein clusters on the membrane surface. Furthermore, membrane coated particles offer the advantage to suppress unwanted non-specific interactions due to the presence of the membrane, while providing an extremely small active area. Hence, it will be conceivable to create sensors based on the detection of equilibrium coverage fluctuations that would circumvent problems arising from mass transport and drift of the sensor signal. As a consequence, complex processes such as cooperative adsorption, adsorption to heterogeneous surfaces and slowly evolving systems could be addressed by fluctuation analysis.

References

Baciu, C., Becker, J., Janshoff, A., & Sönnichsen, C. (2008). Proteinmembrane interaction probed by single plasmonic nanoparticles. *Nano Letters, 8*(6), 1724–1728.

Janshoff, A., & Kunneke, S. (2000). Micropatterned solid-supported membranes formed by micromolding in capillaries. *European Biophysics Journal with Biophysics Letters, 29*(7), 549–554.

Janshoff, A., & Steinem, C. (2006). Transport across artificial membranes—an analytical perspective. *Analytical and Bioanalytical Chemistry, 385*(3), 433.

Liu, M. Z., & Guyot-Sionnest, P. (2004). Synthesis and optical characterization of au/ag core/shell nanorods. *Journal of Physical Chemistry B, 108*(19), 5882–5888.

Luthgens, E., & Janshoff, A. (2005). Equilibrium coverage fluctuations: A new approach to quantify reversible adsorption of proteins. *Chemphyschem, 6*(3), 444–448.

Mayer, L. D., Hope, M. J., & Cullis, P. R. (1986). Vesicles of variable sizes produced by a rapid extrusion procedure. *Biochimica Et Biophysica Acta, 858*(1), 161–168.

McFarland, A. D., & Van Duyne, R. P. (2003). Single silver nanoparticles as real-time optical sensors with zeptomole sensitivity. *Nano Letters, 3*(8), 1057–1062.

Mornet, S., Lambert, O., Duguet, E., & Brisson, A. (2005). The formation of supported lipid bilayers on silica nanoparticles revealed by cryoelectron microscopy. *Nano Letters, 5*(2), 281–285.

Nusz, G. J., Marinakos, S. M., Curry, A. C., Dahlin, A., Hook, F., Wax, A., et al. (2008). Label-free plasmonic detection of biomolecular binding by a single gold nanorod. *Analytical Chemistry, 80*(4), 984–989.

Prescott, S. W., & Mulvaney, P. (2006). Gold nanorod extinction spectra. *Journal of Applied Physics, 99*(12), 123504.

Rajendran, L., & Simons, K. (2005). Lipid rafts and membrane dynamics. *Journal of Cell Science, 118*(6), 1099–1102.

Raschke, G., Kowarik, S., Franzl, T., Sönnichsen, C., Klar, T. A., Feldmann, J., et al. (2003). Biomolecular recognition based on single gold nanoparticle light scattering. *Nano Letters, 3*(7), 935–938.

Roiter, Y., Ornatska, M., Rammohan, A. R., Balakrishnan, J., Heine, D. R., & Minko, S. (2008). Interaction of nanoparticles with lipid membrane. *Nano Letters, 8*(3), 941.

Sönnichsen, C., Geier, S., Hecker, N. E., von Plessen, G., Feldmann, J., Ditlbacher, H., et al. (2000). Spectroscopy of single metallic nanoparticles using total internal reflection microscopy. *Applied Physics Letters, 77*(19), 2949–2951.

Schmitt, E. K., Nurnabi, M., Bushby, R. J., & Steinem, C. (2008). Electrically insulating pore-suspending membranes on highly ordered porous alumina obtained from vesicle spreading. *Soft Matter, 4*(2), 250–253.

Tanaka, M., & Sackmann, E. (2005). Polymer-supported membranes as models of the cell surface. *Nature, 437*(7059), 656–663.

Yethiraj, A., & Weisshaar, J. C. (2007). Why are lipid rafts not observed in vivo? *Biophysical Journal, 93*(9), 3113–3119.

Chapter 8
The Optimal Aspect Ratio for Plasmonic Bio-Sensing

The sensitivity of plasmonic particles to the immediate dielectric environment allows to monitor the dielectric constant of liquids and binding events of molecules to the gold particle surface. Here, by means of simulations and experiments, I investigate which aspect ratio (AR) of gold nanorods is ideal for plasmonic sensing by employing various measures for "ideal" behavior. There are several different quantities that describe the performance of a plasmonic structure for sensing applications on a single particle level—and all of them have their merits for certain applications. I will discuss (Sect. 8.2) the most important of them—the plasmonic sensitivity to refractive index change as well as various "figures of merit"—and present their dependency on the nanorods' geometry from calculations for spherically capped gold rods with the Boundary Element Method. I find aspect ratios with values between 3 and 4 to be optimal and confirm these identified trends by experimental results (Sect. 8.4) obtained using single particle dark-field scattering spectroscopy, which was performed in collaboration with Arpad Jakab. In Sect. 8.5 I discuss a probable reason for the existence of an "optimal aspect ratio". The results presented in this chapter were submitted as a publication to the journal Plasmonics (Becker et al. 2010).

8.1 Introduction

For dielectric plasmonic nanoparticle sensors, one hopes to have a large spectral shift for a given amount of analyte or refractive index change of the environment. Initially, spherical gold particles were used (Raschke et al. 2003; McFarland and Van Duyne 2003), but were soon replaced by gold nanorods (Chap. 7) due to their higher sensitivity on refractive index changes (Lee and El-Sayed 2006). Since the sensitivity depends on the particles' aspect ratio, I did some appropriate investigations using simulations based on the boundary element method (BEM, Sect. 2.4.2) to obtain the "optimal" aspect ratio. However, for sensing applications not only the absolute size of the resonance shift is interesting, but also the resolving precision to detect

J. Becker, *Plasmons as Sensors*, Springer Theses,
DOI: 10.1007/978-3-642-31241-0_8, © Springer-Verlag Berlin Heidelberg 2012

these resonance changes. The resolution is given by the linewidth of the resonance spectrum and therefore a figure of merit (FOM) was introduced recently (Sherry et al. 2005) taking both into account, the size of the shift per refractive index unit and the spectral linewidth. Nevertheless, this measure is only useful for sensors having a Gaussian- or Lorentz-shaped resonance, where a determination of a spectral linewidth is possible. To allow also the comparison of more complex shaped resonances I define a more general figure of merit (FOM*) in the following chapter.

8.2 Plasmon Sensor Quality

Changing the refractive index n of the embedding medium by a given amount dn shifts the plasmon resonance position by $\Delta\lambda$ (Fig. 8.1a). The corresponding proportionality constant or plasmonic sensitivity S can be expressed in wavelength (S_λ) or energy (S_E) units (Burgin et al. 2008):

$$S_\lambda = \mathrm{d}\lambda_{\mathrm{res}}/\mathrm{d}n \tag{8.1}$$

$$S_E = \mathrm{d}E_{\mathrm{res}}/\mathrm{d}n = S_\lambda \mathrm{d}E/\mathrm{d}\lambda = -S_\lambda/\lambda^2 \cdot 1240\,\mathrm{nm/eV} \tag{8.2}$$

The relatively broad plasmon linewidth Γ (full width at half maximum) complicates the analysis further, because the plasmon linewidth of nanostructures with different geometries can vary more than tenfold. Since it is easier to detect a given resonance shift for narrow lines, the resonance shift relative to the linewidth is a more meaningful measure of the sensoric quality. This dimensionless quantity is often referred to as the "figure of merit" FOM (Sherry et al. 2005):

$$\mathrm{FOM} = \frac{S_\lambda[\mathrm{nm}]}{\Gamma[\mathrm{nm}]} = \frac{S_E[\mathrm{eV}]}{\Gamma[\mathrm{eV}]} \tag{8.3}$$

The FOM is easily determined experimentally and allows for the comparison of the plasmonic properties of many different structures with a single sharp plasmonic resonance. For more complex plasmonic responses (such as in metamaterial structures based on an analogue of electromagnetically induced transparency (EIT) (Liu et al. 2009)), where the plasmon resonance does not follow a simple Lorentz peak shape, the concept needs to be refined. In practice, one would normally detect a spectral shift of a resonance as a relative intensity change dI/I at a fixed wavelength λ_0 induced by a small refractive index change dn. We can therefore define an alternative dimensionless figure of merit (FOM*):

$$\mathrm{FOM}^* = \left[\frac{(\mathrm{d}I/I)}{\mathrm{d}n}\right]_{\max} = \left[\frac{S_\lambda \cdot (\mathrm{d}I/\mathrm{d}\lambda)}{I}\right]_{\max} \tag{8.4}$$

The wavelength λ_0 is chosen such that FOM* has a maximum value—for gold nanorods in the shoulder of the resonance of the long-axis plasmon (Fig. 8.1b).

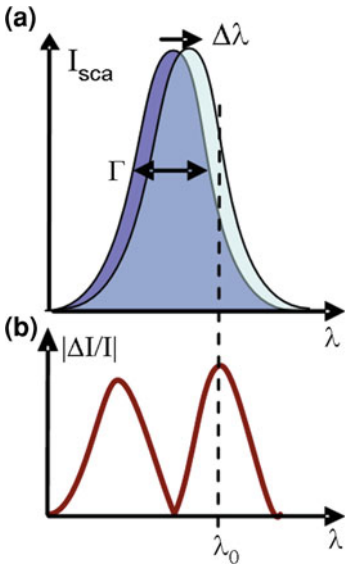

Fig. 8.1 **a** The plasmon resonance shifts ($\Delta\lambda$) upon changing the refractive index of the surrounding medium by Δn. To detect such changes, the sensitivity $S_\lambda = \Delta\lambda/\Delta n$ needs to be large. Other important parameters that characterize plasmonic sensors are the plasmon linewidth Γ and **b** the wavelength position λ_0 where the relative intensity change $|\Delta I/I|$ is largest (see text) [Image taken from reference Becker et al. (2010)]

Bio-sensing applications are even more complex. In this case, one seeks to detect the binding of small (organic) molecules to the nanoparticle surface instead of exchanging the entire embedding medium. The spectral shift now depends on the relative size of the molecules to the volume the plasmon field penetrates into the medium. Furthermore, the sensitivity is reduced with increasing distance to the particles surface. A "figure of merit" trying to capture the different sensing volumes of various nanostructures can be defined as the $\mathrm{FOM}^*_{\mathrm{layer}}$ for a homogeneous coating of molecules with a specific refractive index (for example, $n = 1.5$, typical for organic molecules) in a layer of thickness l around the particle normalized to this layer thickness. The formal definition of this "figure of merit for thin layers" $\mathrm{FOM}^*_{\mathrm{layer}}$ is therefore:

$$\mathrm{FOM}^*_{\mathrm{layer}} = \left[\frac{(\mathrm{d}I/I)}{\mathrm{d}l}\right]_{\max} \tag{8.5}$$

To compare the general sensing quality of different nanostructures, the limit of $\mathrm{FOM}^*_{\mathrm{layer}}$ for $l \to 0$ gives a defined value. Table 8.1 summarizes the different quantities used to determine the quality of plasmon sensors and their definitions.

Table 8.1 Summary of the different quantities describing the quality of plasmon sensors regarding their ability to detect changes in their environment: plasmonic sensitivity S_λ and S_E in wavelength and energy units, the figures of merit as classical definition (FOM), in generalized form (FOM*), and for thin layers ($\text{FOM}^*_{\text{layer}}$)

Quantity	Definition	AR_{opt}	Max. value
S_λ	$\mathrm{d}\lambda_{\text{res}}/\mathrm{d}n$	∞	
S_E	$\mathrm{d}E_{\text{res}}/\mathrm{d}n$	3.0 (4.4)	0.85 eV/RIU
FOM	$S_\lambda/\Gamma_\lambda = S_E/\Gamma_E$	4.3 (3.2)	11.1 (10.9)
FOM*	$\left[\frac{(\mathrm{d}I/I)}{\mathrm{d}n}\right]_{max}$	4.2 (3.1)	24 (23)
$\text{FOM}^*_{\text{layer}}$	$\lim_{l\to 0}\left[\frac{(\mathrm{d}I/I)}{\mathrm{d}l}\right]_{max}$	3.0 (4.3)	0.57/nm

The last columns list the optimal aspect ratio AR_{opt} (the value in bracket corresponds to the second maximum) for gold nanorods with 20 nm diameter in an aqueous environment and the value of the corresponding quantity at the maximum (see Sect. 8.4)

8.3 Description of Calculation Methods

We simulate the light scattering cross sections of gold nanorods by solving Maxwell's equations using the BEM and tabulated optical constants for gold (Johnson and Christy 1972). Regarding shape, we use rods with spherical end-caps varying the particle length while keeping the diameter constant at 20 nm. Even though the exact end-cap geometry influences the resonance position (Prescott and Mulvaney 2006), many researcher have successfully used spherical end-caps for their simulations (Bryant et al. 2008). We vary the aspect ratio by changing only the particle length because gold nanoparticle synthesis usually results in particles of comparable width. From the BEM calculations, we find a linear relationship between aspect ratio AR and plasmon resonance wavelength (Eq. 2.48): $\lambda_{\text{res}} = 94(AR - 1)[\text{nm}] + 532\ [\text{nm}]$. The calculations of the layer effect for $\text{FOM}^*_{\text{layer}}$ were performed within the quasi-static approximation (QSA, Sect. 2.2.3) for spheroids since we did not implement coated particles in our BEM simulations so far. However, comparisons of QSA with full solutions for the Maxwell equations have shown good qualitative agreement (Prescott and Mulvaney 2006).

8.4 Results

The plasmon sensitivity in wavelength units S_λ (calculated with BEM) shows the expected (Lee and El-Sayed 2006) steady increase for increasing aspect ratio (Fig. 8.2a), whereas the plasmonic sensitivity in energy units S_E shows a maximum at an aspect ratio of $\text{AR}_{\text{max}} = 3$ (Fig. 8.2b).

Both the "classical" figure of merit (FOM) and the more general FOM* show the same trend with two maxima (Fig. 8.3a). The classical FOM has a maximum for rods with an aspect ratio of AR = 4.3 and a second local maximum at AR = 3.2.

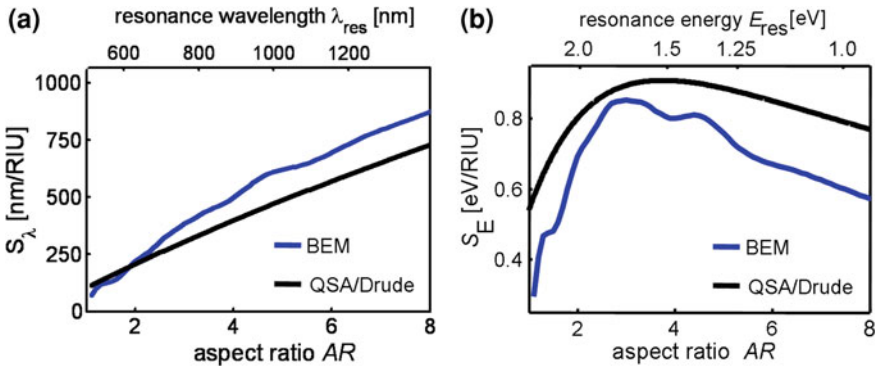

Fig. 8.2 The plasmonic sensitivity in wavelength units S_λ. **a** shows a steady increase for larger aspect ratio, while the plasmonic sensitivity in energy units S_E; **b** shows a maximum for gold nanorods with aspect ratio AR = 3.0. The *blue line* show data calculated with the BEM, assuming gold rods with a diameter of 20 nm and spherical endcaps embedded in water ($n = 1.33$). Similar trends are found for simple calculations using the quasi-static approximation (QSA) and a Drude dielectric function for gold (*black lines*) [Image taken from reference Becker et al. (2010)]

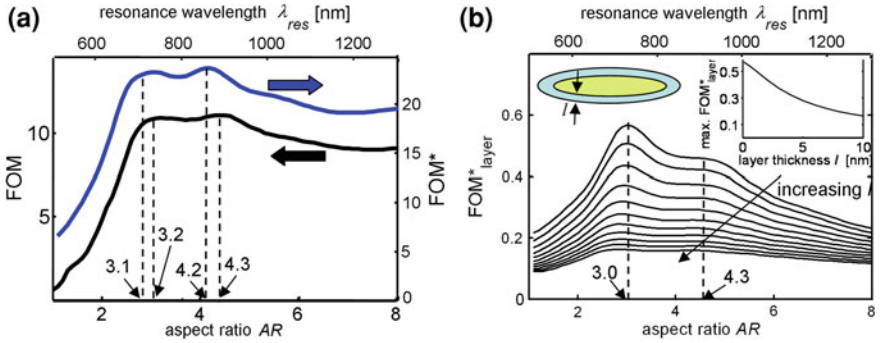

Fig. 8.3 To identify the optimal aspect ratio for plasmon sensing, various "figure of merits" (FOM) are calculated. **a** The classical FOM defined as plasmon sensitivity S divided by plasmon linewidth Γ (*left axis*) is compared to a generalized FOM* defined as the maximal relative intensity change $|\Delta I\ I|$ for a small refractive index change Δn (*right axis*). While the "classical" figure of merit FOM has a maximum for an aspect ratio of AR = 4.3 and a second maximum at AR = 3.2, the generalized FOM* has its maximum at AR = 4.2 with its second local maximum at AR = 3.1. **b** the FOM^*_{layer} takes into account the sensing volume by considering the plasmon change induced by a small layer around the particle normalized to the layer thickness (0.01 nm $< l <$ 10 nm in 1 nm steps). The plasmon sensing quality FOM^*_{layer} decreases with increasing layer thickness (*inset*) and shows a maximal value of $FOM^*_{layer} = 0.55$ for $l \to 0$ at an aspect ratio AR = 3.0 (Data for **a** are calculated by BEM for gold nanorods with spherical end-caps and 20 nm diameter, data for **b** within the QSA for spheroids) [Image taken from reference Becker et al. (2010)]

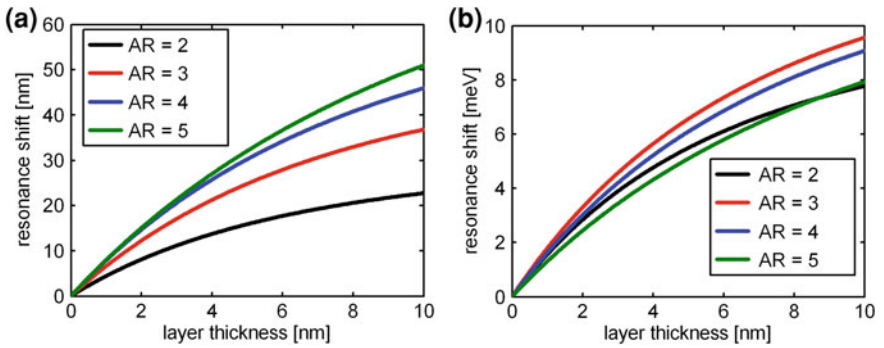

Fig. 8.4 Resonance shift in respect to the layer thickness for gold nanorods with different aspect ratios in wavelength units (**a**) and energy units (**b**). The calculation was performed within the QSA for spheroids with a fixed diameter of 20 nm embedded in aqueous solution and assuming a refractive index of $n = 1.5$ for the coating layer

The maxima of the generalized FOM* is slightly shifted to rod aspect ratios of AR $= 4.2/3.1$ (cf. Table 8.1). The values of the "figure of merit for small layers" $\text{FOM}^*_{\text{layer}}$ (obtained by QSA calculations) are shown in Fig. 8.3b for increasing layer thickness l and show maxima at the aspect ratios of AR $= 3.0$ and AR $= 4.3$. The first maximum at AR $= 3.0$ is higher for thin layers and in the limit of layer thickness $l \to 0$. Hence, rods with aspect ratios in the range of 3–4 are the best candidates to investigate changes in the refractive index of the embedding medium.

Figure 8.4a, b provide the resulting shifts for gold nanorods with different aspect ratios (AR $= 2, 3, 4, 5$) in aqueous solution in respect to the coating layerthickness in wavelength—and energy units, respectively. The calculations where performed using the quasi-static approximation, assuming gold spheroids in aqueous solution with 20 nm in diameter and a refractive index of $n = 1.5$ for the coating layer. Furthermore, these calculations confirm the results presented in Fig. 8.2 of a higher plasmonic sensitivity for larger aspect ratios in wavelength units S_λ, as well as a maximal plasmonic sensitivity in energy units S_E for rods with aspect ratios of $3 <$ AR < 4, since the appropriate lines are above the lines representing AR $= 2$ and 5 (Fig. 8.4b).

8.4.1 Experimental Results

To verify the theoretical conclusions given above, we compared the theoretical results with experimental values measured on single particles. The particle spectra were obtained in the fastSPS setup (Sect. 5.1) for nanorods immobilized in a glass capillary and exposed to liquids with various refractive indices. To remove as many as possible of the molecules attached to the particles surface the glass capillary is rinsed for at least 15 min with distilled water ($n_1 = 1.333$) and the scattering spectra of all particles

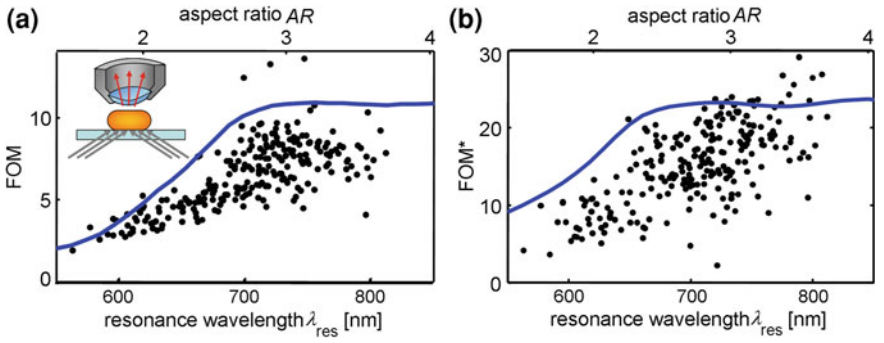

Fig. 8.5 Experimental data (each *black dot* represents one single particle) for the figures of merit FOM (**a**) and FOM* (**b**) obtained by single particle spectroscopy in a dark-field microscope (*inset*). The absolute values are slightly lower than the theoretical prediction (*blue line*, see also Fig. 8.3a) due to the attachment of the gold rods to a glass substrate which limits the accessible surface (*inset*) [Image taken from reference Becker et al. (2010)]

in the field of view are then recorded. After rinsing the glass capillary with glucose solution (25 wt% $n_2 = 1.372$) for 15 min, we again investigate the scattering spectra of the same particles. The resulting scattering spectra $I_1(\lambda)$ and $I_2(\lambda)$ where used to calculate the values of FOM according to Eq. 8.3 and FOM* according to:

$$\mathrm{FOM}^* = \left[\frac{|I_1(\lambda) - I_2(\lambda)|}{1/2 \cdot (I_1(\lambda) + I_2(\lambda))} \right]_{\max} / (n_2 - n_1) \tag{8.6}$$

In practice this slightly modified equation has to be used instead of the original Eq. 8.4, since the definition of FOM* given there is only valid for $\Delta n \to 0$. The resulting values for FOM and FOM* are shown in Fig. 8.5a, b, respectively and show the same trend as predicted by the BEM simulations. The values are generally lower than the calculated values due to the influence of the supporting glass substrate and are potentially also influenced by a thin organic coating of the particles remaining from the synthesis.

8.5 Discussion

The existence of a maximum of the plasmon sensitivity in energy units can be derived from a simple calculation of the polarizability of a spheroid in quasi-static approximation: The polarizability α of a spheroid within the quasi-static approximation is given by (Eq. 2.22):

$$\alpha = V \epsilon_0 \frac{\epsilon_r - 1}{1 + L\,(\epsilon_r - 1)}$$

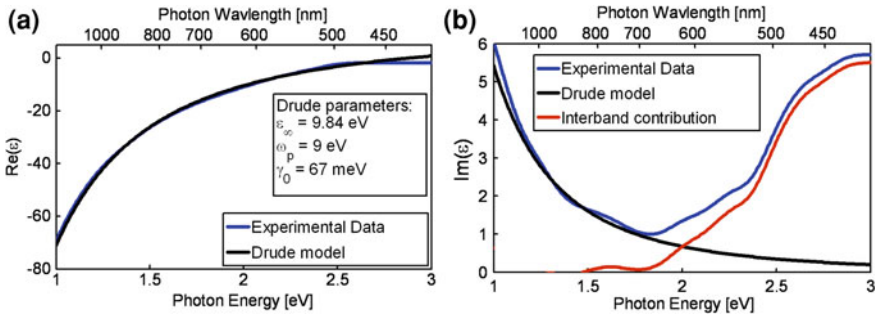

Fig. 8.6 Real and imaginary part of the dielectric function of gold (**a** and **b**, respectively). Experimental data are taken from Johnson and Christy (1972) and compared to calculated values using the Drude model (Eq. 8.8) with the given Drude parameters for gold Sönnichsen (2001). The difference between measurement and theory in the imaginary part of the dielectric function is due to the interband contribution, which is not explained by the Drude model [Image taken from reference Becker et al. (2010)]

where V is the particle volume, $\epsilon_r = \epsilon_\mathrm{p}/\epsilon_\mathrm{m}$ is the relative dielectric function of the particle with respect to the medium (Eq. 2.16), and L is a geometrical shape factor. A resonance is occurring, when the real part of the denominator of this equation is approaching zero (i.e. $1 + L \cdot [\Re(\epsilon_r) - 1] = 0$), which can be transformed into:

$$\Re(\epsilon_p) = (1 - 1/L) \cdot \epsilon_m \tag{8.7}$$

This real part of the dielectric function ϵ_p of the particle is given in a good approximation by the Drude model with respect to the photon energy ω (Fig. 8.6) (Sönnichsen 2001):

$$\epsilon_p = \epsilon_\infty - \frac{\omega_p^2}{\omega\,(\omega + i\gamma_0)} \approx \epsilon_\infty - \frac{\omega_p^2}{\omega^2} + i\frac{\gamma_0 \omega_p^2}{\omega^3} \tag{8.8}$$

$$\Re(\epsilon_p) \approx \epsilon_\infty - \omega_p^2/\omega^2 \tag{8.9}$$

ϵ_∞: contribution of the bound electrons to the polarizability
γ_0: electron relaxation rate
ω_p: plasma frequency

In the resonance $\omega = E_\mathrm{res}$ is obtained, and by equalizing Eqs. 8.7 and 8.9, an equation to calculate the resonance energy can be found. Using furthermore the relationship between the dielectric function and the refractive index of the embedding medium ($\epsilon_m = n^2$) following equation is received:

$$E_\mathrm{res} = \frac{\omega_p}{\sqrt{\epsilon_m/L + \epsilon_\infty - \epsilon_m}} = \frac{\omega_p}{\sqrt{n^2/L + \epsilon_\infty - n^2}} \tag{8.10}$$

To calculate now the plasmonic sensitivity S_E [eV/RIU] on changes in the refractive index n this equation has to be derivated with respect to n:

$$S_E[\text{eV/RIU}] = \frac{\mathrm{d}}{\mathrm{d}\,n} E_{\text{res}} = \frac{\omega_p \cdot n\,(1/L - 1)}{\left(n^2/L + \epsilon_\infty - n^2\right)^{3/2}} \tag{8.11}$$

To calculate the position of this maximum Eq. 8.11 has initially to be derivated with respect to L, since this geometrical factor is directly correlated to the aspect ratio (Eq. 2.24):

$$\frac{\mathrm{d}}{\mathrm{d}\,L} S_E[\text{eV/RIU}] = \frac{-\omega_p n/L^2 \cdot \left(n^2/L + \epsilon_\infty - n^2\right) + 3/2\left(\omega_p n/L - \omega_p n\right) n^2/L^2}{\left(n^2/L + \epsilon_\infty - n^2\right)^{5/2}} \tag{8.12}$$

This equation has then to be set equal to zero and solved for the geometrical factor L:

$$L = \frac{n^2}{n^2 + 2\epsilon_\infty} \tag{8.13}$$

which can thereafter be transformed into the appropriate aspect ratio via Eq. 2.26:

$$AR = \left(\frac{n^2}{n^2 + 2\epsilon_\infty}\right)^{-0.625} - 1$$

For water with a refractive index of $n = 1.33$ this equation results for gold particles in an aspect ratio of AR $= 3.8$.

The calculation of the plasmonic sensitivity S_λ can also be performed in wavelength units. Therefore Eq. 8.10, which is in electronvolt units, has to be transformed into wavelength units via Eq. 2.51 and afterwards derivated also with respect to n:

$$S_\lambda[\text{nm/RIU}] = \frac{\mathrm{d}}{\mathrm{d}\,n}\left(\frac{1240}{\omega_p} \cdot \sqrt{n^2/L + \epsilon_\infty - n^2}\right) = \frac{1240 \cdot n \cdot (1/L - 1)}{\omega_p \sqrt{n^2/L + \epsilon_\infty - n^2}} \tag{8.14}$$

The resulting functions for the sensitivity in wavelength units S_λ (Eq. 8.14) as well as in energy units S_E (8.11) are plotted for gold ($\omega_p = 9$ eV, $\epsilon_\infty = 9.84$, aspect ratio is connected to L via Eq. 2.24) in aqueous solution ($n = 1.33$) in Fig. 8.2a, b as black lines. Although the derivation of these two equations follow a simple principle, the agreement with the exact BEM calculations are quite good. Interestingly, the aspect ratio with the highest plasmon sensitivity in energy units AR_{max} depends on the polarizability of the inner electrons of the metal ϵ_∞ and the refractive index of the medium. For water ($n = 1.33$) as a medium, the optimal aspect ratio becomes $\text{AR}_{\text{max}} = 3.8$. Since the Drude model does not include the contribution of interband damping to the imaginary part of the dielectric function, we conclude that the

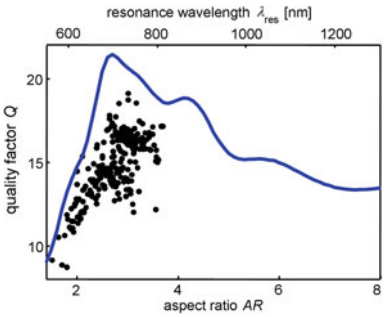

Fig. 8.7 The quality factor Q (see Eq. 8.15) shows a maximum for rods with an aspect ratio of approximately AR $= 3$ and decreases for larger aspect ratios. The *blue line* represents the results obtained by BEM calculations, while the *black dots* correspond to measurements on single gold nanorods [Image taken from reference Becker et al. (2010)]

maximum in plasmonic sensitivity S_E is not caused by the effect of those interband excitations.

Explanation of the Optimal Aspect Ratio

Yet, what is the reason for the "optimal aspect ratio" for the three "figures of merit"? We believe the quality factor Q is the key quantity in explaining this behavior. The quality factor of an oscillation describes the number of oscillations until the oscillation is damped. We find it plausible that a longer plasmon oscillation lifetime (i.e. a higher quality factor) results in a more sensitive dependency on changes in the surroundings. For a classical driven harmonic oscillator, the resonance frequency divided by the linewidth of the resonance Γ gives the quality factor:

$$Q = E_{\text{res}} / \Gamma \tag{8.15}$$

Figure 8.7 shows the quality factor as a function of the aspect ratio for gold nanorods (calculated by the BEM and measured experimentally on single particles). Evidently, a maximum is found around AR $= 3$. The initial rise from $Q(\text{AR} = 1) = 8$ to $Q(\text{AR} = 3) = 22$ is easily explained considering the reduced plasmon damping as the resonance shifts to lower energies with an increasing aspect ratio (Sönnichsen et al. 2002). The slow decrease above the aspect ratio of 3 is due to the decreasing resonance energy divided by the (more or less) constant Drude damping. The similarity between the way the quality factor and the figures of merit depend on the aspect ratio is a strong hint but not solid proof that one is the cause of the other. It is desirable to have more detailed investigations of this aspect.

8.6 Conclusion

In summary, for the four measures for an "optimal plasmonic sensor", namely plasmonic sensitivity S, figure of merit FOM, generalized figure of merit FOM*, and figure of merit for thin layers $\text{FOM}^*_{\text{layer}}$, there is an optimum aspect ratio around 3–4, where gold nanorods show the best sensitivity. Only the plasmonic sensitivity in wavelength units S_λ increases steadily with aspect ratio. Contrary to many claims, the four plasmonic property measures of gold nanorods do not steadily increase towards the infrared spectral region but show an optimum in the near infrared. Even though gold nanorods show very strong plasmon resonances with high quality factors and are, at the same time, small in volume, we cannot exclude the idea that other shapes of metal structures (bi-pyramids, rattles, pairs of particles, EIT structures etc) are even better plasmon sensors. We hope that our new definition of a generalized figure of merit and the corresponding generalized figure of merit for small layers will trigger the comparison of plasmon sensor quality of many more complicated metal structures.

References

Becker, J., Trügler, A., Jakab, A., Hohenester, U., & Sönnichsen, C. (2010). The optimal aspect ratio of gold nanorods for plasmonic bio-sensing. *Plasmonics, ASAP, 5*, 161–167. doi:10.1007/s11468-010-9130-2.

Raschke, G., Kowarik, S., Franzl, T., Sönnichsen, C., Klar, T. A., Feldmann, J., et al. (2003). Biomolecular recognition based on single gold nanoparticle light scattering. *Nano Letters, 3*(7), 935–938.

McFarland, A. D., & Van Duyne, R. P. (2003). Single silver nanoparticles as real-time optical sensors with zeptomole sensitivity. *Nano Letters, 3*(8), 1057–1062.

Lee, K.-S., & El-Sayed, M. (2006). Gold and silver nanoparticles in sensing and imaging: Sensitivity of plasmon response to size, shape, and metal composition. *Journal of Physical Chemistry B, 110*(39), 19220–19225.

Sherry, L. J., Chang, S. H., Schatz, G. C., Van Duyne, R. P., Wiley, B. J., & Xia, Y. N. (2005). Localized surface plasmon resonance spectroscopy of single silver nanocubes. *Nano Letters, 5*(10), 2034–2038.

Burgin, J., Liu, M. Z., & Guyot-Sionnest, P. (2008). Dielectric sensing with deposited gold bipyramids. *Journal of Physical Chemistry C, 112*(49), 19279–19282.

Liu, N., Weiss, T., Mesch, M., Langguth, L., Eigenthaler, U., Hirscher, M., Sönnichsen, C., & Giessen, H. (2009). Planar metamaterial analogue of electromagnetically induced transparency for plasmonic sensing. *Nano Letters, 10*, 1103–1107. doi:10.1021/nl902621d.

Johnson, P., & Christy, R. (1972). Optical constants of the noble metals. *Physical Review B, 6*(12), 4370–4379.

Prescott, S. W., & Mulvaney, P. (2006). Gold nanorod extinction spectra. *Journal of Applied Physics, 99*(12), 123504.

Bryant, G., Garcia de Abajo, F., & Aizpurua, J. (2008). Mapping the plasmon resonances of metallic nanoantennas. *Nano Letters, 8*(2), 631–636.

Sönnichsen, C. (2001). *Plasmons in metal nanostructures*. Mnchen: Cuvillier Verlag Göttingen.

Sönnichsen, C., Franzl, T., Wilk, T., von Plessen, G., Feldmann, J., Wilson, O., et al. (2002). Drastic reduction of plasmon damping in gold nanorods. *Physical Review Letters, 88*(7), 077402.

Chapter 9
Increasing Nanoparticles' Refractive Index Sensitivity

Since the plasmon resonance of nanoparticles depends on the refractive index of the immediate environment, these particles form the basis of many sensing schemes (Anker et al. 2008). The sensitivity of plasmon sensors for the detection of changes in the environment varies greatly and depends on the particle material and its morphology (size and shape) (Lee and El-Sayed 2006). Spherical gold and silver nanoparticles with relatively low sensitivity were the first single particle "attoliter" plasmon sensors (McFarland and Van Duyne 2003; Raschke et al. 2003; Mock et al. 2003). However, the sensitivity has been improved using gold nanoshells (Sun and Xia 2002; Raschke et al. 2004) or rod-shaped (Nusz et al. 2008; Baciu et al. 2008) nanoparticles. There are two reasons for using non spherical particles: one is a higher plasmonic sensitivity resulting in a larger resonance shift if the refractive index of the embedding medium is changed (Perez-Juste et al. 2005). The second reason is the desire to shift the plasmon resonance to lower energies—away from competing interband transitions—to decrease the plasmon linewidth (Sönnichsen et al. 2002).

As shown in the previous chapter the sensitivity of gold nanorods can be optimized by choosing the ideal aspect ratio. To further increase this sensitivity by chemical modifications was another goal of my work. One possibility to achieve this is to coat the gold nanorods with a thin silver shell, which reduces the single particle linewidth (Sect. 9.2). This investigation was performed in collaboration with Inga Zins and published in Ref. Becker et al. (2008).

Another possibility is to synthesize a hollow gold shell around the rods ("nanorattle"), resulting in a larger plasmon sensitivity, which was shown by Yuriy Khalavka on ensemble measurements. Since for practical use the sensitivity in a single particle sensor arrangement is important, I measured the sensitivity on single particle level. Both, ensemble and single particle data, are described in (Sect. 9.3) and were published in Ref. Khalavka et al. (2009).

J. Becker, *Plasmons as Sensors*, Springer Theses,
DOI: 10.1007/978-3-642-31241-0_9, © Springer-Verlag Berlin Heidelberg 2012

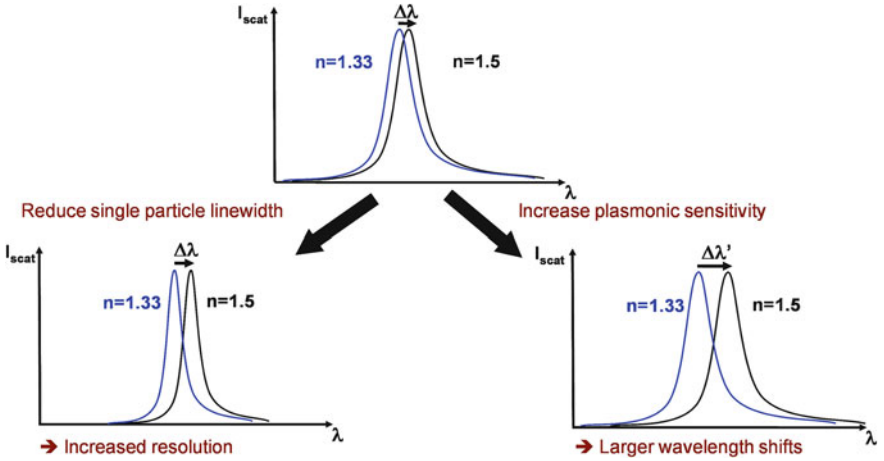

Fig. 9.1 An increase in the refractive index of the local environment of a nanoparticle shifts its resonance wavelength into the red. To increase the sensitivity there are two possibilities: a reduction of the single particle linewidth (while the size of the shift stays the same) increases the resolution and therefore also the sensitivity of the sensor (*left part* of the image). Another possibility is to increase the size of the shift by increasing the plasmonic sensitivity on changes in the refractive index, which is shown in the *right part* of the image

9.1 Introduction

To improve the sensitivity to changes in the refractive index n, there are in general two possibilities (Fig. 9.1): one is to reduce the single particle linewidth of the sensor which increases the resolution. Although the size of the shift stays the same it is easier to detect a small shift. The second possibility is to directly increase the shift by increasing the plasmonic sensitivity on changes in the refractive index.

In this work I investigate both possibilities. The reduction of single particle linewidth is achieved by coating gold nanorods with a small shell of silver. Since silver shows a smaller plasmon damping than gold (and therefore a smaller resonance linewidth), silver particles are an interesting alternative for improved sensors (Sect. 2.5.2). Unfortunately the synthesis of rodshaped silver nanoparticles is difficult and so far samples with narrow size distribution and without defects could not be prepared. Therefore we synthesized gold rods coated with a small silver shell (Sect. 3.2) and showed that this silver shell already leads to a reduced single particle linewidth (Sect. 9.2).

The second possibility for improvement is an increase of the plasmonic sensitivity. In principle, candidates for very sensitive plasmon sensors have a large part of the plasmon field penetrating the accessible dielectric environment. This favors hollow structures (cages, boxes) or nanoparticle-filled cages (rattles). So far, only a few examples of nanorattles with both core and shell made of metals were reported. Xia and co-workers synthesized spherical nanorattles consisting of Au/Ag alloy cores and

shells by means of an electroless galvanic replacement reaction (Sun et al. 2004). More recently, a promising synthesis of nanorattles with spherical Au core and Pt/Ag shell has been reported by Yang et al. (2006), but data on their chemical stability and plasmon sensitivity are lacking. For this reason we synthesize rodshaped gold nanorattles (Sect. 3.3) and show in Sect. 9.3 their increased sensitivity on refractive index changes of the environmental solution.

9.2 Silver Coating Reduces Single Particle Linewidth

As described, a small single particle plasmon linewidth implies a high sensing sensitivity. This intrinsic single particle plasmon linewidth is determined by the amount of damping and mainly due to interband and intraband excitation of electron-hole pairs, thus temperature, frequency, and material dependent (Sönnichsen et al. 2002). To reduce the plasmon linewidth of single gold nanorods, we coat these nanorods with a silver shell as described in Sect. 3.2.

Single Particle Measurement

I examined the single particle linewidth for both, coated and uncoated nanoparticles by observing the scattered light of individual nanoparticles by fastSPS (see Sect. 5.1). This setup is automated to allow the spectral investigation of several hundred nanoparticles with reasonable effort. For each particle spectrum, we extract the mean resonance position (λ_{res}) and the full width at half maximum — FWHM (cf. Fig. 9.2a inset). Because the excitation of d-band electrons into the conduction band requires a threshold energy, the linewidth increases for higher frequencies or smaller wavelengths. Hence, a plot of single particle FWHM as a function of the resonance wavelength λ_{res} shows an increase of linewidth at smaller wavelengths (Fig. 9.2). Most importantly, we observe a decrease of the single particle linewidth (FWHM) after silver coating compared to uncoated particles *at the same resonance wavelength* λ_{res}. The silver shell reduces the plasmon damping due to the higher energy required to excite d-band electrons into the conduction band of silver compared to gold. The interface between the gold core and the silver shell causes apparently no additional damping. This linewidth decrease is largest for thin coatings and less pronounced for a thicker silver shell.

Polarization Anisotropy

The increase of the single particle linewidth for a thick silver coating (compared to a thin coating) is probably due to the variation in the shell thickness around each particles as already observed in TEM Fig. 3.2b. To confirm the hypothesis of a decreasing rodlike shape for thick silver coatings, I measure the polarization anisotropy of the differently coated particles with the RotPOL setup Sect. 5.2. As Fig. 9.3a shows, a decrease in the optical polarization anisotropy for rods with thicker silver coating can indeed be observed, while for a thin silver coating the polarization anisotropy is similar to uncoated rods. This proves that a thick coating leads to an inhomogeneous growth of the shell for high silver concentrations.

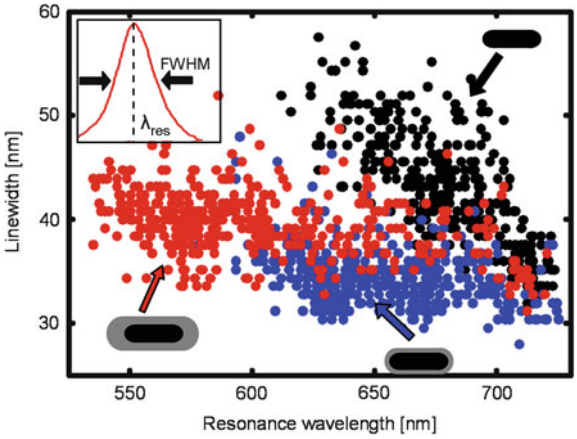

Fig. 9.2 Linewidth of gold nanorods (without coating (*black dots*), with a thin (*blue dots*) and thick (*red dots*) silver shell) plotted against their resonance wavelength, both extracted directly from scattering spectra (inset). On average, the linewidth (FWHM) of particles with silver coating is smaller than the linewidth of pure gold nanorods with similar resonance wavelength. The thicker silver shell shows a higher linewidth than the thin shell due to an anisotropic shell thickness [Image reprinted with permission of the American Chemical Society (Becker et al. 2008)]

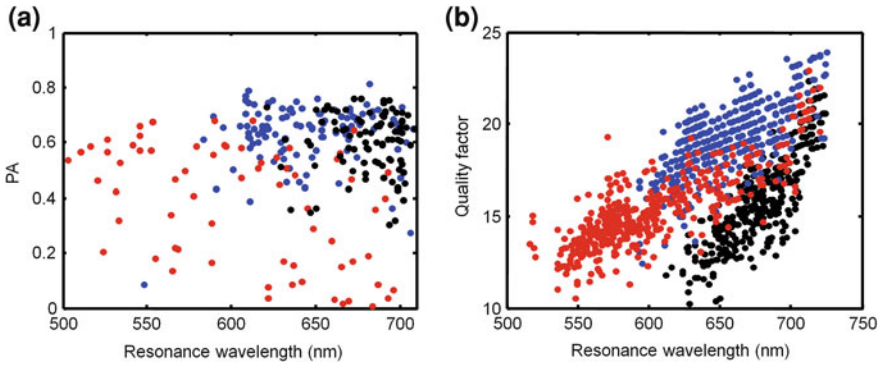

Fig. 9.3 **a** Polarization anisotropy (PA) for pure gold nanorods (*black dots*), with a thin silver coating (*blue dots*), and with a thick silver coating (*red dots*). PA is a measure for the degree of rod-like shape: it is expected to be close to 1 for perfect rods and close to 0 for perfect spheres. Clearly, the PA decreases for particles with thick coating. **b** The quality factor extracted from single particle scattering spectra are shown here for pure gold nanorods (*black dots*), those rods with a thin silver coating (*blue dots*) and thick silver coating (*red dots*). The silver coating increases the quality factor up to 2 fold [Image reprinted with permission of the American Chemical Society (Becker et al. 2008)]

Quality Factor

Additionally to the higher sensitivity, a smaller single particle linewidth means a lower plasmon damping, thus a longer plasmon lifetime and a higher field enhancement, which is beneficial for many plasmonic applications. The quality factor Q of a harmonic oscillator is related to the FWHM and the resonance wavelength λ_{res} by $Q = \text{FWHM} / \lambda_{\text{res}}$. The quality factor gives the amount of energy stored in an externally driven oscillator and is thus a measure for the field enhancement around the particles. The quality factor Q increases for silvercoated rods compared to gold rods at the same resonance wavelength (Fig. 9.3b). For example, at 670 nm, we find silver-coated gold rods with quality factors above 20, whereas uncoated rods show quality factors below 15. The enhancement of Raman signals (Kneipp et al. 1997) is believed to depend on Q^4, so the silver-coated gold rods should show an improvement in the signal of more than $(20/15)^4 \approx 3$.

9.3 Nanorattles Show an Increase of Plasmon Sensitivity

In order to test the plasmon sensitivity of gold nanorattles (Sect. 3.3) to changes in the dielectric environment, we systematically varied the refractive index of the aqueous surrounding by adding sugar, ethylene glycol, or glycerin to suspensions of gold particles and measured each time the resonance wavelength.

9.3.1 Ensemble Measurement

To measure the plasmonic sensitivity of a sample the refractive index n of the solutions is measured with a digital refractometer (Mettler Toledo, Refracto 30PX), and the position of the plasmon resonance peak λ_{res} is determined from the samples extinction spectrum (Sect. 4.1). The plasmon resonance shifts linearly to higher wavelength with increasing refractive index n of the surrounding environment (Fig. 9.4a) (Murphy et al. 2008) and therefore the plasmonic sensitivity S_λ is calculated according to $(S_\lambda[\text{nm/RIU}] = \text{d}\lambda_{\text{res}}/\text{d}n)$ (see Eq. 8.1) in units of nanometers per refractive index unit. In general, the plasmon sensitivity is expected to increase for rods with higher resonance wavelength due to their large polarizability Sect. 8.2—a trend we observe in the measurements on solid gold nanorods with different resonance wavelength. The sensitivity of an ensemble of gold nanorods is in the range of $S_\lambda^E = 150-263$ nm/RIU, which is much larger than the values for solid gold spheres ($S_\lambda^E = 44$ nm/RIU) (Chen et al. 2008) and gold cubes ($S_\lambda^E = 83$ nm/RIU) (Chen et al. 2008) and even larger than the value for spherical hollow gold nanoshells ($S_\lambda^E = 125$ nm/RIU) (Raschke et al. 2004). Indeed, we observed sensitivity values for rod-shaped gold nanorattles of up to $S_\lambda^E = 285$ nm/RIU (Fig. 9.4b), which is also slightly higher compared to recently

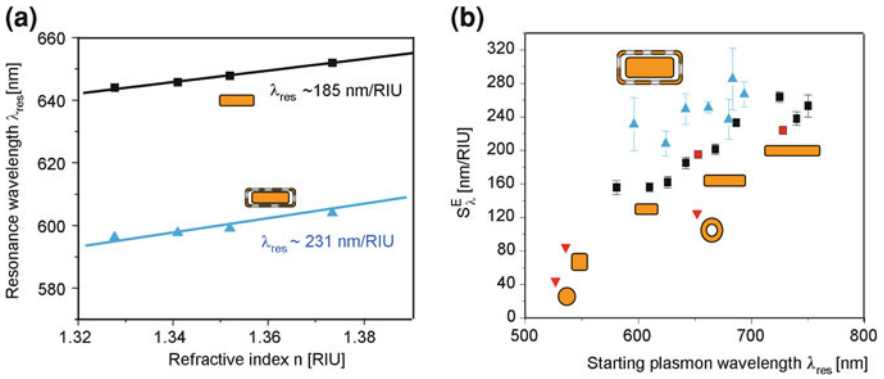

Fig. 9.4 **a** Position of the longitudinal plasmon resonance wavelength versus refractive index of the surrounding medium for gold nanorods and nanorattles (as indicated). The slopes show different sensitivities S_λ^E [nm/RIU] toward changes in the dielectric environment for both particles. **b** Overview of the S_λ^E values of different gold nanostructures: spheres, cubes, rods, shells, and rod-shaped nanorattles. Since the sensitivity S_λ^E depends not only on shape but also on the position of the resonance wavelength, we show the S_λ^E values as a function of the plasmon wavelength in water. The values for spheres, cubes, shells, and some rod samples are taken from the literature (Raschke et al. 2003, 2004; Chen et al. 2008). Our data for ensemble measurements on different samples of solid gold nanorods (*black labels*) show lower values for plasmon sensitivity than those of rod-shaped gold nanorattles, produced from these rods (*blue labels*) [Image reprinted with permission of the American Chemical Society (Khalavka et al. 2009)]

reported values for gold nanodiscs supported on dielectric pillars (Dmitriev et al. 2008).

9.3.2 Measurement on Single Particle Level

For practical use of nanorattles in plasmon sensors, the sensitivity in a single particle sensor arrangement is of great importance, where the particles are supported by a substrate, which forms part of a microfluidic flow cell. Single particle spectra are recorded by fast single particle spectroscopy (fastSPS, Sect. 5.1) which automatically records the spectra of about 50–100 single particles per measurement, which are initially immersed in distilled water. To measure the nanoparticle's sensitivity toward changes in the dielectric environment, we rinse them with solutions of different refractive indexes [sucrose (n = 1.378), ethylene glycol (n = 1.427), or dimethylsulfoxide (n = 1.4785)] and record the spectra of the previously investigated particles again. In several dozen experiments with different solvents, we investigated a total of 1,567 solid gold nanorods and 803 nanorattles. The median plasmon sensitivity of solid gold rods was $S_\lambda^{\text{rod}} = 169 \pm 1.3$ nm/RIU and for nanorattles $S_\lambda^{\text{rattles}} = 199 \pm 2.5$ nm/RIU (Fig. 9.5a). The relatively large standard deviations in

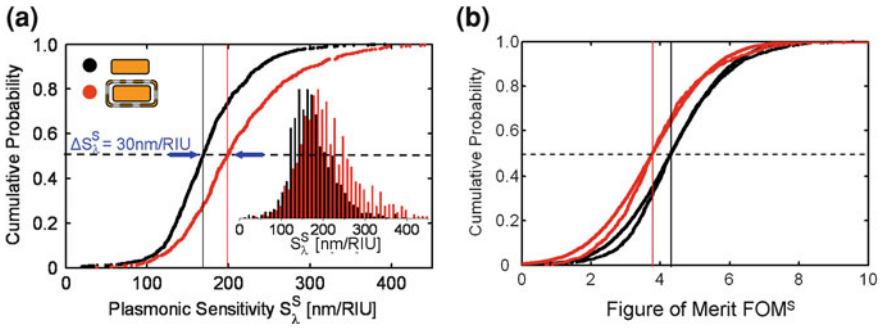

Fig. 9.5 **a** Cumulative probability distribution of S_λ^S values derived from measuring single particle spectra of 1567 gold nanorods and 803 gold nanorattles. The median $S_\lambda^S = 169 \pm 1.3$ nm/RIU and $S_\lambda^S = 199 \pm 2.5$ nm/RIU for the rods (*black*) and cages (*red*), respectively. The inset shows the corresponding normalized histograms. **b** Cumulative probability distribution of the figure of merit (FOM) derived from the measured single particle spectra. The median value is $FOM^S = 4.3 \pm 1.4$ and $FOM^S = 3.8 \pm 1.5$ for the rods (*black*) and cages (*red*), respectively. Although the rattles have a higher S_λ^S value compared to the rods, they show a smaller FOM^S value due to the larger FWHM as a result of the stronger plasmon damping in rattles, which increases the linewidth [Image reprinted with permission of the American Chemical Society (Khalavka et al. 2009)]

those values is caused both by large interparticle deviations within the same experiment as well as systematic deviations between subsequent experiments with new flow cells, particles, and solvents. Whereas the deviations between particles is expected from the polydispersity of the particles and points toward further chances for improvements, the large deviations in between subsequent experimental runs is puzzling. At present, we have not identified the factor causing these deviations, but we have collected sufficiently high statistics to report precise mean sensitivities (Student's t test proves significantly higher plasmon sensitivity of nanorattles compared to that of solid nanorods with >99.999 % probability.). However, previous reports for plasmon sensitivity with fewer statistics have probably overlooked this variation and should be regarded with some caution. Further study of these unexplained variations in plasmon sensitivity, which are independent of the type of particles under investigation, is clearly needed but may require ultraclean working environments. The single particle measurements yielded slightly higher FOM^S for the solid rods (4.3 ± 1.4) compared to that for the rattles (3.8 ± 1.5) (Fig. 9.5b) caused by the slightly stronger plasmon damping in rattles which increases the linewidth.

9.4 Conclusion

To show the improved sensitivity on changes in the refractive index, we investigated silver coated gold nanorods as well as rod-shaped gold nanorattles. Since silver coated particles show a reduced single particle linewidth *at the same reso-*

nance wavelength compared to bare gold nanorods, their sensitivity to changes in the refractive index is larger. Even though silver-coated nanoparticles have been prepared and studied before, this linewidth narrowing has not yet been reported. Only the spectroscopic investigation of several hundred single particles using the fastSPS approach made it possible to obtain enough statistics to compare particles *at the same resonance wavelength*. Each individual particle shifts in resonance wavelength after silver coating, but observing many different particles allows comparing pairs with the same resonance wavelength. Since the damping (and thus the single particle linewidth) changes with resonance wavelength, only this direct comparison at the same wavelength makes sense.

Additionally, we synthesized rod-shaped gold nanorattles and showed their improved sensitivity on refractive index changes by measuring the resonance wavelength in solutions with different refractive indices. Both, ensemble and single particle measurements revealed an increased sensitivity compared to gold nanorods. This increase results from the large surface area of nanorattles, since in the case of such hollow structures a large part of the plasmon field penetrates the accessible dielectric environment.

Both types of particles are promising candidates for detecting changes in the local dielectric environment. Since molecules have a larger refractive index compared to the environmental aqueous solution, these particles are optimized plasmon binding sensors compared to bare gold nanorods.

References

Anker, J. N., Hall, W. P., Lyandres, O., Shah, N. C., Zhao, J., & Van Duyne, R. P. (2008). Biosensing with plasmonic nanosensors. *Nature Materials, 7*(6), 442–453.

Baciu, C., Becker, J., Janshoff, A., & Sönnichsen, C. (2008). Protein-membrane interaction probed by single plasmonic nanoparticles. *Nano Letters, 8*(6), 1724–1728.

Becker, J., Zins, I., Jakab, A., Khalavka, Y., Schubert, O., & Sönnichsen, C. (2008). Plasmonic focusing reduces ensemble linewidth of silver-coated gold nanorods. *Nano Letters, 8*(6), 1719–1723.

Chen, H., Kou, X., Yang, Z., Ni, W., & Wang, J. (2008). Shape- and size-dependent refractive index sensitivity of gold nanoparticles. *Langmuir, 24*(10), 5233–5237.

Dmitriev, A., Hägglund, C., Chen, S., Fredriksson, H., Pakizeh, T., Käll, M., et al. (2008). Enhanced nanoplasmonic optical sensors with reduced substrate effect. *Nano Letters, 8*(11), 3893–3898.

Khalavka, Y., Becker, J., & Sönnichsen, C. (2009). Synthesis of rod-shaped gold nanorattles with improved plasmon sensitivity and catalytic activity. *Journal of the American Chemical Society, 131*(5), 1871–1875.

Kneipp, K., Wang, Y., Kneipp, H., Perelman, L. T., Itzkan, I., Dasari, R., et al. (1997). Single molecule detection using surface-enhanced raman scattering (sers). *Physical Review Letters, 78*(9), 1667–1670.

Lee, K.-S., & El-Sayed, M. (2006). Gold and silver nanoparticles in sensing and imaging: Sensitivity of plasmon response to size, shape, and metal composition. *Journal of Physical Chemistry B, 110*(39), 19220–19225.

McFarland, A. D., & Van Duyne, R. P. (2003). Single silver nanoparticles as real-time optical sensors with zeptomole sensitivity. *Nano Letters, 3*(8), 1057–1062.

Mock, J. J., Smith, D. R., & Schultz, S. (2003). Local refractive index dependence of plasmon resonance spectra from individual nanoparticles. *Nano Letters, 3*(4), 485–491.

Murphy, C. J., Gole, A. M., Hunyadi, S. E., Stone, J. W., Sisco, P. N., Alkilany, A., et al. (2008). Chemical sensing and imaging with metallic nanorods. *Chemical Communications, 5*, 544–557.

Nusz, G. J., Marinakos, S. M., Curry, A. C., Dahlin, A., Hook, F., Wax, A., et al. (2008). Label-free plasmonic detection of biomolecular binding by a single gold nanorod. *Analytical Chemistry, 80*(4), 984–989.

Perez-Juste, J., Pastoriza-Santos, I., Liz-Marzan, L. M., & Mulvaney, P. (2005). Gold nanorods: Synthesis, characterization and applications. *Coordination Chemistry Reviews, 249*(17–18), 1870–1901.

Raschke, G., Kowarik, S., Franzl, T., Sönnichsen, C., Klar, T. A., Feldmann, J., et al. (2003). Biomolecular recognition based on single gold nanoparticle light scattering. *Nano Letters, 3*(7), 935–938.

Raschke, G., Brogl, S., Susha, A. S., Rogach, A. L., Klar, T. A., Feldmann, J., et al. (2004). Gold nanoshells improve single nanoparticle molecular sensors. *Nano Letters, 4*(10), 1853–1857.

Sönnichsen, C., Franzl, T., Wilk, T., von Plessen, G., Feldmann, J., Wilson, O., et al. (2002). Drastic reduction of plasmon damping in gold nanorods. *Physical Review Letters, 88*(7), 077402.

Sun, Y., & Xia, Y. (2002). Increased sensitivity of surface plasmon resonance of gold nanoshells compared to that of gold solid colloids in response to environmental changes. *Analytical Chemistry, 74*(20), 5297–5305.

Sun, Y., Wiley, B., Li, Z.-Y., & Xia, Y. (2004). Synthesis and optical properties of nanorattles and multiple-walled nanoshells/nanotubes made of metal alloys. *Journal of the American Chemical Society, 126*(30), 9399–9406.

Yang, J., Lu, L., Wang, H., & Zhang, H. (2006). Synthesis of pt/ag bimetallic nanorattle with au core. *Scripta Materialia, 54*(2), 159–162.

Chapter 10
Plasmonic Focusing Reduces Ensemble Linewidth

In this chapter I present an effect the coating of gold nanorods with a silver shell is evocating: a reduction of the ensemble plasmon linewidth by changing the plasmon-shape relation, which connects the particle shape with its plasmon resonance wavelength. This change, we term "plasmonic focusing" (Sect. 10.2), leads to less variation of resonance wavelengths for the same particle size distribution. Section 10.3 explains the effect of increasing single particle linewidth during the coating process, which is therefore *not* the reason for the observed ensemble linewidth decrease. This is rather a result from a change in the plasmon-shape relation explained in Sect. 10.4. Using a simple model, the effect of the single particle linewidth can be subtracted from the ensemble linewidth, showing the plasmonic focusing effect is even larger than the measured ensemble linewidth decrease (Sect. 10.5). The discovery and explanation of this effect was performed in collaboration with Inga Zins and the results were published in reference Becker et al. (2008).

10.1 Introduction

The ensemble linewidth of a suspension of plasmonic nanoparticles is a convolution of the linewidth of individual particles and the distribution of their resonance wavelengths. A narrow ensemble plasmon linewidth is desirable for most plasmonic applications such as sensors (Elghanian et al. 1997; McFarland and Van Duyne 2003; Raschke et al. 2003), the enhancement of nonlinear optical effects (Nie and Emory 1997; Kneipp et al. 1997; Campion and Kambhampati 1998), light guiding (Maier et al. 2001; Quinten et al. 1998), labeling (Schultz et al. 2000), or tissue targeting (Brigger et al. 2002; Hirsch et al. 2003). The plasmon resonance wavelength is strongly dependent on the nanoparticle shape (Sect. 2.5.1); a narrow ensemble linewidth indicates therefore a low polydispersity of the plasmonic particles. The main factor influencing the resonance wavelength of rod-shaped particles is the aspect ratio, via a linear relationship we term the "plasmon-shape relation". Hence, three

J. Becker, *Plasmons as Sensors*, Springer Theses,
DOI: 10.1007/978-3-642-31241-0_10,

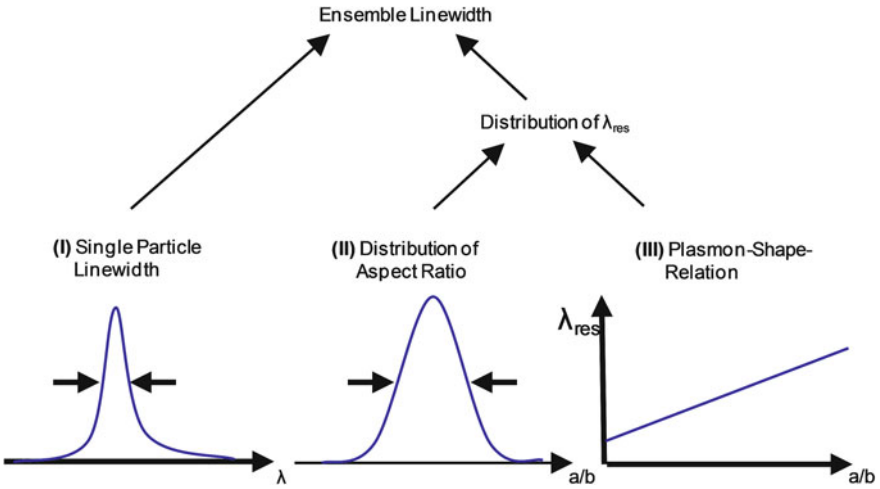

Fig. 10.1 The three factors contributing to the ensemble plasmon linewidth: (*I*) the single particle linewidth, (*II*) the width of the distribution in aspect ratios (a/b) in the sample, and (*III*) the slope of the plasmon-shape relation connecting aspect ratio (a/b) to resonance wavelength (λ_{res}). A change in the slope of the plasmon-shape relation (*III*) is responsible for the ensemble linewidth narrowing of gold nanorods after silver coating [Image reprinted with permission of the American Chemical Society Becker et al. (2008)]

factors effectively determine the ensemble plasmon linewidth: (I) the single particle linewidth, (II) the width of the distribution in aspect ratios in the sample, and (III) the slope of the plasmon-shape relation connecting aspect ratio to resonance wavelength (Fig. 10.1)

10.2 Explanation of the Plasmonic Focusing Effect

We find that coating gold nanorods with a thin shell of silver leads to a strong reduction of the ensemble linewidth. The quantitative examination of this effect leads to the surprising finding that this reduction is caused by a change in slope of the plasmon-shape relation (factor III), an effect we term "plasmonic focusing". The silver coating leaves the shape and size of the original gold nanorods intact, excluding factor II from the discussion. The contribution of the single particle linewidth to the observed ensemble linewidth (factor I) is complex due to simultaneous shifts in the central resonance wavelength. However, we are able to show by single particle experiments together with theoretical modeling that the single particle linewidth contribution actually counteracts plasmonic focusing.

To explain our term "plasmonic focusing", we first note that during nanoparticle crystallization in solution, the shape and size polydispersity of the ensemble typically increases by statistical variations over time. An exception is the well-known (chemical) focusing regime during nanocrystal growth (Peng et al. 1998; Reiss 1951;

Yin and Alivisatos 2005), where a faster growth of small compared to larger particles lets small particles "catch up". This effectively narrows or focuses the nanoparticle size distribution. The plasmonic focusing we observe, where the plasmon resonance linewidth of an ensemble of gold nanorods is smaller after silver coating than before, leaves the gold nanoparticles shape undisturbed but rather changes the way their shape polydispersity translates into spectral polydispersity. A shallower slope of the plasmon-shape relation narrows or focuses the distribution of plasmon resonances. In the ideal case of a completely flat plasmon-shape relation, all particles would have the same resonance wavelength regardless of their aspect ratio leading to an ensemble linewidth only limited by the intrinsic single particle linewidth. Another way of looking at plasmonic focusing is by observing the spectral shift induced by the silver coating. Silver coating generally leads to a blueshift, but the shift is stronger for particles with original larger resonance wavelengths.

Note the nontrivial choice of units in the discussion of linewidth changes accompanied with a resonance shift: a linewidth narrowing in energy or frequency units may correspond to a linewidth narrowing or broadening in wavelength units, depending on the magnitude of the resonance shift. Length or wavelength units have to be chosen here because of the almost linear relationship between aspect ratio and resonance wavelength (Link et al. 2005; Perez-Juste et al. 2005). Other geometric factors besides aspect ratio, namely end-cap geometry and particle volume, have a weak influence on the plasmon resonance compared to the aspect ratio (Prescott and Mulvaney 2006; Bryant et al. 2008). An ensemble linewidth in length units therefore relates to a certain polydispersity in aspect ratio regardless of the mean resonance wavelength. For other discussions, linewidth in energy units may be more appropriate, e.g. the single particles energy linewidth corresponds to the plasmon decay time.

Ensemble Linewidth

The extinction spectra show a strong narrowing of the plasmon resonance in the particle ensemble spectra after silver coating when compared to the linewidth of the original gold nanoparticles at least for thin silver coating (Fig. 10.2). This narrowing has to the best of my knowledge not been reported before and is only observable if the silver shell is very homogeneous. As it is evident from Fig. 3.2b, a slightly thicker silver layer typically leads to a more inhomogeneous coating resulting in a broadening of the ensemble linewidth compared to the optimal silver thickness.

10.3 Single Particle Observation During Coating Process

As described in Sect. 9.2 the single particle linewidth of silver-coated gold rods is smaller *at the same resonance wavelength* compared to uncoated rods. However, this effect is not responsible for the observed *ensemble* linewidth narrowing. The reason is the simultaneous reduction in the resonance wavelength toward regions with intrinsically higher plasmon damping. Depending on the initial and final wavelength,

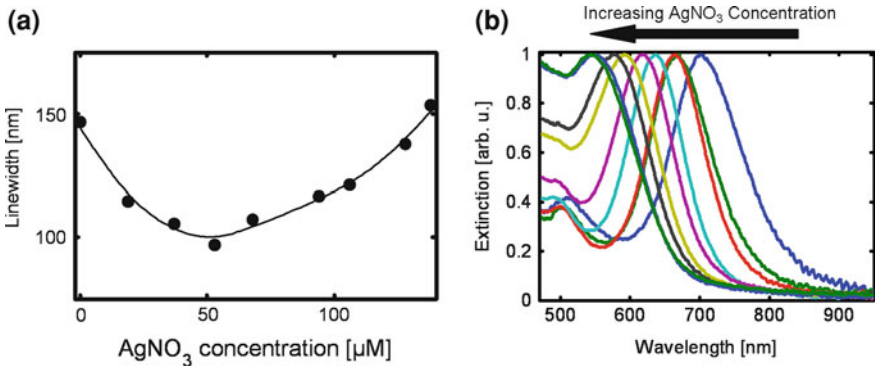

Fig. 10.2 **a** Ensemble linewidth as a function of silver concentration in the coating solution for a gold nanorod sample with an initial linewidth of 148 nm. The linewidth is the full width at half-maximum (*FWHM*) as determined directly from the spectra (shown in **b**). It shows a minimum at 53 μm, where it is reduced to 97 nm from the initial 148 nm (*thin line* is a guide to the eye) [Image reprinted with permission of the American Chemical Society Becker et al. (2008)]

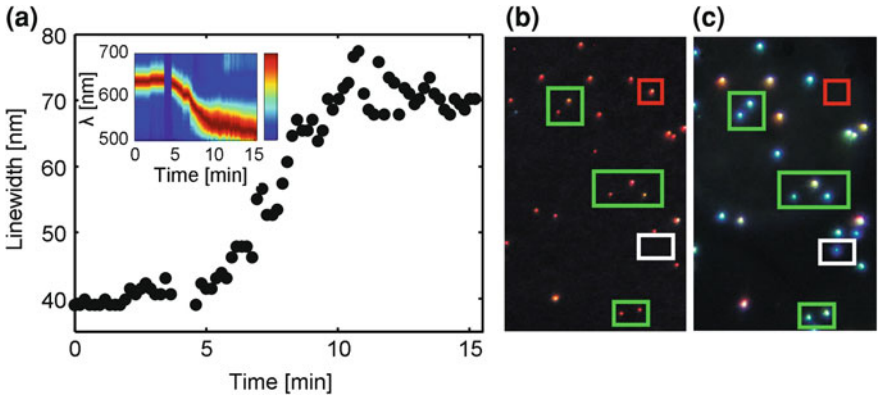

Fig. 10.3 (**a**) Observation of the linewidth change over time of a single gold nanorod exposed to the silver-coating solution. The inset shows the full spectra (*color* coded) over time [image taken from reference Becker et al. (2008)]. True color photograph of the same particles in the *dark*-field microscope before (**b**) and after coating (**c**). *Green boxes* show particles which get coated, while the *white box* indicates the emersion of a *blue* particle, which is probably a silver sphere. Due to adding and mixing solutions during the growth process some particles can vanish (*red box*)

this shift in resonance wavelength often results in a broadening of the linewidth of a given particle after coating with silver. We observe such plasmon linewidth broadening of an individual particle by continuously monitoring individual particles exposed to a coating solution (Fig. 10.3).

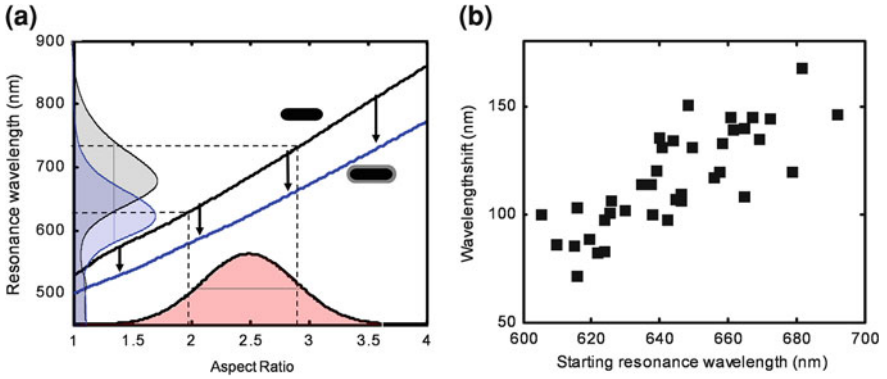

Fig. 10.4 **a** The plasmon-shape relation shows how the resonance wavelength depends on aspect ratio. Values derived theoretically within the quasi-static approximation are shown for gold rods in water (*black line*, n = 1.33) and with a 2.3 nm silver coating (*blue line*). The plasmon-shape relation converts an ensemble of particles with a distribution of aspect ratios (indicated by *pink shading*) into a distribution of resonance wavelengths (indicated by the *gray shaded* spectrum). The plasmon-shape relations are almost linear, i.e. a distribution of aspect ratios with a given width (polydispersity) gives a certain linewidth regardless of the mean aspect ratio. The shallower slope of the plasmon-shape relation for the silver-coated rods results therefore in a smaller spectral linewidth (*blue shaded* spectrum). An alternative way to look at the effect of coating is to observe the vertical differences between the two plasmon-shape relations (indicated by *black arrows*). Hence, rods with higher aspect ratio shift more on silver coating than those with a smaller aspect ratio. **b** Experimental data for the wavelength shifts of gold nanorods upon coating with silver as a function of the starting resonance wavelength. Each data point is extracted from two single particle measurements of the same particle before and after coating. Higher starting resonance wavelengths (i.e. rods with higher aspect ratio), result in larger wavelength shifts [Image reprinted with permission of the American Chemical Society Becker et al. (2008)]

10.4 Change of the Plasmon-Shape Relation

The single particle linewidth of particles becomes broader after silver coating as shown in the Chap 9. But why is a narrowing of the ensemble linewidth observable? The answer is a change in the plasmon-shape relation, which converts the distribution of particle aspect ratios into a distribution of plasmon resonances. In chemical focusing during nanocrystal growth, the growth of small particles is favored. Here, the silver coating shifts the plasmon resonances stronger for rods with higher aspect ratios than for particles with lower ones. Therefore, the same particle distribution leads to a narrower distribution of plasmon resonances after coating due to a different slope in the plasmon-shape relation (Fig. 10.4a). This purely electrodynamic effect that we call plasmonic focusing is responsible for the observed narrowing of the ensemble linewidth. The shallower slope of the plasmon-shape relation for silver coated particles is caused by the strong wavelength dependency of the dielectric function of silver due to the plasma of the quasi free conduction band electrons. There are two equivalent ways to look at plasmonic focusing: by noting the change

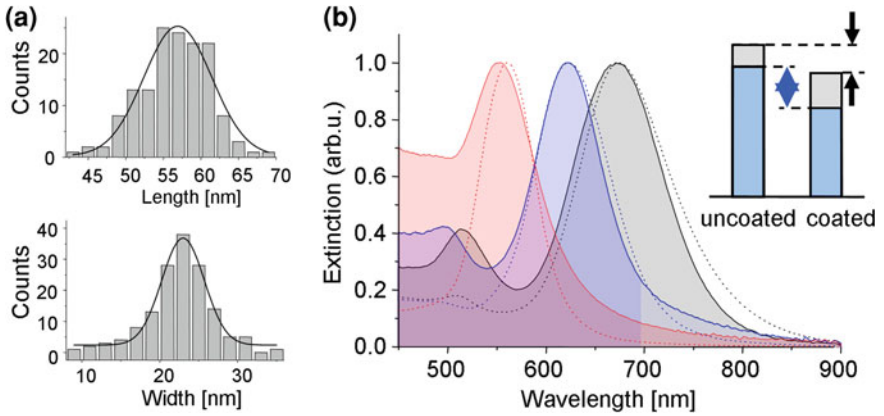

Fig. 10.5 **a** Length and width distribution of a sample of uncoated gold nanorods as determined from TEM images of 145 particles. The length and width show a mean of 56.4 ± 4.4 and 22.8 ± 3.4 nm, respectively. **b** Ensemble extinction spectra of this gold nanoparticle sample (*black*) with a thin (2.3 nm) silver coating (*blue*) and a thick coating (6.9 nm, *red*): *solid lines* measured, *dashed lines* calculated. Only one free parameter enters all three calculations: the eccentricity e used to calculate the geometrical "L factor" Prescott and Mulvaney (2006), here e = 0.95. All other parameters are determined by TEM. The calculated spectra show good agreement to the measurement in both resonance position and linewidth. The inset illustrates the (calculated) linewidth for the uncoated and thinly coated nanorods, in *black/gray* including the single particle contribution and in *blue* without this contribution (i.e., pure plasmonic focusing) [Image reprinted with permission of the American Chemical Society Becker et al. (2008)]

in the slope in the plasmon-shape relation or by considering the plasmon shifts after coating. The latter lets us verify the theoretical model by spectrally investigating the same particles before and after coating without knowing the precise aspect ratio. We expect to find that particles with longer resonance wavelengths (i.e., larger aspect ratio) show a larger plasmon shift than those with a shorter starting wavelength, which we indeed observed (Fig. 10.4b).

10.5 Deduction of the Single Particle Linewidth

The plasmon-shape relation in Fig. 10.4a is derived from an electrodynamic model based on the quasi-static approximation Sect. 2.2, since this model allows to calculate the spectra of coated particles. We test whether this model is able to predict the measured ensemble spectra from a known particle shape distribution, which we obtain by measuring the width and length of about 150 particles per sample on TEM Sect. 4.3 images (Fig. 10.5a). To calculate the spectra only one parameter can be varied, which is the endcap structure of the assumed rods Sect. 2.2.4. The simulation using our electrodynamic model reproduces the observed spectrum well, both for the uncoated and for the coated particles (Fig. 10.5b). The shell thicknesses used here are

inferred from TEM analysis, therefore there are no additional free parameters entering the calculation. Hence, we are confident that this simple method predicts ensemble plasmon wavelength and linewidth accurately. The model lets us theoretically analyze how strong the plasmonic focusing effect would be if the single particle linewidth remained constant after coating. Since the single particle linewidth increases due to the coating, it effectively reduces the amount of linewidth narrowing observable in the ensemble spectra. The convolution of single particle linewidth with the distribution of resonances in the ensemble further weakens the effect of any reduction of either of the two parameters. We show the values for the ensemble linewidth with and without the single particle contribution in the inset of Fig. 10.5b. The plasmonic focusing alone would reduce the linewidth from 97 to 66 nm while the single particle linewidth increases from 28 to 29 nm. Their convolution then changes from 113 to 92 nm, which compares well to the measured change from 112 to 88 nm.

10.6 Conclusion

Our analysis of the *ensemble* plasmon linewidth of silver-coated gold nanorods shows a surprising and important result: the linewidth narrowing by plasmonic focusing. Even though silver-coated nanoparticles have been prepared and studied before, this linewidth narrowing has not been reported - probably because it is only present for very homogeneous silver shells. In combination with extensive particle size analysis by TEM, our electrodynamic model based on quasi-static approximation allows entangling the contributions of single particle linewidth and plasmonic focusing for the observed ensemble linewidth reduction. Plasmonic focusing alone would reduce the ensemble linewidth by about 30 %; the convolution with single particle linewidth reduces the effect to about 20 %. Plasmonic focusing is a new feature of bimetallic core-shell structures, interesting from a fundamental point of view. A sample preparation strategy with plasmonic focusing provides a simple method to obtain high-quality plasmonic particles with tunable resonance energy over the entire visible spectrum.

References

Becker, J., Zins, I., Jakab, A., Khalavka, Y., Schubert, O., & Sönnichsen, C. (2008). Plasmonic focusing reduces ensemble linewidth of silver-coated gold nanorods. *Nano Letters, 8*(6), 1719–1723.

Brigger, I., Dubernet, C., & Couvreur, P. (2002). Nanoparticles in cancer therapy and diagnosis. *Advanced Drug Delivery Reviews, 54*(5), 631–651.

Bryant, G., Garcia de Abajo, F., & Aizpurua, J. (2008). Mapping the plasmon resonances of metallic nanoantennas. *Nano Letters, 8*(2), 631–636.

Campion, A., & Kambhampati, P. (1998). Surface-enhanced raman scattering. *Chemical Society Reviews, 27*(4), 241–250.

Elghanian, R., Storhoff, J. J., Mucic, R. C., Letsinger, R. L., & Mirkin, C. A. (1997). Selective colorimetric detection of polynucleotides based on the distance-dependent optical properties of gold nanoparticles. *Science, 277*(5329), 1078–1081.

Hirsch, L. R., Stafford, R. J., Bankson, J. A., Sershen, S. R., Rivera, B., Price, R. E., et al. (2003). Nanoshell-mediated near-infrared thermal therapy of tumors under magnetic resonance guidance. *Proceedings of the National Academy of Sciences of the United States of America, 100*(23), 13549–13554.

Kneipp, K., Wang, Y., Kneipp, H., Perelman, L. T., Itzkan, I., Dasari, R., et al. (1997). Single molecule detection using surface-enhanced raman scattering (sers). *Physical Review Letters, 78*(9), 1667–1670.

Link, S., El-Sayed, M. A., & Mohamed, M. B. (2005). Simulation of the optical absorption spectra of gold nanorods as a function of their aspect ratio and the effect of the medium dielectric constant (vol 103b, pg 3073, 1999). *Journal of Physical Chemistry B, 109*(20), 10531–10532.

Maier, S., Brongersman, M., Kik, P., Meltzer, S., Requicha, A., & Atwater, H. (2001). Plasmonics-a route to nanoscale optical devices. *Advanced Materials, 13*(19), 1501–1505.

McFarland, A. D., & Van Duyne, R. P. (2003). Single silver nanoparticles as real-time optical sensors with zeptomole sensitivity. *Nano Letters, 3*(8), 1057–1062.

Nie, S., & Emory, S. R. (1997). Probing single molecules and single nanoparticles by surface-enhanced raman scattering. *Science, 275*, 1102–1106.

Peng, X., Wickham, J., & Alivisatos, A. (1998). Kinetics of ii-vi and iii-v colloidal semiconductor nanocrystal growth: "focusing" of size distributions. *Journal of the American Chemical Society, 120*, 5343–5344.

Perez-Juste, J., Pastoriza-Santos, I., Liz-Marzan, L. M., & Mulvaney, P. (2005). Gold nanorods: Synthesis, characterization and applications. *Coordination Chemistry Reviews, 249*(17–18), 1870–1901.

Prescott, S. W., & Mulvaney, P. (2006). Gold nanorod extinction spectra. *Journal of Applied Physics, 99*(12), 123504.

Quinten, M., Leitner, A., Krenn, J. R., & Aussenegg, F. R. (1998). Electromagnetic energy transport via linear chains of silver nanoparticles. *Optics Letters, 23*(17), 1331–1333.

Raschke, G., Kowarik, S., Franzl, T., Sönnichsen, C., Klar, T. A., Feldmann, J., et al. (2003). Biomolecular recognition based on single gold nanoparticle light scattering. *Nano Letters, 3*(7), 935–938.

Reiss, H. (1951). The growth of uniform colloidal dispersions. *Journal of Chemical Physics, 19*(4), 482–487.

Schultz, S., Smith, D. R., Mock, J. J., & Schultz, D. A. (2000). Single-target molecule detection with nonbleaching multicolor optical immunolabels. *Proceedings of the National Academy of Sciences of the United States of America, 97*(3), 996–1001.

Yin, Y., & Alivisatos, A. P. (2005). Colloidal nanocrystal synthesis and the organic-inorganic interface. *Nature, 437*(7059), 664–670.

Chapter 11
Self Calibrating Nano-Ruler

The aim of a nanoruler is to measure distances on a length scale in the order of nanometers. This concept can be realized by two plasmonic nanoparticles (usually spheres), which are placed within a short distance to each other. Since the plasmon modes of both particles are coupled, they influence each other along the interparticle axis (i.e. longitudinal plasmon mode, see inset of Fig. 11.1) resulting in a shift of the resonance wavelength compared to the single particle (Sect. 2.5.7). Because the resulting resonance wavelength depends on the interparticle distance, the spectral investigation of such a dimer allows the determination of the interparticle distance.

However, the resonance wavelength of a dimer is also dependent on the refractive index of the local environment, which can be influenced by several parameters, e.g. the embedding solution, the substrate the particles are immobilized on, or the molecules connecting the two particles. For this reason, a resonance shift of a dimer can have two different origins (interparticle distance or local refractive index change), which are not differentiable if only the longitudinal plasmon mode is measured. This problem could be avoided, if any change in the local refractive index would be measured separately. I will show in Sect. 11.2 that the transversal plasmon mode (perpendicular to the interparticle axis; see inset of Fig. 11.1) indeed depends on the local refractive index, and furthermore fulfills the requirement to be independent on the interparticle distance. Therefore by measuring both plasmon modes of a dimer separately (longitudinal and transversal), the interparticle distance can be estimated, even if the local refractive index changes. Technically, the separation of both plasmon modes can easily be achieved by a polarizer in the light path, since the polarization states of both modes are perpendicular to each other.

In Sect. 11.3 I will present first experimental results on spectral investigations of a single dimer. By a selective replacement of the environmental solution the local refractive index as well as the interparticle distance can be varied, which results in resonance shifts of both plasmon modes. To prove that the interparticle distance change occurs from a conformation change of the molecule connecting both particles caused by the solvent exchange, dynamic light scattering measurements on nanospheres in both solvents are performed. Thereby the particle sizes including the

J. Becker, *Plasmons as Sensors*, Springer Theses,
DOI: 10.1007/978-3-642-31241-0_11, © Springer-Verlag Berlin Heidelberg 2012

surrounding polymer (Sect. 11.4) is obtained. The project was performed with the support of Olaf Schubert, Andreas Trügler, Ulrich Hohenester (simulations) and Inga Zins with the production of dimers.

11.1 Introduction

Using the dependency of the longitudinal plasmon resonance wavelength of a dimer consisting of two spherical gold nanoparticles to monitor its interparticle distance is a well known approach (Sönnichsen et al. 2005; Reinhard et al. 2005). To experimentally investigate the influence of the interparticle distance on the plasmon resonance wavelength usually several dimers are produced by double stranded DNA as connecting molecule (Reinhard et al. 2005) or by lithographically fabricated gold nanoparticles (Jain et al. 2007). In both methods, the separation of the coupled particles could be chosen during their formation, but stays constant afterwards. Only in the case the particles are connected by single DNA strands, the interparticle distance could be varied by the salt concentration in the environmental solution (Sönnichsen et al. 2005), but the local refractive index had carefully to be kept constant since it also influences the resonance position. The extension of this approach allows the variation of the local refractive index, while the interparticle distance could still be monitored. This could be achieved, since the dimers are anisotropical structures and they therefore exhibit two plasmon modes: while one is along the interparticle axis (i.e. longitudinal plasmon mode) the second one corresponds to the "short-axis" of the dimer, which results in a transversal plasmon mode, with a polarization state perpendicular to initial one. As shown in Fig. 11.1, the longitudinal mode scatters light more efficiently and is overlayed with the transversal mode, but the separation of both modes can be obtained by using a polarization filter in the light path.

11.2 Theory on Refractive Index Changes

Figure 11.2a shows the transversal resonance mode for a dimer consisting of two gold spheres with 60 nm in diameter in aqueous solution (refractive index $n = 1.33$, blue line), calculated with the boundary element method (BEM, Chap. 2.4.2). It can be seen, that the resonance is nearly constant for any interparticle distance (only a slight blueshift can be observed for very small interparticle distances (Rechberger et al. 2003). The black line represents the same dimer in a solution with a higher refractive index ($n = 1.5$), showing the same trend of the resonance wavelength. Calculating the difference of these two resonances reveals the shift due to changes in the refractive index of the environment. It is obvious that this shift (i.e. the sensitivity on refractive index changes S_λ [nm/RIU]) is nearly constant for any interparticle distance (inset of Fig. 11.2a).

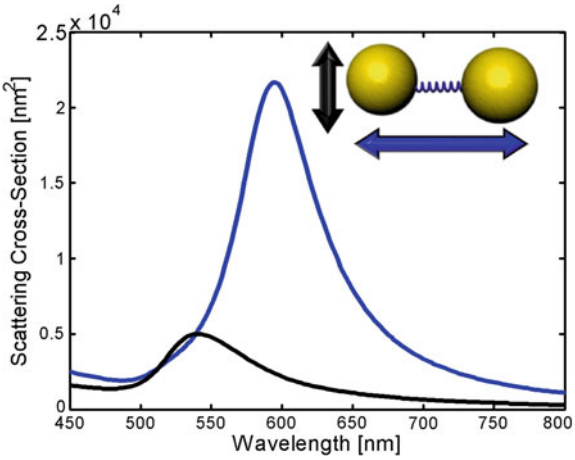

Fig. 11.1 A dimer of nanospheres (particle diameter = 60 nm, interparticle distance = 5 nm) has two scattering modes, which are perpendicular to each other. Since the longitudinal (*blue*) mode is overlayed with the transversal mode (*black*) a polarizer is needed to investigate both modes independently

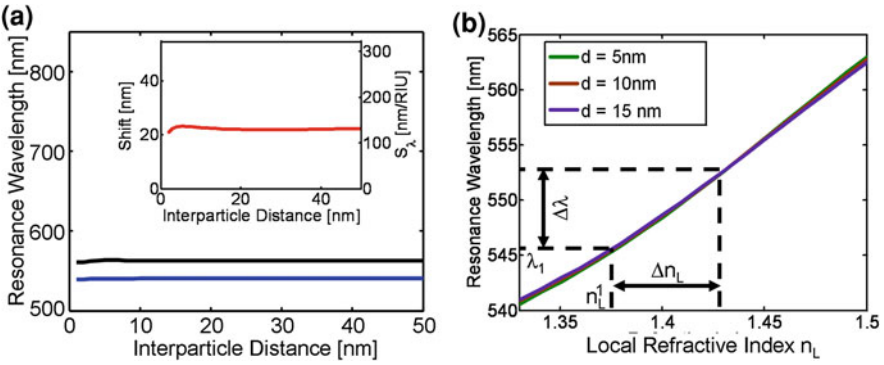

Fig. 11.2 **a** For the transversal plasmon mode the resonance wavelength is nearly independent of the interparticle distance in water (*blue line*) as well as in a medium with refractive index $n = 1.5$ (*black line*). An increase of the refractive index leads to a redshift, which is therefore also constant in respect to the interparticle distance (inset). **b** Relationship of the plasmon resonance and the refractive index for different interparticle distances. The overlapping of the lines emphasizes the independency of the resonance wavelength from the interparticle distance. By measuring the transversal resonance wavelength λ_1 the local effective refractive index n_L^1 can be calculated. An occuring shift $\Delta\lambda$ corresponds therefore in a change of Δn_L

For this reason the local refractive index of the solution can then be calculated if the resonance wavelength of the transversal mode is measured (Fig. 11.2b). Although it is possible to measure the refractive index of a solution by a refractometer, the local refractive index n_L next to the particles might differ. Since the dimers are immobilized

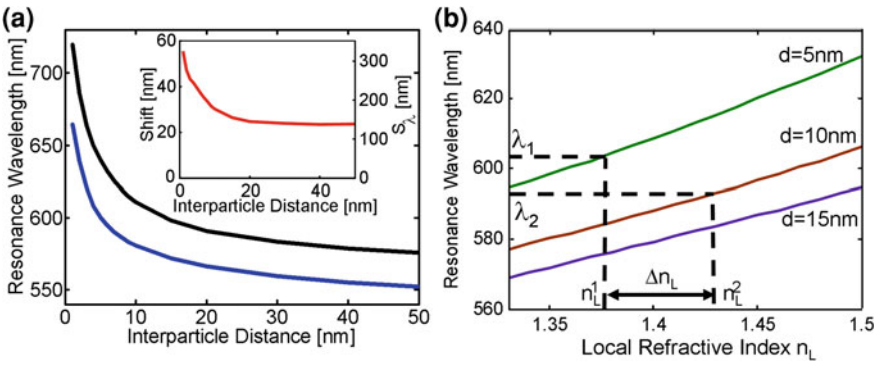

Fig. 11.3 **a** The resonance wavelength of the longitudinal plasmon mode shows a dependency on the interparticle distance in water (*blue line*) as well as in a medium with refractive index $n = 1.5$ (*black line*). An increase of the refractive index leads to a redshift, but in this plasmon mode the shift (i.e. also the sensitivity S_λ) is not independent of the interparticle distance (inset). **b** If the local effective refractive index n_L^1 was estimated from the transversal mode (Fig. 11.2), the measured resonance wavelength λ_1 reveals the interparticle distance. In the case the interparticle distance stays constant for an increase of n_L (5 (*green*), 10 (*brown*) and 15 nm (*purple*) lines), the corresponding resonance wavelength is redshifted. However, if the local refractive index is increased up to n_L^2 and the interparticle distance enlarges (e.g. from 5 to 10 nm), the appropriate resonance wavelength λ_2 can even be blueshifted

on a glass-substrate with a refractive index of $n = 1.5$ this has an influence on the plasmon mode (Sect. 2.5.5). Furthermore the molecules connecting the two particles could also have a different refractive index which may influence the plasmon mode too. Therefore, only in the very special case of using matching refractive indices of the substrate, interconnecting molecules and environmental solution the estimation of the local refractive index would be easy. In any other case the combination of the refractive indices results in a local effective refractive index n_L. Modifying the refractive index of the solution results in a change of n_L and therefore leads to a shift of the resonance wavelength. For this reason, measuring the shift of the transversal mode $\Delta\lambda$ leads to an estimation of Δn_L, which is sketched in Fig. 11.2b. This figure additionally emphasizes the fact, that this resonance wavelength shift is independent of the interparticle distance, since the lines for different interparticle distances superimpose each other.

A different situation is present, if the longitudinal plasmon mode is investigated. Here the resonance wavelength indeed depends on the interparticle distance (Fig. 11.3a). Increasing the refractive index of the solvent results in this case also in a redshift, however the shift is *not* independent of the interparticle distance (inset Fig. 11.3a). For this reason the measurement of the shift in the resonance wavelength of the longitudinal mode reveals a possible change in the interparticle distance. For example an increase of n_L can lead to a blueshift, i.e. a reduced resonance wavelength λ_2, if the interparticle distance is increasing as a consequence of an exchange of the environmental solution (Fig. 11.3b). Another possibility would be a redshift ($\Delta\lambda_e$),

Table 11.1 BEM Simulation of the shift of the resonance wavelength of the longitudinal plasmon mode due to changes of the refractive index and the interparticle distance

Δn	Δd (nm)	$\Delta\lambda$ (nm)
0	+2	$\Delta\lambda_a = -9$
0	−2	$\Delta\lambda_b = 21$
0.03	0	$\Delta\lambda_c = 6$
0.03	+2	$\Delta\lambda_d = -4$
0.03	−2	$\Delta\lambda_e = 28$

The initial dimer consists of two gold spheres with diameters of 60 nm with an interparticle distance of 5 nm and is hosted in water with a refractive index of $n = 1.33$ and has a resonance wavelength of $\lambda = 594$ nm

which is even larger as the expected one for a refractive index increase ($\Delta\lambda_c$), if the interparticle distance decreases (see Table 11.1).

The resonance wavelength shift caused by a refractive index change from $n = 1.33$ to $n = 1.5$ can be transformed into an appropriate sensitivity according to the equation $S_\lambda = \Delta\lambda/\Delta n$. Since the shift for the transversal mode is nearly independent of the interparticle distance, also the appropriate sensitivity has a constant value S_λ^T (Fig. 11.2a, inset). For the longitudinal axis the shift depends on the interparticle distance and therefore this is also valid for the sensitivity S_λ^L (Fig. 11.3a, inset), which can be described in respect to the interparticle distance d by following fit-equation:

$$S_\lambda^L\ [\text{nm/RIU}] = 211.4\ [\text{nm/RIU}] \cdot \exp\left(\frac{d\ [\text{nm}]}{-5.15\ [\text{nm}]}\right) + 138.8\ [\text{nm/RIU}] \quad (11.1)$$

$$S_\lambda^T\ [\text{nm/RIU}] = 132\ [\text{nm/RIU}] \quad (11.2)$$

11.3 Single Particle Measurements

In single particle measurements the transversal and the longitudinal mode are usually overlaying each other, and therefore these two modes have to be measured separately. This separation can be done by a polarization filter, due to the perpendicular polarization state of these two plasmon modes. An ideal approach would be the RotPOL setup, described in Sect. 5.2. In this setup the polarization states are separated by a wedge-shaped rotating polarizer and the resonances of the transversal and the longitudinal mode can be measured by moving a variable interference filter stepwise. Therefore only a certain wavelength is transmitted through the filter and the corresponding intensity of the scattered light is captured by a CCD camera. However, acquiring the spectrum takes about 30–40 min and therefore defocusing of the sample becomes an issue. And already a small defocusing of the sample results in a large variation of the light collected by the objective. As defocusing occurs with progressing time, the amount of the collected light is not constant during one measurement period. However, the collected light at each wavelength step results in the

spectrum and therefore this setup cannot be used to resolve small changes in the resonance wavelength of single particles. For this reason a standard darkfield microscope (Sect. 4.2) is used combined with a polarizer which is rotated manually. The polarization filter is adjusted in the way, that either the transversal (green resonance) or the longitudinal mode (orange to red resonance) of a single dimer clearly appear.

Sample Preparation

In order to prepare dimers on a glass substrate gold spheres with 60 nm diameter (British Biocell International) are rinsed through a flowcell consisting of a thin, flat glass capillary (0.1 mm × 2 mm × 100 mm) connected to PET tubing. Some of the spheres stick to the glass surface, which is enhanced by addition of a 1 M sodium chloride solution. When enough spheres are immobilized water is rinsed to remove the excess of spheres. Afterwards a solution of 2 mM di-thiol-Polyethylenglycol (SH-PEG, $M_w = 6000$ g/mol, Iris Biotech) is flushed into the capillary and incubated for 5 min. Since the thiol-endgroup of the PEG has a strong affinity to bind onto gold, it can be assumed that the molecule is covalently attached on the surface of the spheres. Some of the particles appear already red, probably due to forming dimers already in solution or being not perfectly spherical but rather elongated. For this reason a first picture of the sample is taken at this point of the experiment. To remove the unbound SH-PEG molecules, the flowcell is rinsed again with water and subsequently 60 nm gold spheres are flushed again and incubated for 5 min. Since these PEG-molecules have thiol groups on both ends, the goldspheres in solution can attach to the free thiol groups and therefore form a dimer. The excess of spheres is again removed by rinsing the flowcell with water. Once more a picture of the sample is taken and is compared to the first one. Particles appearing initially green and on the second picture red can be regarded as dimers.

Measurement of the Spectra

After identifying dimers in the sample, the transversal and the longitudinal plasmon resonance of each of them is measured separately. To investigate several particles in the same sample, the stage is moved but the position of each investigated particle is saved. This allows to replace the water ($n = 1.33$) in the flowcell by dimethyl sulfoxide (DMSO, Sigma-Aldrich) having a refractive index of $n = 1.47$ and a subsequent investigation of the same dimers. Increasing the refractive index leads to the expected redshift of the resonance wavelength of the transversal plasmon mode (Fig. 11.4). But the investigation of the longitudinal plasmon mode reveals a blueshift, although the refractive index is increased. This result can only be explained by an increase of the interparticle distance in DMSO. To prove the reversibility, the flowcell is rinsed again with water resulting in an opposite shift: a blueshift for the transversal and a redshift for the longitudinal mode (Fig. 11.4). The procedure is repeated two more times, revealing the repeatability of the system. However, the resonance wavelength of the longitudinal mode shows a gradual overall redshift. Such a gradual redshift was already observed in an experiment using dimers tethered with DNA (Sönnichsen et al. 2005). In this case it was assumed that weakly bound ssDNA leached from the surface of the particles after each washing step, leading to

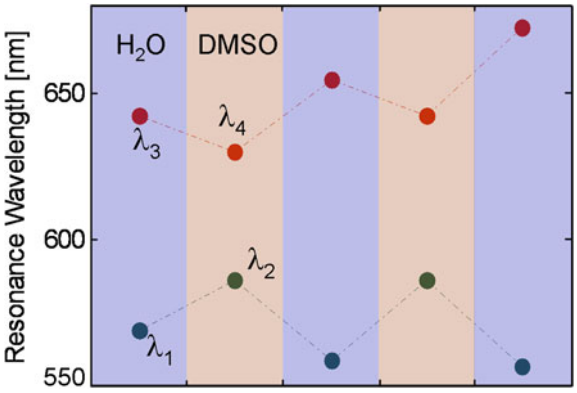

Fig. 11.4 Investigation of the resonances of a single dimer in different refractive indices. Initially the dimer is immobilized on glass substrate and immersed in water $n = 1.33$. Rinsing the flowcell with dimethyl sulfoxide (DMSO) with a refractive index of $n = 1.47$ leads to the expected redshift of the transversal plasmon mode (*blue dots* and *line*, with $\lambda_1 = 568$ nm and $\lambda_2 = 586$ nm). The resonance of the longitudinal plasmon mode (*red dots* and *line*, with $\lambda_3 = 642$ nm and $\lambda_4 = 630$ nm) shows a blueshift, which can only be explained by an increase of the interparticle distance. The reversibility was proved by rinsing the flowcell again with water, which results in an opposite shifts of the two modes compared to the initial ones

a reduced repulsive steric interaction. The leaching of the PEG molecules from the particle's surface and the accompanied reduced repulsive interaction could probably also be a reason for the observed gradual redshift, assuming that dimethyl-sulfone (which is present in small parts in the DMSO solvent, since it is its oxidized state) binds to the gold surface (Nifontova and Lavrentev 1992) and replaces some of the PEG molecules. The origin of the replacement can be explained by the influence of the solvent on the composition, structure and the equilibrium composition of a PEG monolayer bound via thiol-groups onto the gold surface (Bain et al. 1989). However, the given argument is only an assumption and the observed shift, which is an interesting topic itself needs further investigations.

Determination of Interparticle Distances

It is a little bit astonishing that the measured resonance wavelength of the transversal axis in water ($n = 1.33$) is $\lambda_1 = 568$ nm (Fig. 11.4), which is even higher compared to the resonance wavelength estimated by BEM-simulation of a spherical particle totally immersed in $n = 1.5$ ($\lambda_{res} \approx 563$ nm, Fig. 11.2a). To explain the enlarged resonance wavelength a dimer is assumed consisting of two particles which are elongated in respect to the transversal axis (Fig. 11.5).

This geometry shifts the resonance wavelength of the transversal mode of the dimer to higher wavelengths. The assumption of elongated spheres can be justified by transmission electron microscopy (TEM, Chap. 4.3) imaging and subsequently analysis of the shapes, which revealed particle aspect ratios between 1 and 1.4 (Fig. 5.11b).

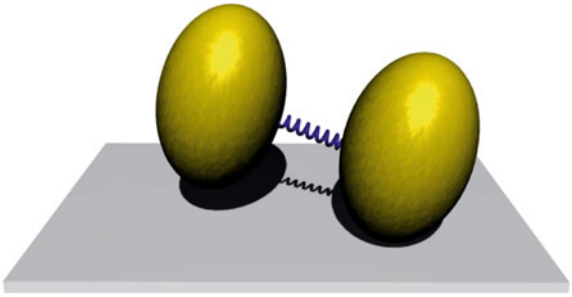

Fig. 11.5 Since the measured wavelength of the transversal axis of the dimer in water ($\lambda_1 = 568$ nm) is smaller compared to the resonance in $n = 1.5$ ($\lambda_{res} \approx 563$ nm) a dimer is assumed, consisting of two spheroidal particles which are elongated in respect to the transversal axis

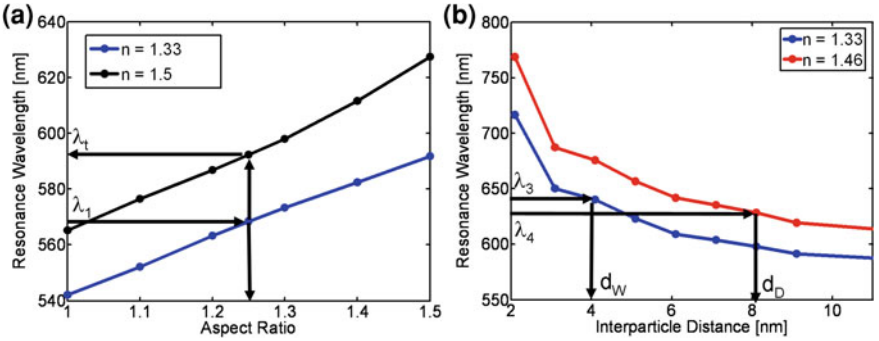

Fig. 11.6 **a** DDA simulation of the resonance wavelength of the transversal mode of dimers consisting of spheroidal particles with varying aspect ratio in water (*blue*) and $n = 1.5$ (*black*). Comparison with the measured transversal resonance λ_1 of the dimer in water reveals an aspect ratio of AR ≈ 1.25. The plasmonic sensitivity S_λ of the transversal mode is calculated using additionally the resonance wavelength λ_t in $n = 1.5$. In combination with the measured resonance wavelength λ_2 of the transversal mode in the second solvent (DMSO) the local refractive index n_L could be estimated to $n_L = 1.46$. **b** DDA simulations of the longitudinal mode of a dimer consisting of two spheroidal particles with aspect ratio AR $= 1.25$ in water and in $n_L = 1.46$. The measured resonances λ_3 and λ_4 reveal a interparticle distance of $d_W \approx 4$ nm in water and $d_D \approx 8$ nm in DMSO, respectively. This means an increase in the interparticle distance of $\Delta d \approx 4$ nm, due to the exchange of the solvent from water to DMSO

For an estimation of the existing aspect ratio of the single particles in the dimer, we simulate dimers with varying aspect ratios using the discrete dipole approximation (DDA, Chap. 2.4.1) and extracted the resonance wavelengths of the transversal modes (Fig. 11.6a). A comparison of these values with the measured transversal resonance wavelength in water $\lambda_1 = 568$ nm reveals an aspect ratio of AR ≈ 1.25. To obtain the plasmonic sensitivity S_λ on changes in the refractive index we additionally simulate such a dimer in an environment having a refractive index of $n = 1.5$, which results

in a transversal resonance wavelength $\lambda_t = 589$ nm. Therefore S_λ amounts to: $S_\lambda^t = (592\,\text{nm} - 568\,\text{nm})/(1.5 - 1.33) = 141$ nm/RIU.

In a next step we calculate the local refractive index n_L in the second solvent (DMSO) from the measured resonance of the transversal mode λ_2, which was determined as $\lambda_2 = 586$ nm. Compared to λ_1 in water this results in a shift of $\Delta\lambda = 18$ nm and therefore the increase in the refractive index is: $\Delta n = \Delta\lambda / S_\lambda^t = 0.128$ RIU. Hence, the local refractive index in the second solvent is: $n_L = 1.33 + \Delta n = 1.46$. This value is in a good agreement with the value $n_R = 1.47$ determined by a refractometer (Mettler Toledo, Refracto 30PX).

To estimate the interparticle distances the resonances of the longitudinal axis has to be considered. Initially the dimer is in water and comparing the measured resonance $\lambda_3 = 642$ nm (Fig. 11.4) with the appropriate simulation reveals an interparticle distance of $d_W \approx 4$ nm (Fig. 11.6b). For the calculation of the interparticle distance in the second solvent (DMSO), we simulate the resonance wavelength in $n_L = 1.46$ (as it was determined from the transversal axis) for different interparticle distances. Comparing these simulations with the measured resonance wavelength $\lambda_4 = 630$ nm the interparticle distance d_D can be estimated to $d_D \approx 8$ nm. This corresponds to an increase of $\Delta d \approx 4$ nm due to the exchange of the solvent from water to DMSO.

11.4 Size-Measurements by DLS

To prove the size increase of the particles using DMSO as solvent instead of water, the particle sizes measured by dynamic light scattering (DLS, Chap. 4.4) in both media are compared. First of all, the initially citrate-stabilized gold nanospheres in water are measured, which results in a hydrodynamic diameter of 46.5 ± 2.6 nm for the nominally 40 nm particles (British Biocell International). Afterwards the particles are coated with methoxy-Polyethylenglycol-thiol (mPEG, $M_w = 6000$ g/mol, Iris Biotech) by centrifugation of 1 mL of the spheres and redispersion of the pellet in 100 µL of a 2 mM PEG solution and incubation over night. In this case here, it is not possible to use SH-PEG like in the coating process using immobilized particles on a glass substrate, since the particles are coated directly in solution which would lead to a precipitation. Therefore a PEG molecule of the same molecular weight was used, having only one thiol endgroup, which binds to the gold surface, and methoxy as the other endgroup as a non-reactive entity to prevent aggregation of the particles. To remove after the coating process excess of mPEG the solution was centrifuged twice and redispersed each time in water. DLS measurement on these particles reveal a hydrodynamic diameter of 71.3 ± 0.8 nm, where the size increase compared to the citrate stabilized particles reveal the successful coating of the particles by mPEG molecules. In the next step the water is exchanged by centrifugation of these particles followed by a redispersion in DMSO. The following DLS measurement results in a hydrodynamic diameter of 87.4 ± 1.7 nm (Fig. 11.7). This proves the hypothesis claimed in the section before (Ozdemir and Guner 2007), that the PEG molecule

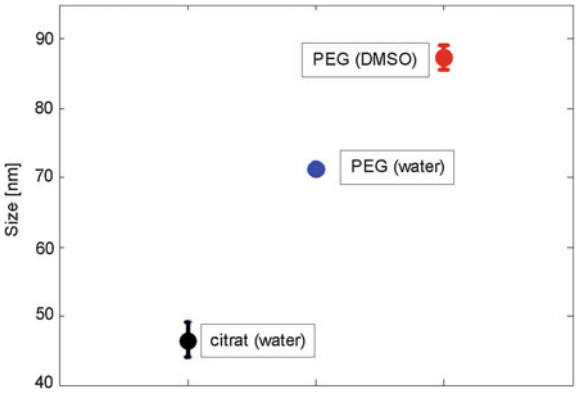

Fig. 11.7 Dynamic light scattering (DLS) measurements of nominally 40 nm spherical particles in water initially stabilized with citrate reveals a hydrodynamic diameter of 46.5 $\pm$ 2.6 nm. After coating the particles with methoxy-Polyethylenglycol-thiol (mPEG) molecules the hydrodynamic diameter (also in water) is increased to 71.3 $\pm$ 0.8 nm. After transfer of these particles into DMSO the hydrodynamic diameter amounts to 87.4 $\pm$ 1.7 nm, which proves the hypothesis that the PEG molecule is more stretched in DMSO then in water

is more stretched in DMSO then in water, which leads to an increased interparticle distance for dimers connected by PEG molecules.

11.5 Conclusion

Investigation of the resonance wavelength of the longitudinal mode of a dimer depends on the interparticle distance as well as on the local refractive index. The resonance wavelength of the transversal plasmon mode also varies with changes in the refractive index, but is nearly independent of any occurring interparticle distance changes. Therefore, the transversal axis can be used to monitor the local refractive index and subsequently calibrate the longitudinal plasmon mode to the appropriate refractive index. This leads to the possibility to use dimers as sophisticated nanorulers, since interparticle distances can be determined for the first time even if changes in the refractive index are occurring.

In a first approach we experimentally investigated a dimer consisting of two gold nanoparticles connected by di-thiol-Polyethylenglycol (SH-PEG). Initially we investigated the dimer in water and obtained an interparticle distance of approximately 4 nm. Thereafter we exchanged the environmental solution to DMSO with a higher refractive index. By determination of the resonance wavelength shift of the transversal axis we were able to measure the increase of the local refractive index. entally investigated a dimer consisting of two gold nanoparticles connected by di-thiol-Polyethylenglycol (SH-PEG). Initially we investigated the dimer in water and obtained an interparticle distance of approximately 4 nm. Thereafter we exchanged

the environmental solution to DMSO with a higher refractive index. By determination of the resonance wavelength shift of the transversal axis we were able to measure the increase of the local refractive index. This value was used to "calibrate" the nanoruler and to estimate an interparticle distance of approximately 8 nm in DMSO, by measuring the resonance wavelength of the longitudinal mode. In a control experiment we were able to proof by dynamic light scattering that the hydrodynamic diameters of PEG coated particles are indeed larger in DMSO then in water.

We were therefore able to present for the first time an optical approach, which allows to monitor interparticle distances on the nanoscale, even if the refractive index of the environment is changed.

References

Bain, C. D., Evall, J., & Whitesides, G. M. (1989). Formation of monolayers by the coadsorption of thiols on gold–variation in the head group, tail group, and solvent. *Journal of the American Chemical Society, 111*(18), 7155–7164.

Jain, P. K., Huang, W. Y., & El-Sayed, M. (2007). On the universal scaling behavior of the distance decay of plasmon coupling in metal nanoparticle pairs: A plasmon ruler equation. *Nano Letters, 7*, 2080–2088.

Nifontova, G. A., Lavrentev, I. P. (1992). Dissolution of metallic gold in dmso rx systems–the concept of a donor-acceptor electron-transfer system. *Bulletin of the Russian Academy of Sciences-Division of Chemical Science, 41*(3), 391–397 (Part 1).

Ozdemir, C., & Guner, A. (2007). Solubility probles of poly(ethylene glycol)/solvent systems, i: Qualitative comparison of solubility parameter approaches. *European Polymer Journal, 43*(7), 3068–3093.

Rechberger, W., Hohenau, A., Leitner, A., Krenn, J. R., Lamprecht, B., & Aussenegg, F. R. (2003). Optical properties of two interacting gold nanoparticles. *Optics Communications, 220*(1–3), 137–141.

Reinhard, B. M., Siu, M., Agarwal, H., Alivisatos, A. P., & Liphardt, J. (2005). Calibration of dynamic molecular rule based on plasmon coupling between gold nanoparticles. *Nano Letters, 5*(11), 2246–2252.

Sönnichsen, C., Reinhard, B. M., Liphardt, J., & Alivisatos, A. P. (2005). A molecular ruler based on plasmon coupling of single gold and silver nanoparticles. *Nature Biotechnology, 23*(6), 741–745.

Chapter 12
Summary

In this thesis I show my work on the improvement of plasmonic bio-sensors. This progress came in three areas: automatization of spectral acquisition, developing a versatile bio-functionalization approach, and increasing the plasmonic sensitivity. The basis of such plasmonic bio-sensors is the very efficient light scattering at the plasmon resonance wavelength, which is sensitive to the local refractive index of the environment. Since the plasmonic light scattering is so strong it is possible to investigate individual plasmonic nanoparticles in a light microscope with sizes an order of magnitude smaller than the optical diffraction limit, i.e. down to about 20 nm in diameter.

In microscope setups used until now, only one single nanoparticle could be investigated manually resulting in time consuming procedures and lack of statistical information. To circumvent these drawbacks I developed a novel fast single particle spectroscopy (fastSPS) method, which allows the investigation of all particles in the field of view automatically (Chap. 5). Furthermore, with this setup up to 30 particles can be monitored continuously in parallel. This improvement was achieved by replacing the entrance pinhole of the coupled spectrometer by a liquid crystal device (LCD), which acts as an electronically addressable shutter.

To automatize the wavelength dependent polarization anisotropy measurements of non-isotropic nanoparticles, I build a second setup (RotPOL). In this RotPOL setup, the fast rotation of a wedge-shaped polarizer is combined with a stepwise movable variable interference filter allowing the investigation of several particles at once. First investigations on differently shaped nanoparticles (e.g. cubes, rods, triangles, and dimers of spheres) provided new insights into their polarization modes.

In order to detect specific bio-molecules, the plasmonic particles need to be functionalized with organic ligands. I developed a flexible approach based on coating gold nanorods with bio-membranes (Chap. 7). By using appropriately functionalized lipid headgroups, I was able to detect the binding of the protein streptavidin onto the membrane by measuring the corresponding plasmon resonance shift caused by the larger refractive index of biomolecules compared to the deplaced aqueous solution. The advantage of using membrane coated nanoparticles is the high number

J. Becker, *Plasmons as Sensors*, Springer Theses,
DOI: 10.1007/978-3-642-31241-0_12, © Springer-Verlag Berlin Heidelberg 2012

of different commercially available headgroups allowing the specific investigation of various biomolecules, which are easily integrated into the membrane. Furthermore, the membrane suppresses unwanted non-specific binding to the particles and the substrate. Using the high statistics collected by the fastSPS setup, different protein-membrane spacings could be distinguished.

To detect small environmental changes with plasmonic sensors, a high sensitivity to changes in the refractive index is desirable. I performed systematic theoretical and experimental investigations (Chap. 8) to identify the particle geometry with the highest sensitivity. In contrary to many claims, I could show that gold nanorods with an aspect ratio in the range of 3–4 have an optimum in sensitivity. In this study, I introduced a new and more general measure for the sensing quality (FOM*). In a second step, gold nanorods were chemically modified in two ways to increase the sensitivity further (Chap. 9): encapsulating them in a porous gold cage ("nanorattles") or coating them with a thin silver shell. I used the fastSPS setup to investigate hundreds of single particles to quantify for both novel particle types the sensitivity increase compared to bare gold nanorods with the same resonance wavelength. Interestingly, I found another effect, the silver coating is evoking: the reduction of the spectral linewidth of a nanoparticle-ensemble (Chap. 10). By extended simulations and theoretical considerations, I could explain this narrowing by the determination of a change in the relation connecting the particles' shape with their plasmon resonance. This change ("plasmonic focusing") is a new feature for bimetallic core-shell structures providing a new tool to synthesize plasmonic nanoparticles with a narrow distribution of plasmon resonance wavelengths.

A different plasmonic sensing scheme uses two coupled nanoparticles to estimate the interparticle separation from the corresponding shift of the plasmon resonance along the connection axis. The plasmon resonance perpendicular to the connection axis is (nearly) independent from the interparticle distance, hence revealing the environmental refractive index. Determining the plasmon resonance in both directions separately allows to investigate both interparticle distance and refractive index at the same time. I showed the practical usefulness of such a refractive index calibrated nanoruler in experiments on polyethyleneglycol (PEG) coupled particle dimers (Chap. 11).

Besides using plasmonic nanoparticles as molecular sensors, the plasmon resonance can be used to monitor size and shape evolution during particle growth. Exposing preformed gold nanorods to a solution containing further gold ions, I was able to continuously follow size and shape changes on a single particle level using both the fastSPS and the RotPOL setups (Chap. 6). This allowed to extract quantitative data on nanoparticle growth at each time and provided novel insights into the nanoparticles synthesis process.

My work provided novel setups for rapid single particle spectroscopy, which enables the possibility to sense molecular events in a systematic way. The range of applications I demonstrated are only a starting point. The developed techniques provide the groundwork for further optimization of spectral acquisition, chemical procedures, and better sensing schemes.

Author Biography

Additional Scientific Publications During PhD (Not Presented in this Thesis):

"*A Nanoassembled Plasmonic-Photonic Hybrid Cavity for Tailored Light-Matter Coupling*"
M. Barth, S. Schietinger, S. Fischer, J. Becker, N. Nüsse, T. Eichele, B. Löchel, C. Sönnichsen, and O. Benson
Nano Letters, Year: 2010, Vol. 10, Pages: 891–895

"*Au@MnONanoflowers: Hybrid Nanocomposites for Selective Dual Functionalization and Imaging*"
T. D. Schladt, M. I. Shukoor, K. Schneider, M. N. Tahir, F. Natalio, I. Ament, J. Becker, F. D. Jochum, S. Weber, O. Köhler, P. Theato, L. M. Schreiber, C. Sönnichsen, H. C.Schröder, W. E. G. Müller, and W. Tremel
Angewandte Chemie International Edition, Year: 2010, Vol. 49, Pages: 3976–3980

Conference Contributions

Talks

"*Gold Nanorods as Novel Nonbleaching Plasmon-Based Sensors for Molecular Orientations and Local Refractive Index Changes*"
Spring Meeting of the German Physical Society, Dresden (Germany), March 2006

"*Protein-Membrane Interaction Probed by Single Plasmonic Nanoparticles*"
Heraeus-Seminar "Ultrafast Nanooptics", Bad Honnef (Germany), Juni 2008

J. Becker, *Plasmons as Sensors*, Springer Theses
DOI: 10.1007/978-3-642-31241-0, © Springer-Verlag Berlin Heidelberg 2012

"*Single Plasmonic Nanoparticles as Biosensors*" (Invited Talk)
Fall meeting of the European Materials Research Society (E-MRS), Warsaw (Poland), September 2008

"*Protein-Membrane Interaction Probed by Single Plasmonic Nanoparticles*"
Annual Meeting of the Optical Society of America (OSA), Rochester, NY (USA), November 2008